Title

Plastron State and Drag Reduction of High-Performance Superhydrophobic (SHPo) Surfaces in High-Speed Turbulent Flows on Open Water

Author

Yu, Ning

Publication Date

2022

Peer reviewed|Thesis/dissertation

UNIVERSITY OF CALIFORNIA

Los Angeles

Plastron State and Drag Reduction of High-Performance Superhydrophobic (SHPo) Surfaces in High-Speed Turbulent Flows on Open Water

A dissertation submitted in partial satisfaction of the

requirements for the degree Doctor of Philosophy

in Mechanical Engineering

by

Ning Yu

2022

ABSTRACT OF THE DISSERTATION

Plastron State and Drag Reduction of High-Performance Superhydrophobic (SHPo) Surfaces in High-Speed Turbulent Flows on Open Water

by

Ning Yu

Doctor of Philosophy in Mechanical Engineering

University of California, Los Angeles, 2022

Professor Chang-Jin Kim, Chair

Superhydrophobic (SHPo) surfaces, which may capture a thin air layer (called plastron) on them underwater, have been studied over the last two decades most notably due to their potential drag-reducing ability for water vessels. Despite many reports of successful drag reduction in laboratory settings, no success has been reported for highly turbulent flows on the open water in natural environment until just two years ago. While reporting around 30% of reduction under a boat, the recent success indicated that the plastron was the culprit for most of the failures and the resulting controversies about SHPo drag reduction. The current study is motivated by our finding that the common practice of confirming the plastron with the silvery sheen appearance is not sufficient and may be seriously misleading for SHPo drag reduction research. Since drag reduction requires a

plastron pinned on top of the surface asperities while depinned plastron may still appear bright, we develop a convenient observation strategy that can discern the pinned from the depinned plastron in field studies such as under a boat. By further revamping the 13 foot motorboat retrofitted for drag-reduction experiments, we study the behavior of plastron on micro-trench SHPo surfaces in highly turbulent flows on a natural sea environment. A unified theory is developed and experimentally confirmed to predict the maximum trench length that allows for a full plastron in the typical flow conditions of watercraft. Furthermore, high-performance SHPo surfaces are developed with micro electro mechanical systems (MEMS) technology to maintain a full plastron at typical boat speeds (tested up to 14 knots). In addition to testing the effect of slip length and obtaining about 30% of drag reduction with longitudinal trench SHPo surfaces, transverse trench and aligned post SHPo surfaces are also tested to reveal the effect of transverse slip on drag reduction in the turbulent flows under the boat.

The dissertation of Ning Yu is approved.

Pei-Yu Chiou

Jeff D. Eldredge

Kunihiko Taira

Richard F. Ambrose

Chang-Jin Kim, Committee Chair

University of California, Los Angeles

2022

Dedicated to my family

TABLE OF CONTENTS

LIST OF FIGURES

LIST OF TABLES

ACKNOWLEDGEMENTS

To start, I would like to express my deepest gratitude to my advisor, Prof. Chang-Jin "CJ" Kim, who has consistently guided me with his wisdom and expertise, encouraged me with his patience and kindness, inspired me with his passion and curiosity, throughout my Ph.D. life. I am blessed with an advisor who teaches and develops critical thinking in me and a mentor who cares for and motivates my personal growth.

I am deeply grateful to Prof. Jeff Eldredge, for his invaluable contribution to my understanding of fluid mechanics and his constructive advice regarding my Ph.D. research. I would like to offer my special thanks to Prof. Pei-Yu "Eric" Chiou, for his valuable guidance on my MEMS study, insightful suggestions for my research, and generous support for my career. I would like to extend my sincere appreciation to Prof. Kunihiko "Sam" Taira and Prof. Richard Ambrose for their kindness to be my committee members and for their suggestions on my work.

I am truly thankful to Mr. Byron Pfeifer and the UCLA Aquatic Center for assisting me with the retrofitting of the boat. I appreciate the help from Dr. Matt Schibler for his assistance on the confocal microscopy in UCLA CNSI. Many thanks to Prof. Jae Hwa Lee and Mr. Sun Youb Lee for the numerical analysis of flows over an air-filled trench. I thank the staff from UCLA Nanolab for their assistance with MEMS fabrication.

I would like to thank my colleagues at UCLA for their cooperation, assistance, and discussions throughout my Ph.D. journey. I very much appreciate the guidance from Dr. Muchen Xu, who generously taught me how to do research at the beginning of my Ph.D. life. I thank Mr. Zhaohui "Ray" Li, Mr. Alexander McClelland, Mr. Francisco Jose del Campo Melchor, and Ms. Sarina

Kiani for their valuable assistance in my projects. I enjoyed working with Dr. Ryan McGuan, Mr. Qinning “Leo” Wang, Mr. Hyunsung “Eric” Cho, Mr. Christopher Carter, Mr. Xiaojie “Toby” Tao, and Mr. Caedmon Gouldthorpe, to name just a few.

Finally, from the bottom of my heart, I would like to say thank you to my parents. Without their unwavering support and unconditional love, I would not have been able to experience such a wonderful and challenging adventure.

VITA

2016	B.S. Mechanical Engineering Tsinghua University, Beijing, China
2018	M.S. Mechanical Engineering University of California, Los Angeles, USA
2016-2022	Graduate Student Researcher Teaching Associate Mechanical and Aerospace Engineering Department University of California, Los Angeles, USA

PUBLICATIONS AND PRESENTATIONS

N. Yu and C.-J. Kim, "Detecting the sub-states of grating superhydrophobic surfaces with naked eyes." *Proceedings of the IEEE International Conference on Micro Electro Mechanical Systems*, January 2018, Belfast, UK, pp. 1293-1295 (Poster).

S. Pan, T. Saso, N. Yu, M. Sokoluk,G. Yao, N. Umehara, and X. Li, "New study on tribological performance of AA7075-TiB2 nanocomposites." *Tribology International*, vol. 152, pp. 106565, 2020.

M. Xu, A. Grabowski, N. Yu, G. Kerezyte, J.-W. Lee, B. R. Pfeifer and C.-J. Kim, "Superhydrophobic drag reduction for turbulent flows in open water." *Physical Review Applied*, vol. 13, pp. 034056, 2020.

M. Xu, B. Arihara, H. Tong, N. Yu, Y. Ujiie and C.-J. Kim, "A low-profile wall shear comparator to mount and test surface samples." *Experiments in Fluids*, vol. 61, pp. 1-13, 2020.

M. Xu, N. Yu, and C.-J. Kim, "Superhydrophobic drag reduction in high-speed towing tank." *Journal of Fluid Mechanics*, vol. 908, pp. A6, 2021.

N. Yu, S. Kiani, M. Xu, and C.-J. Kim, "Brightness of microtrench superhydrophobic surfaces and visual detection of intermediate wetting states." *Langmuir*, vol. 37, 1206-1214, 2021.

N. Yu, Z. Li, A. McClelland, and C.-J. Kim, "Combined Theory and Experimental Verification of Plastron Stability on Superhydrophobic Surface." *Proceedings of the IEEE International Conference on Micro Electro Mechanical Systems*, January 2022, Virtual, pp. 99-101 (Oral, Outstanding Student Paper Award Finalist).

Chapter 1 Introduction

1.1 Background

Mother nature never fails to fascinate human beings with its magical phenomena: water droplets rolling off lotus leaf effortlessly [1], water striders moving on the water of a pond quickly [2, 3], fishing spiders diving underwater freely [4]. Millions of years of evolution have granted these species an extraordinary ability to propel water out of their body surfaces. With decades of exploration and study, people found one of the key mechanisms behind all of these interesting appearances was a microscopic roughness made of hydrophobic material on what is called a superhydrophobic (SHPo) surface, where small pockets of air could be captured between the water and such surfaces and prevent the wetting by water. The air layer, which is called plastron [5], provides the water-air interface, also called the meniscus, which makes all the natural "magics" happen.

1.1.1 Definition of SHPo Surface

To study the adhesion of fluids to the solids, Young [6] defined the contact angle, as shown in Figure 1-1(a), of a liquid sitting on a smooth solid surface in the vapor environment.

$$\gamma_{SV} = \gamma_{SL} + \gamma_{LV} \cos\theta_Y \tag{1-1}$$

where γ_{SV}, γ_{SL}, and γ_{LV} are the tension of the solid-vapor interface, solid-liquid interface, and liquid-vapor interface, respectively, and Yong's contact angle θ_Y is also called intrinsic contact angle. The material properties of each phase determine Yong's contact angle θ_Y. In an air environment, if the intrinsic contact angle of the water droplet on a smooth solid surface is smaller

than 90°, the surface is regarded as a hydrophilic surface, and the material of the solid surface is deemed to be hydrophilic. On the other hand, if the intrinsic contact angle of the water droplet on the smooth solid surface is larger than 90°, the surface is then regarded as hydrophobic surface and the solid material is regarded as hydrophobic. If a droplet is placed on a tilted surface and starts sliding off, as shown in Figure 1-1(b), the tilting angle is called roll-off angle α, the larger contact angle at the leading edge is called advancing contact angle θ_a, and the smaller contact angle at the trailing edge is called receding contact angle θ_r. The difference between θ_a and θ_r is called contact angle hysteresis.

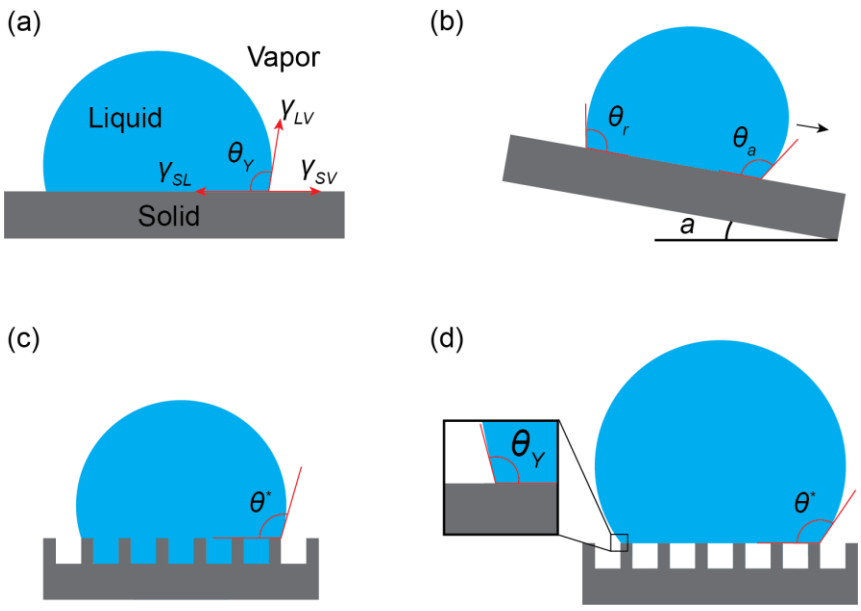

Figure 1-1. Cross-section view of a water droplet on various surfaces. (a) Droplet on a smooth surface with intrinsic contact angle or Young's contact angle θ_Y. (b) Droplet on a tilted smooth surface with advancing contact angle θ_a, receding contact angle θ_r, and roll-off angle α. (c) Droplet on a rough surface at Wenzel state with apparent contact angle θ^*. (d) Droplet on a rough surface at Cassie-Baxter state with apparent contact angle θ^*. The inset figure shows the intrinsic contact angle of water on the asperity top in the zoom-in view.

On a rough surface, Young's equation (1-1) can be applied to determine the apparent contact angle of the droplet, θ^*, as shown in Figure 1-1(c) and (d), with the different wetting status of the liquid on the solid roughness. First, if the roughness is filled by the liquid, which is defined as a Wenzel state [7], the apparent contact angle is determined by

$$\cos\theta^* = r\cos\theta_Y \tag{1-2}$$

where *r* is the roughness defined as the ratio of the actual solid-liquid interface area to the projected solid-liquid interface area. Wenzel's model predicts that the roughness of the surface will promote the wettability of the surface. In other words, the apparent contact angle on a rough hydrophobic surface will be larger than the intrinsic contact angle on the smooth surface with the same hydrophobic material (i.e., becomes more hydrophobic), while the apparent contact angle on a rough hydrophilic surface will be smaller than the intrinsic contact angle on the smooth surface with the same hydrophilic material (i.e., becomes more hydrophilic). Second, if there are air pockets captured inside the roughness, such state is called the Cassie-Baxter state (or Cassie state), where the apparent contact angle is determined by

$$\cos\theta^* = \Phi_S\cos\theta_Y - \left(1-\Phi_S\right) \tag{1-3}$$

where Φ_S is the fraction of solid-liquid interface to the entire contact area between the liquid and the surface. The Cassie-Baxter model predicts that the air pockets will increase the apparent angle of the surface regardless of the intrinsic contact angle. To determine at which state the surface will be more thermodynamically stable, the wetting diagram of a rough hydrophobic surface is shown in Figure 1-2. When the $\cos\theta^*$ value of the Wenzel state is larger than that of the Cassie state, the surface will have less Gibb's free energy and tend to stay at the Wenzel state, and vice versa when

the cos θ^* value of the Cassie state is larger than that of the Wenzel state. The critical intrinsic contact angle is $\cos\theta_c = \frac{\Phi_s - 1}{r - \Phi_s}$ [8, 9], as shown in Figure 1-2.

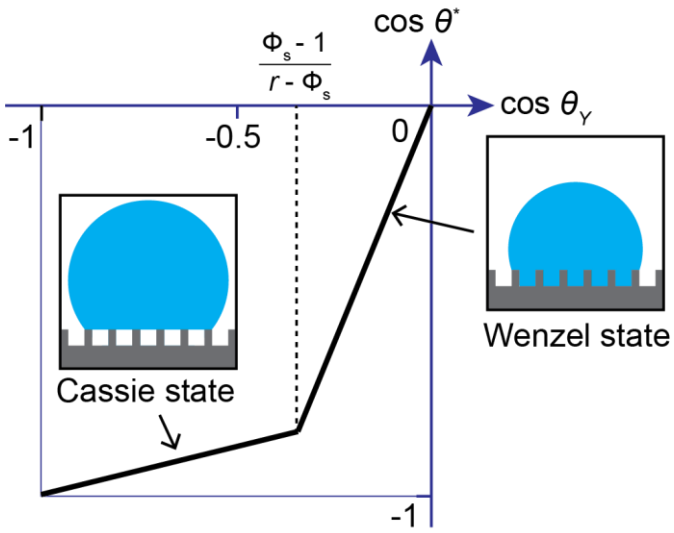

Figure 1-2. Schematic of wetting diagram of the rough hydrophobic surface [8]. The dotted line shows the critical intrinsic contact angle, where the Wenzel and Cassie states are at the same energy state.

The SHPo surface is usually regarded as the surface on which a water droplet has an apparent contact angle larger than 150° and can easily roll off (i.e., small contact angle hysteresis) [10, 11], which requires the surface to remain in Cassie state. While the largest intrinsic contact angle on a smooth surface has never been found to be larger than ~120°, it has been well-known that creating the SHPo surface with high water-repelling ability requires utilization of the chemical properties of hydrophobic material (i.e., large intrinsic contact angle) as well as the physical properties of being rough (i.e., solid-liquid fraction smaller than unity).

1.1.2 Applications of SHPo Surfaces: from Nature to Functional

Using scanning electron microscopy (SEM) established in 1965 [12], the secret of the water-repelling ability of multiple plants, especially the lotus leaf, was revealed to us with the detailed SEM pictures of the hierarchical micro-nano structures on its macroscopically smooth surfaces [1, 13, 14], as shown in Figure 1-3(a). The extraordinary water-resistance ability of these plants makes water bead off the surface completely, which therefore sustain its self-cleanliness by washing off the contamination. While discovered on many other plant species, such effect has been termed as "Lotus effect". The dryness and cleanness of the plant's leaf empower their ability to ensure the photosynthesis process and protect themselves from pathogen attack. By mimicking the similar hierarchical structures on the surface, people have fabricated SHPo surfaces with similar self-cleaning abilities [15, 16].

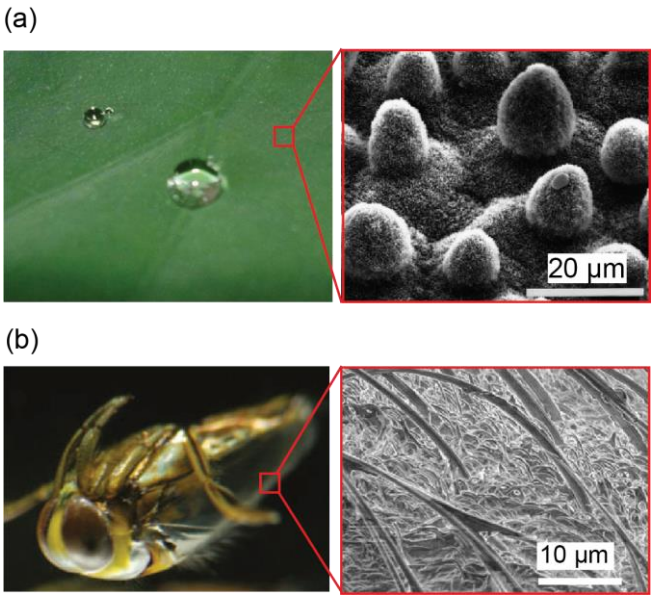

Figure 1-3. Superhydrophobic surface in nature. (a) Water droplet on lotus leaf [13]. The inset picture SEM shows the hierarchical micro-nano structures on the leaf [1]. (b) Picture of backswimmer [17]. The inset SEM picture shows the microscale hair on its back [4].

While most of the SHPo surfaces in nature are found in the air for repelling water droplets, some creatures utilize the SHPo surface underwater to capture a pocket of air for their living. For example, the backswimmer (*Notonecta*) grabs air bubbles on its back collected from the water surface with the assistance of the microscale hairs for breathing underwater, as shown in Figure 1-3(b) [4, 17]. The underwater spiders (*Argyroneta Aquatica*) construct air bells under water for breathing and living by capturing air bubbles around their body using hairs on their abdomen and legs [18, 19].

1.2 Drag Reduction of SHPo Surface

While most of the underwater applications of SHPo surfaces in nature are for restoring the plastron for breathing, people find a potential utilization of the plastron for reducing the underwater skin friction on the surface. Although there are few related examples in nature [20], this subject has been attracting tremendous attention over the past 20 years due to its significance in water transportation.

Among the total resistance of a traveling ship, 50-85% of the resistance is from skin friction [21]. Marine transport is accounted for more than 90% of the global transport of international trade goods. The global annual fuel consumption of marine shipping is estimated to be ~330 million metric tons [22]. Marine shipping generates 2.5-3.5% of global CO_2 emissions [23] and also 13% of SOx and 15% of NOx emissions [24]. Reducing only a fraction of that by reducing the drag of marine vessels can be of great significance for protecting the environment and preserving energy.

1.2.1 Slip on SHPo Surface

When a liquid flows over a solid surface, the viscosity of the liquid will cause shear stress on the

surface. For a Newtonian fluid, the shear stress is proportional to the velocity gradient on the surface and expressed as

$$\vec{\tau} = \mu \nabla \vec{u} \tag{1-4}$$

where μ is the dynamic viscosity of the fluid. On a smooth surface, there exist a boundary layer in the flow on the surface, such as that the fluid velocity is the same as the free stream velocity at the outer edge of the boundary. At the other end of the boundary, i.e., on the solid surface, the fluid velocity is zero, which is called no-slip boundary condition, as illustrated in Figure 1-4(a). The velocity gradient on the surface creates the shear stress on the surface, which is regarded as skin friction. However, if there exists a thin layer of gas between the liquid and solid surface, the gas provides a lubricating effect, thus creating an effective slip on the solid surface, i.e., slip boundary condition. The amount of slip is quantified by a parameter called slip length, λ, which is the virtual distance into the wall where the extrapolated flow velocity vanishes to zero, as shown in Figure 1-4(b), and the slip length is expressed as,

$$\lambda = \frac{u_s}{\left.\frac{\partial u}{\partial y}\right|_{wall}} \tag{1-5}$$

where u_s is the velocity of fluid on the wall, $\left.\frac{\partial u}{\partial y}\right|_{wall}$ is the velocity gradient on the wall. Although such an ideal case does not exist in reality since the thin air layer is not thermodynamically stable, on the SHPo surface where the gas pockets are captured inside the roughness of the surface, as shown in Figure 1-4(c), the surface will have a composite interface consisting of solid-liquid interfaces and the gas-liquid interfaces, as shown in Figure 1-4(b).

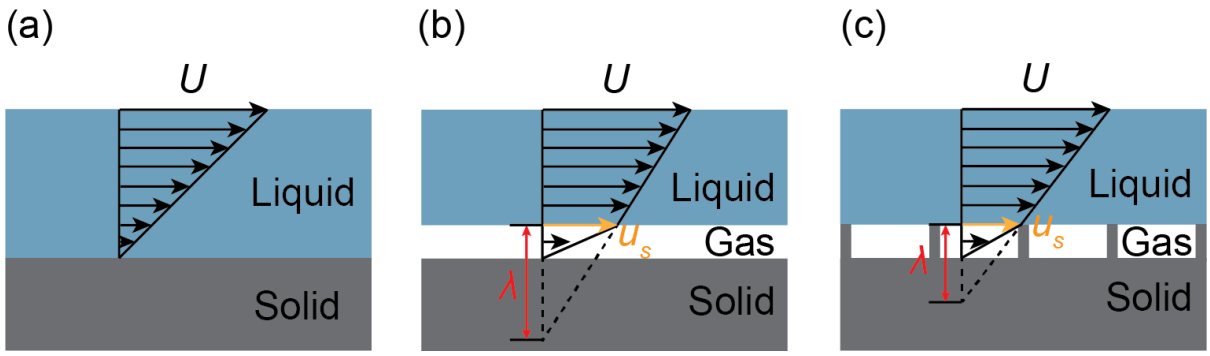

Figure 1-4. Illustration of no-slip boundary condition and slip boundary condition. (a) Liquid flows over a smooth solid surface with no-slip boundary conditions. Slip length equals zero. (b) Liquid flows over an ideal surface with a gas layer between the liquid and solid. The effective slip length on the surface would be very large. (c) Liquid flows over a structured surface where both liquid-solid and liquid-gas interfaces exist. A slip boundary condition similar to (b) will occur with an effective slip smaller than that of (b). This figure is adapted from [25].

The slip length of SHPo surface in laminar flow has been systematically studied theoretically [26-29] and experimentally [30-33]. The slip length varies with different structure patterns on the SHPo surface and depends mainly on the geometrical parameters of the pattern, such as the pitch (i.e., the periodicity length scale of the patterned structure) and the gas fraction (which equals to $1-\Phi_S$). For a given slip length, the drag reduction induced by the slip surface decreases as the characteristic size of the flow system (e.g., pipe diameter) increases [31]. Accordingly, to have a nonnegligible amount of drag reduction, the slip length of the SHPo surface has to be around or above the characteristic length scale of the flow system relevant to the desired application. The drag reduction of SHPo surface has been critically reviewed for laminar flow in Lee [25] and for turbulent flows in Park [34]. The SHPo surface with parallel collection of micro-trenches oriented along the streamwise direction (i.e., longitudinal trenches) is found to have the largest slip length.

1.2.2 Plastron State on SHPo Surface

While most of the theoretical studies assume the water-air interface on the immersed SHPo surface to be flat as shown in the common Cassie state of Figure 1-1(d), the pressure difference between the surrounding water and the plastron can cause the interface to deform, as shown in Figure 1-5. On the SHPo surface with longitudinal trenches, the pinned plastron with curved-out meniscus will have slightly increased slip length compared to the flat meniscus, while the slip length of platron with curved-in meniscus has negligible changes [35, 36]. For depinned plastron, on the other hand, if the meniscus is depinned-out, the slip length will increase slightly due to the slightly increased solid-water area, but, if the meniscus is depinned-in, the slip length may decrease dramatically (or even becomes negative) as the meniscus slides into the trench and increases to the solid-water area dramatically [35, 37]. In reality, when the depinned-out menisci spread on the top of microtrenches, they will merge with neighboring menisci and form a large plastron, which may provide a large slip length. However, such a state of large bubbles above the surface is unstable and exists only temporarily. In the field condition, most of the SHPo surface is found to have a depinned-in state due to the hydrostatic pressure, air diffusion [38, 39], high shear [40, 41], surfactant pollution [42], etc. In general, the successful application of the SHPo surface for watercraft in most realistic conditions is limited by how to achieve and maintain a proper plastron on the SHPo surface.

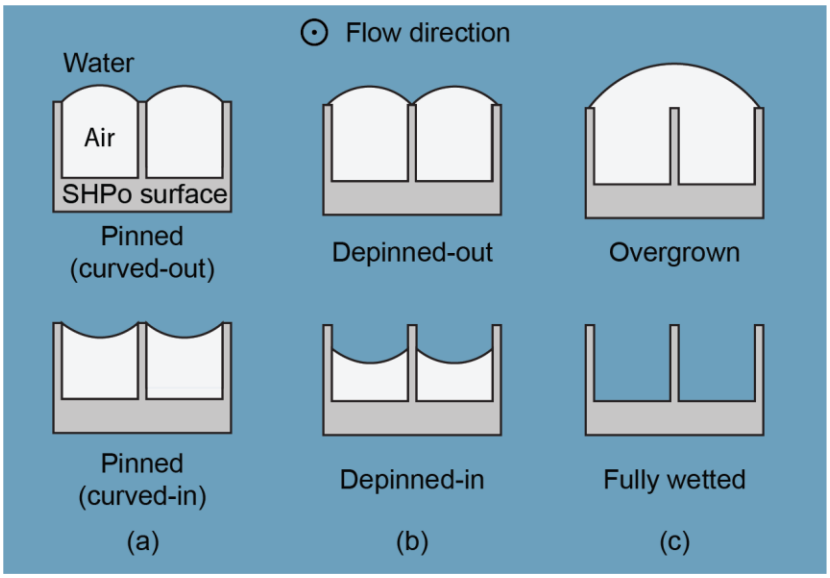

Figure 1-5. Deviation of the water-air interface from the commonly considered Cassie state under water. All the sketches describe the cross-section view of the longitudinal trenches. (a) Deformation of the meniscus at pinned state, where the meniscus is curved outwardly (top) or curved inwardly (bottom). (b) Displacement of meniscus at depinned state, where the triple-phase contact line detaches from the trench top edge and spreads on the top surface (top) or slides down on the trench sidewall (bottom). (c) Unstable or no meniscus, where the neighboring air pockets merge to form an overgrown plastron (top) or the plastron is completely depleted to reach a fully wetted state (bottom).

1.2.3 Drag Reduction in Turbulent Open Water Flow

While all numerical studies over the years [43-48] and many experimental studies in the 2010s [49-52] have reported a significant drag reduction, successful drag reduction in fully turbulent flows in open water, which represents the field condition of watercraft, has not been reported until 2020 [53, 54]. Xu [53] retrofitted a 13 foot motorboat and tested a 4 × 7 cm^2 micro-trench SHPo surface under the turbulent boundary layer of boat and achieved ~30% drag reduction with boat speed up to 10 knots (i.e., 2.3 m/s < flow seed < 5.1 m/s or 10000 s^{-1} < shear rate < 62000 s^{-1}).

While the plastron was monitored to be intact in Xu [53], Xu [54] tested the same surface in a high-speed towing tank with a higher shear flow (i.e., 6.1 m/s < flow speed < 10.1 m/s, or 55000 s^{-1} < shear rate < 140000 s^{-1}) and observed the wetting on the SHPo surface at the higher shear rate, proving the deterioration of drag reduction due to the wetted state.

1.3 Scope of Research

Due to the importance of the plastron state to the drag reduction of the SHPo surface, Chapter 2 studies the brightness of the micro-trench SHPo surface of different wetting states and focuses on discerning the depinned-in state from the pinned state, which usually requires a complicated microscopy setup that is unavailable for field condition tests. We establish a theoretical model for predicting the brightness of the depinned-in state with respect to the pinned state and the fully wetted state in different observation directions. To test the depinned-in states with various degrees of water intrusion generated on a submersed micro-trench SHPo surface, an observation stage is developed that allows us to observe the immersed surface with underwater cameras in a wide range of directions and measure the position of the meniscus via confocal microscopy. The theory is developed and confirmed by the brightness values of the different wetting states on the sample images. A convenient observation strategy is developed to allow for the accurate detection of the meniscus depinning in the field condition, such as under a motorboat, utilizing two underwater cameras. In Chapter 3, using the observation method capable of detecting the depinning-in as developed in Chapter 2, we study the state of plastron on the micro-trench SHPo surface in the high-speed flows under a real boat on open water of natural environment. The 13-foot motorboat used by Xu [53] is revamped to increase the planing stability and the speed of the boat. The increased speed was necessary to generate high enough shear rate so that shear-induced draining occurs on similar SHPo surfaces as it did in the high-speed towing tank experiment by Xu [54].

To study the wetting mechanism of the SHPo surface under the high-speed boat, we develop a unified theory by analyzing the effects of major factors causing the depinning of the meniscus in the field condition: hydrostatic pressure, air diffusion and shear. To confirm the unified theory, we design and fabricate multiple types of SHPo surfaces with different micro and nano scale structures and test them under the revamped boat in brackish water at a sea mouth. After achieving a full plastron on the entire SHPo surface at the highest boat speed, in Chapter 4, we design SHPo surfaces with different geometrical parameters to study the slip length effect on the drag reduction in a turbulent flow. By eliminating the tainted data caused by the deteriorated plastron on the SHPo surface, we report a consistent drag reduction result of longitudinal trench SHPo surfaces in the field condition as a function of the slip length normalized to turbulent wall unit. The negative effect of transverse slip on the SHPo drag reduction is verified by comparing the drag on SHPo surfaces with transverse trenches and aligned posts to that on the longitudinal trenches. Chapter 5 summarizes the dissertation and discusses the future works.

References

1. W. Barthlott and C. Neinhuis, "Purity of the sacred lotus, or escape from contamination in biological surfaces", *Planta*, 202, 1-8, 1997.
2. X. Gao and L. Jiang, "Water-repellent legs of water striders", *Nature*, 432, 36-36, 2004.
3. J.W. Bush, D.L. Hu, and M. Prakash, "The integument of water-walking arthropods: form and function", *Advances in insect physiology*, 34, 117-192, 2007.
4. M.R. Flynn and J.W. Bush, "Underwater breathing: the mechanics of plastron respiration", *Journal of Fluid Mechanics*, 608, 275-296, 2008.
5. F. Brocher, "Reserches sur la respiration des insects aquatiques adultes–les haemonia.", *Ann Biol Lac*, 5, 5-26, 1912.
6. T. Young, "III. An essay on the cohesion of fluids", *Philosophical transactions of the royal society of London*, 65-87, 1805.

7. R.N. Wenzel, "Resistance of solid surfaces to wetting by water", *Industrial & Engineering Chemistry*, 28, 988-994, 1936.

8. J. Ou, G. Fang, W. Li, and A. Amirfazli, "Wetting transition on textured surfaces: a thermodynamic approach", *The Journal of Physical Chemistry C*, 123, 23976-23986, 2019.

9. L. Joly and T. Biben, "Wetting and friction on superoleophobic surfaces", *Soft Matter*, 5, 2549-2557, 2009.

10. D. Quéré, "Non-sticking drops", *Reports on Progress in Physics*, 68, 2495, 2005.

11. A. Marmur, "The lotus effect: superhydrophobicity and metastability", *Langmuir*, 20, 3517-3519, 2004.

12. D. McMullan, "Scanning electron microscopy 1928–1965", *Scanning*, 17, 175-185, 1995.

13. Z. Guo and W. Liu, "Biomimic from the superhydrophobic plant leaves in nature: Binary structure and unitary structure", *Plant Science*, 172, 1103-1112, 2007.

14. A. Otten and S. Herminghaus, "How plants keep dry: a physicist's point of view", *Langmuir*, 20, 2405-2408, 2004.

15. K.M. Wisdom, J.A. Watson, X. Qu, F. Liu, G.S. Watson, and C.-H. Chen, "Self-cleaning of superhydrophobic surfaces by self-propelled jumping condensate", *Proceedings of the National Academy of Sciences*, 110, 7992-7997, 2013.

16. S. Zheng, C. Li, Q. Fu, M. Li, W. Hu, Q. Wang, M. Du, X. Liu, and Z. Chen, "Fabrication of self-cleaning superhydrophobic surface on aluminum alloys with excellent corrosion resistance", *Surface and Coatings Technology*, 276, 341-348, 2015.

17. P.G. Matthews and R.S. Seymour, "Diving insects boost their buoyancy bubbles", *Nature*, 441, 171-171, 2006.

18. D. Schütz and M. Taborsky, "Adaptations to an aquatic life may be responsible for the reversed sexual size dimorphism in the water spider, Argyroneta aquatica", *Evolutionary Ecology Research*, 5, 105-117, 2003.

19. D. Neumann and A. Kureck, "Composite structure of silken threads and a proteinaceous hydrogel which form the diving bell wall of the water spider Agyroneta aquatica", *SpringerPlus*, 2, 1-5, 2013.

20. J. Davenport, R.N. Hughes, M. Shorten, and P.S. Larsen, "Drag reduction by air release promotes fast ascent in jumping emperor penguins—a novel hypothesis", *Marine Ecology Progress Series*, 430, 171-182, 2011.

21. M. Leer-Andersen and S. Werner (2019), *Skin Friction database for the maritime sector.* Available: https://www.sspa.se/ship-design-and-hydrodynamics/skin-friction-

database#:~:text=Skin%20friction%20is%20responsible%20for,the%20cost%20of%20surface%20maintenance.

22. M.D. Kass, Z. Abdullah, M.J. Biddy, C. Drennan, Z. Haq, T. Hawkins, S. Jones, J. Holliday, D.E. Longman, and S. Menter, *Understanding the opportunities of biofuels for marine shipping*, Oak Ridge National Lab.(ORNL), Oak Ridge, TN (United States). 2018.

23. N. Olmer, B. Comer, B. Roy, X. Mao, and D. Rutherford, "Greenhouse Gas Emissions from Global Shipping, 2013–2015 Detailed Methodology", *International Council on Clean Transportation: Washington, DC, USA*, 1-38, 2017.

24. R. Khasawneh and K. Wallis (2016), *Shippers brace for new rules to cut deadly sulfur emissions.* Available: https://www.reuters.com/article/us-shipping-regulation-imo-idUSKCN1240KF.

25. C. Lee, C.-H. Choi, and C.-J. Kim, "Superhydrophobic drag reduction in laminar flows: a critical review", *Experiments in Fluids*, 57, 1-20, 2016.

26. J.R. Philip, "Flows satisfying mixed no-slip and no-shear conditions", *Zeitschrift für angewandte Mathematik und Physik ZAMP*, 23, 353-372, 1972.

27. E. Lauga and H.A. Stone, "Effective slip in pressure-driven Stokes flow", *Journal of Fluid Mechanics*, 489, 55-77, 2003.

28. C. Ybert, C. Barentin, C. Cottin-Bizonne, P. Joseph, and L. Bocquet, "Achieving large slip with superhydrophobic surfaces: Scaling laws for generic geometries", *Physics of Fluids*, 19, 123601, 2007.

29. A.M. Davis and E. Lauga, "Hydrodynamic friction of fakir-like superhydrophobic surfaces", *Journal of Fluid Mechanics*, 661, 402-411, 2010.

30. J. Ou, B. Perot, and J.P. Rothstein, "Laminar drag reduction in microchannels using ultrahydrophobic surfaces", *Physics of Fluids*, 16, 4635-4643, 2004.

31. C.-H. Choi and C.-J. Kim, "Large slip of aqueous liquid flow over a nanoengineered superhydrophobic surface", *Physical Review Letters*, 96, 066001, 2006.

32. J. Davies, D. Maynes, B. Webb, and B. Woolford, "Laminar flow in a microchannel with superhydrophobic walls exhibiting transverse ribs", *Physics of fluids*, 18, 087110, 2006.

33. C. Lee and C.-H. Choi, "Structured surfaces for a giant liquid slip", *Physical Review Letters*, 101, 064501, 2008.

34. H. Park, C.-H. Choi, and C.-J. Kim, "Superhydrophobic drag reduction in turbulent flows: a critical review", *Experiments in Fluids*, 62, 1-29, 2021.

35. C.J. Teo and B.C. Khoo, "Flow past superhydrophobic surfaces containing longitudinal grooves: effects of interface curvature", *Microfluidics and Nanofluidics*, 9, 499-511, 2010.

36. C.-O. Ng and C. Wang, "Effective slip for Stokes flow over a surface patterned with two- or three-dimensional protrusions", *Fluid Dynamics Research*, 43, 065504, 2011.

37. D.G. Crowdy, "Slip length formulas for longitudinal shear flow over a superhydrophobic grating with partially filled cavities", *Journal of Fluid Mechanics*, 925, 2021.

38. M. Xu, G. Sun, and C.-J. Kim, "Infinite lifetime of underwater superhydrophobic states", *Physical Review Letters*, 113, 136103, 2014.

39. P. Lv, Y. Xue, Y. Shi, H. Lin, and H. Duan, "Metastable states and wetting transition of submerged superhydrophobic structures", *Physical Review Letters*, 112, 196101, 2014.

40. J.S. Wexler, I. Jacobi, and H.A. Stone, "Shear-driven failure of liquid-infused surfaces", *Physical Review Letters*, 114, 168301, 2015.

41. Y. Liu, J.S. Wexler, C. Schönecker, and H.A. Stone, "Effect of viscosity ratio on the shear-driven failure of liquid-infused surfaces", *Physical Review Fluids*, 1, 074003, 2016.

42. J.R. Landel, F.J. Peaudecerf, F. Temprano-Coleto, F. Gibou, R.E. Goldstein, and P. Luzzatto-Fegiz, "A theory for the slip and drag of superhydrophobic surfaces with surfactant", *Journal of Fluid Mechanics*, 883, 2020.

43. T. Min and J. Kim, "Effects of hydrophobic surface on skin-friction drag", *Physics of Fluids*, 16, L55-L58, 2004.

44. K. Fukagata, N. Kasagi, and P. Koumoutsakos, "A theoretical prediction of friction drag reduction in turbulent flow by superhydrophobic surfaces", *Physics of Fluids*, 18, 051703, 2006.

45. M.B. Martell, J.B. Perot, and J.P. Rothstein, "Direct numerical simulations of turbulent flows over superhydrophobic surfaces. ", *Journal of Fluid Mechanics*, 620, 31-41, 2009.

46. H. Park, H. Park, and J. Kim, "A numerical study of the effects of superhydrophobic surface on skin-friction drag in turbulent channel flow", *Physics of Fluids*, 25, 110815, 2013.

47. A. Rastegari and R. Akhavan, "On the mechanism of turbulent drag reduction with super-hydrophobic surfaces", *Journal of Fluid Mechanics*, 773, 2015.

48. H.J. Im and J.H. Lee, "Comparison of superhydrophobic drag reduction between turbulent pipe and channel flows", *Physics of Fluids*, 29, 095101, 2017.

49. R.J. Daniello, N.E. Waterhouse, and J.P. Rothstein, "Drag reduction in turbulent flows over superhydrophobic surfaces", *Physics of Fluids*, 21, 085103, 2009.

50. R.A. Bidkar, L. Leblanc, A.J. Kulkarni, V. Bahadur, S.L. Ceccio, and M. Perlin, "Skin-friction drag reduction in the turbulent regime using random-textured hydrophobic surfaces", *Physics of Fluids*, 26, 085108, 2014.

51. H. Park, G. Sun, and C.-J. Kim, "Superhydrophobic turbulent drag reduction as a function of surface grating parameters", *Journal of Fluid Mechanics*, 747, 722-734, 2014.

52. J.W. Gose, K. Golovin, M. Boban, J.M. Mabry, A. Tuteja, M. Perlin, and S.L. Ceccio, "Characterization of superhydrophobic surfaces for drag reduction in turbulent flow", *Journal of Fluid Mechanics*, 845, 560-580, 2018.

53. M. Xu, A. Grabowski, N. Yu, G. Kerezyte, J.-W. Lee, B.R. Pfeifer, and C.-J. Kim, "Superhydrophobic drag reduction for turbulent flows in open water", *Physical Review Applied*, 13, 034056, 2020.

54. M. Xu, N. Yu, J. Kim, and C.-J. Kim, "Superhydrophobic drag reduction in high-speed towing tank", *Journal of Fluid Mechanics*, 908, A6, 2021.

Chapter 2 Brightness of Microtrench Superhydrophobic Surfaces and Visual Detection of Intermediate Wetting States

The materials in this chapter have mostly been published in [1, 2].

2.1 Introduction

A superhydrophobic (SHPo) surface would transition from the dewetted to wetted state when water intrudes into the surface roughness or from the wetted to dewetted state when the trapped air grows in the roughness, depending on hydrostatic pressure and dissolved air concentration, among others [3]. The transitions may be categorized by the position of the air-water-solid contact lines, as schematically illustrated in Figure 2-1 [4], where the roughness is drawn as a regular microstructure for simplicity, and the states of overgrown air above the roughness are added to be complete. Because most underwater applications of SHPo surfaces, such as drag reduction [4-7] and anti-biofouling [8, 9], require the surface roughness to be substantially filled with an air layer, called plastron [10], it is highly desirable that the SHPo surface stays dewetted under water. Since the overgrowing air, Figure 2-1(b), usually causes the contact lines to detach from the surface, leading to the overly dewetted state of Figure 2-1(a), which is unstable, for most applications the desired state is the properly dewetted state of Figure 2-1(c), which is commonly regarded as Cassie-Baxter state. We said "commonly" because Figure 2-1(d) also belongs to the composite interface considered by Cassie and Baxter [11, 12]. This rather casual and imprecise naming is widespread because the intermediate states are usually not apparent or addressable.

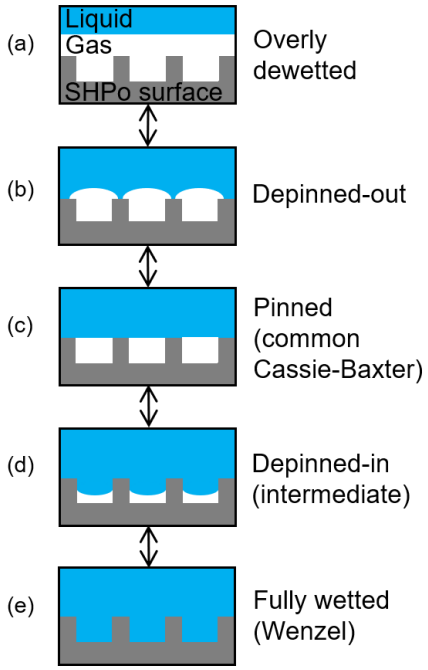

Figure 2-1. Various wetting states of a submerged SHPo surface. The current report aims to detect the depinned-in state (d), which is intermediate between the pinned state (c) and the fully wetted state (e), on microtrench SHPo surfaces. The depinned-in state (d) can appear either silvery bright like the pinned (c), dark black like the fully wetted (e), or greyish between bright and dark, depending on the water intrusion depth and observer's viewing directions.

Most times, the dewetted states, Figure 2-1(a-d), are visually distinguishable by the bright silvery sheen due to the total internal reflection (TIR) of light at the water-air interface. In contrast, the fully wetted state, Figure 2-1(e), known as Wenzel [13] state appears dark, because with no water-air interface light reaches the inner surfaces of the surface roughness and gets scattered. This first-order information whether the SHPo surface is dewetted (appearing bright) or fully wetted (appearing dark) is good enough for some applications, where the intermediate states between the dewetted and fully wetted states are transient and ignorable. However, for other applications, where the intermediate states are important and not transient, the second-order information, such

as the intermediate state of wetting shown in Figure 2-1(d), may further be necessary. For example, the intermediate wetting state with the air-water contact line depinned from the roughness top edge, as illustrated by Figure 2-1(d), may persist instead of jumping to the fully wetted state of Figure 2-1(e) in some hydrodynamic conditions [4, 14]. In particular, recent studies found that, while both may appear bright, the pinned state of Figure 2-1(c) may entail significant drag reduction but the depinned-in state of Figure 2-1(d) may not and even invoke drag increase [15, 16] expected of the fully wetted state of Figure 2-1(e), leading to some inexplicable results in the field of SHPo drag reduction [4, 17]. To avoid such a major pitfall, one needs to know which sub-states of the dewetted state (while all appearing bright) a SHPo surface is in. More specifically, this chapter seeks to distinguish the depinned-in state of Figure 2-1(d) from the pinned state Figure 2-1(c) on a SHPo surface made of parallel microtrenches. Furthermore, we show the depth of water intrusion can be quantitatively estimated by observing the sample surface with a series of viewing angles. The other intermediate wetting state, i.e., the depinned-out state (Figure 2-1(b)) is between the pinned state (Figure 2-1(c)) and the overly dewetted state (Figure 2-1(a)), is not considered in this chapter.

Over the past decade, numerous methods have been utilized or developed to find the shape and position of the water-air interface on SHPo surfaces. The most widely used for its convenience is the bright silvery appearance, which simply indicates the existence of plastron on an immersed SHPo surface [18-22]. Additional details would require some instrumentation. Rathgen [23] measured the diffraction pattern of reflected light to detect the detailed meniscus shape on parallel microtrenches. Acoustic sensing [19, 24], quartz crystal microbalance [25], and transmission small-angel x-ray scattering [26] were utilized to detect the intrusion depth (wetting depth) of water into surface roughness. On the other hand, a variety of strategies have been used for direct visualization of the water-air interface on the SHPo surface, including optical microscopy [3, 27,

28], confocal microscopy [29-32], atomic force microscopy [33-35], environmental scanning electron microscopy [36], X-ray computed tomography [37, 38], micro particle image velocimetry [39], and freeze fracturing approach [40, 41]. Unfortunately, however, they are not suitable or convenient for large samples or general field studies (e.g., boat on the sea [6], model in a towing tank [42, 43], where the SHPo surface of interest may travel at high speed under water and cannot accommodate the installation of any bulky instrument.

Considering field experiments of SHPo drag reduction as a prominent example, in this paper we propose and confirm a strategy to detect the intermediate wetting – distinguish the depinned-in state (Figure 1(d)) from the pinned state (Figure 1(c)) in particular – on SHPo surfaces without special instrumentation. Periodic microtrenches aligned to the flow direction are of the prime interest because they have recorded the largest slip lengths (up to 400 μm) [6, 17, 43], the largest drag reductions in a water tunnel (up to 75%) [44], and so far the only successful drag reduction (~30%) for highly turbulent flows in open water [6]. This chapter was initiated by our long frustration of not being able to interpret the results in the literature properly without knowing whether the bright plastron reported in all the successful experiments was indeed in the depinned state Figure 2-1(c) or mixed with the depinned-in state of Figure 2-1(d). More specifically, for an amount of drag reduction reported, how much of the SHPo surface was bright and properly dewetted to fully contribute to drag reduction and how much was bright but in intermediate states to compromise the reduction? The strategy proposed in this chapter to address this challenge was based on our own disturbing experience that a depinned-in state with a relatively small but non-negligible intrusion depth would appear as bright as the pinned state and motivated by our impromptu observation that the same surface could appear dark if seen with a very small elevation angle. Encouraged by a qualitative proof-of-concept with naked eyes [1], in this chapter we

establish a geometric model that mathematically relates how the surface brightness is affected by the water intrusion depth and observer's viewing angles and then perform a series of viewing tests using three underwater cameras and a confocal microscope simultaneously to quantitatively assess the proposed scheme. The strategy is being utilized for our flow studies in field conditions, following the recent report of SHPo drag reduction tested under a 13-foot motorboat in the open sea – an exemplary field condition.

2.2 The Concept and Theorization

2.2.1 Bright Ratio and Intrusion Ratio of SHPo Surface

Between the pinned (i.e., common Cassie-Baxter) state of Figure 2-1(c) and the fully wetted (i.e., Wenzel) state of Figure 2-1(e) under water, a SHPo surface would appear the brightest at the former and the darkest at the latter. Since SHPo surfaces appear bright by the total internal reflection (TIR) of the water-air interface on the plastron, let us simplify the discussion by assuming TIR dominates the light reaching the viewer, i.e., ignoring all other lights, for now. To explain the underlying concept and proposed strategy, it helps to define the observation direction of a viewer (e.g., camera, person) with the elevation angle β and azimuth angle φ with respect to the sample surface and transverse trench direction, respectively. Figure 2-2(a) shows β and φ in a rectangular coordinate system, where the x direction is parallel to the trenches, y direction is normal to the sample surface, and the z direction is transverse to the trenches, with the coordinate origin as the center of observation and the yellow arrow pointing to the viewer. As far as this report is concerned, the elevation angle is $0 \leq \beta \leq 41.4°$ for TIR on the flat water-air interface, and the azimuth angle is $0 \leq \varphi \leq 90°$ due to the symmetry of parallel trenches. In addition to assuming (i) TIR dominates the light, we further assume: (ii) the water-air interface is flat inside the trench, (iii)

the lighting is diffusive, and (iv) the viewer is far from the surface so that the observation angles are uniform throughout the surface of interest. The first and second assumptions will be discussed later in this section, and the third and fourth assumptions will be explained in the next section. For a SHPo surface with periodic trenches, let us define their pitch (periodicity) as p, width as w, and depth as d. Figure 2(b) shows a trench cross-sectioned along the plane of incidence, defining azimuthal pitch $p' = p/\cos\varphi$ and azimuthal width $w' = w/\cos\varphi$. Note that the azimuthal width of the trench coincides with the actual width when $\varphi = 0°$ and increases with φ. The degree of water intrusion into the trench, i.e., intrusion depth h, is defined as the vertical distance between the trench top edge and the solid-water-air three-phase contact line on the trench sidewall. The intrusion depth h can be normalized by the trench depth d as intrusion ratio $h^* = h/d$ so that the pinned state has $h^* = 0$, the depinned-in state has $0 < h^* < 1$ and the fully wetted state has $h^* = 1$. Since the sidewalls (assuming an opaque material) of the trench would block the light, as shown in Figure 2(b), the portion of meniscus available for TIR to the viewer for a given observing direction is w_T'. The meniscus width providing TIR can be expressed as:

$$w_T' = w' - h / \tan\beta \tag{2-1}$$

The brightness μ (seen to the viewer) of a microtrench SHPo surface under water would be determined by the areal ratio between the meniscus of TIR visible to the viewer and the entire SHPo surface, i.e., w_T'/p', because for now all other areas of the surface are assumed to appear completely dark. Furthermore, for this report it is more relevant and useful to express the brightness relative to the brightness possible on a given SHPo surface, i.e., with a given gas fraction (w/p), i.e., as the bright ratio:

$$\mu^* = \frac{\mu - \mu_{fully\ wetted}}{\mu_{pinned} - \mu_{fully\ wetted}} = \frac{w_T}{w} = w_T' \tag{2-2}$$

where μ_{pinned} and $\mu_{fully\ wetted}$ indicates the brightness of the pinned and the fully wetted state, respectively. For a given SHPo surface and excluding the depinned-out or overly dewetted from consideration, the pinned state would appear the brightest, i.e., $\mu^* = 1$, because all of the water-air menisci on the SHPo surface sends TIR light to the viewer, while the fully wetted state would appear the darkest, i.e., $\mu^* = 0$, because there is no meniscus for TIR.

Accordingly, we define TIR ratio w_T^* as the TIR region w_T relative to the entire meniscus w, i.e., $w_T^* = w_T'/w' = w_T/w$, and the brightness ratio equals the TIR ratio by definition, i.e., $w_T^* = \mu^*$.

During the intermediate state transitioning from the pinned to fully wetted state, for a given observing direction, the depinned-in state gradually changes from bright to dark since w_T^* decreases when the meniscus slides down into the trench, as shown in Figure 2-2(c). If w_T^* is large enough to make the surface appear quite bright, the intermediate surface is perceived to be dewetted, i.e., $\mu^* \sim 1$. If w_T^* becomes small enough to make the surface quite dark, the intermediate surface is perceived to be fully wetted, i.e., $\mu^* \sim 0$. This simple choice of either depinned or fully wetted has been widely adopted in practice without any better options unless special instrumentation was used.

The brightness of the depinned-in state is affected not only by the water intrusion depth but also by the observing directions. Figure 2-2(d) illustrates, for a given intrusion depth h and elevation angle β, that the surface will appear from dark to bright as the azimuth angle φ increases because the TIR ratio w_T^* increases. Similarly, Figure 2-2(e) illustrates, for a given intrusion depth h and

azimuth angle φ, that the surface will appear from dark to bright as the elevation angle β increases because w_T^* increases.

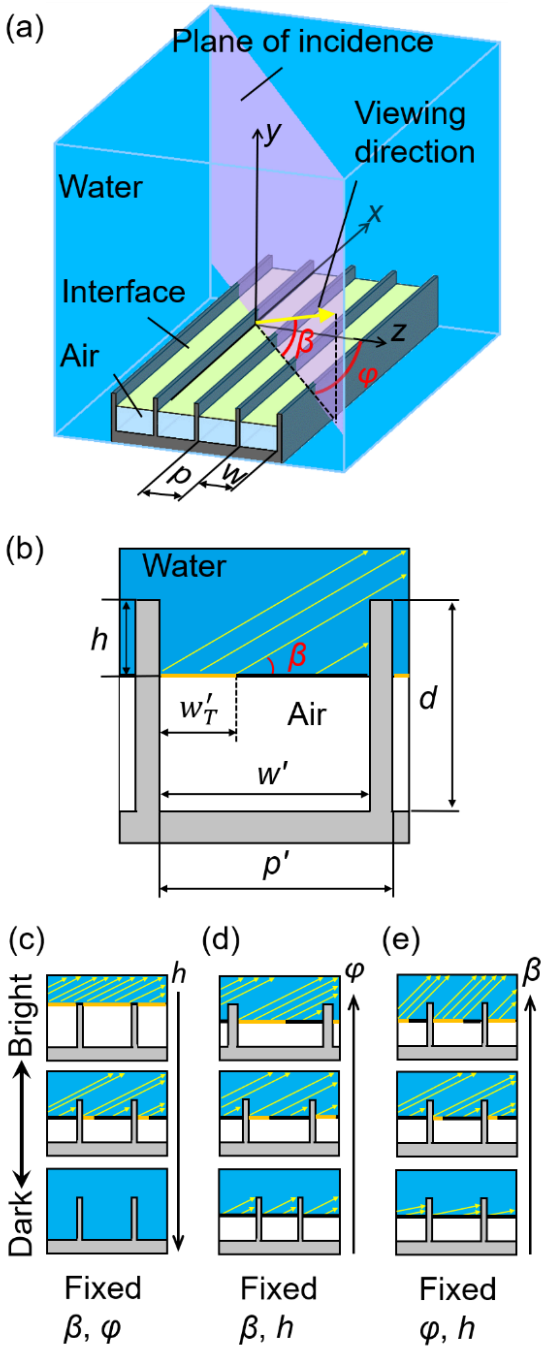

Figure 2-2. The proposed relationship between the viewing direction and surface brightness of a microtrench SHPo surface.(a) The viewing direction (yellow arrow) is defined by two angles:

elevation angle β with respect to the sample surface (xz plane) and azimuth angle φ of the incidence plane to the transverse trench direction (z-axis). The trenches have pitch p and width w. Drawn not to scale for clarity. (b) The water-air interface inside a trench cross-sectioned along the plane of incidence. The yellow arrows indicate TIR off the meniscus towards the viewer. The red portion would be visible and appear bright to the viewer. (c) TIR towards the viewer for pinned, depinned-in, and fully wetted state. (d, e) TIR towards the viewer detailed for a depinned-in state shows the effect of azimuth angle φ (d) and elevation angle β (e).

Recall the first assumption for the above theory that all the lights reaching the viewer are from TIR, ignoring all other lights. However, since other lights are often not negligible (for example, the solid surfaces on the trench top and sidewall may not be completely dark), a deviation from the above theory is expected. Regarding the fully wetted state, the 30-40% reflection on the silicon surface in water [45] is much weaker than the 100% reflection by TIR on the water-air interface but still significant. However, in most cases, the light reflects off the water-silicon interface multiple times (e.g., reflections on the sidewall, bottom, then the other sidewall) before only a few percent reaches the viewer. The main deviation from the negligible non-TIR assumption is for large azimuth angle φ, for which the light may reflect the water-silicon interface only once (on the trench bottom) before 30-40% reaching the viewer, as will be discussed later with the experimental results. Other non-TIR reflections include those on the trench top surfaces, which increase with the solid fraction of SHPo surface, and those on the trench sidewalls above the water-air interface for depinned-in cases, which increases with intrusion depth. For the current study, which employed typical silicon micromachining, the 10% solid fraction of the top surfaces and the roughness on sidewall surfaces make the non-TIR reflection on them negligibly small. While the absolute brightness μ is further affected by various other factors (e.g., reflection on other surfaces around

the sample, the exposure of the camera, the background light intensity), what really matters to the observer is the brightness relative to those on the pinned and the fully wetted surface on the same sample location at the same observation event. Accordingly, the brightness ratio μ^* will play a main role in the proposed strategy.

Utilizing the fact that the pinned state appears the brightest (i.e., $\mu^* = 1$) and the fully wetted state appears the darkest (i.e., $\mu^* = 0$) for any φ and β, let us discuss how the intrusion depth h can be obtained from the brightness ratio μ^* and the observation angles φ and β. Utilizing $w_T^* = \mu^* = w_T'/w'$ and $h^* = h/d$, Equation (2-1) be rearranged to be:

$$h^* = \left(1 - \mu^*\right) \frac{w \tan \beta}{d \cos \varphi} \tag{2-3}$$

where $0 \le \beta \le 41.4°$, $0 \le \varphi < 90°$, $0 \le \mu^* \le 1$ and $0 \le h^* \le 1$. Equation (2-3) indicates that, in theory, one can estimate h^* by just measuring μ^* for any viewing direction φ and β. However, in reality, the brightness measurement was found unreliable with scattered data when the brightness ratio was close to the two ends ($\mu^* \sim 0$ or 1), as will be shown later in the experimental results. To avoid the limitation, we propose a better strategy is to assign a target value away from 0 and 1 for μ^* and find φ and β that result in the target value of μ^*. An obvious choice would be a middle point, i.e., $\mu^* = 0.5$, which reduces Equation (2-3) to:

$$h^* = \frac{w \tan \beta}{2d \cos \varphi} \tag{2-4}$$

In fact, $\mu^* = 0.5$ will be found effective in the experiments in the next sections. In other words, Equation (2-4) establishes a relationship between intrusion ratio h^* and observing angles β and φ when the surface appears half-bright and half-dark.

2.2.2 Effect of Meniscus Curvature

When the meniscus is curved (bent), mostly into the trench by the water pressure, the reflecting angle on the meniscus to the viewer deviates from the elevation angle because the tangential line angles from the horizontal line by the curvature, as illustrated in Figure 2-3. Note the deviation of the curved meniscus from the horizontal line increases near the sidewall. If the deviation is large enough to make the reflection angle out of the TIR range, the surface would appear dimmer overall. Figure 2-3 is drawn for the surface being viewed perpendicularly to the trench direction, i.e., φ = 0°, for which the meniscus curvature in the plane of the incident is the most prominent and, thus, dimming by the curvature would be the most significant.

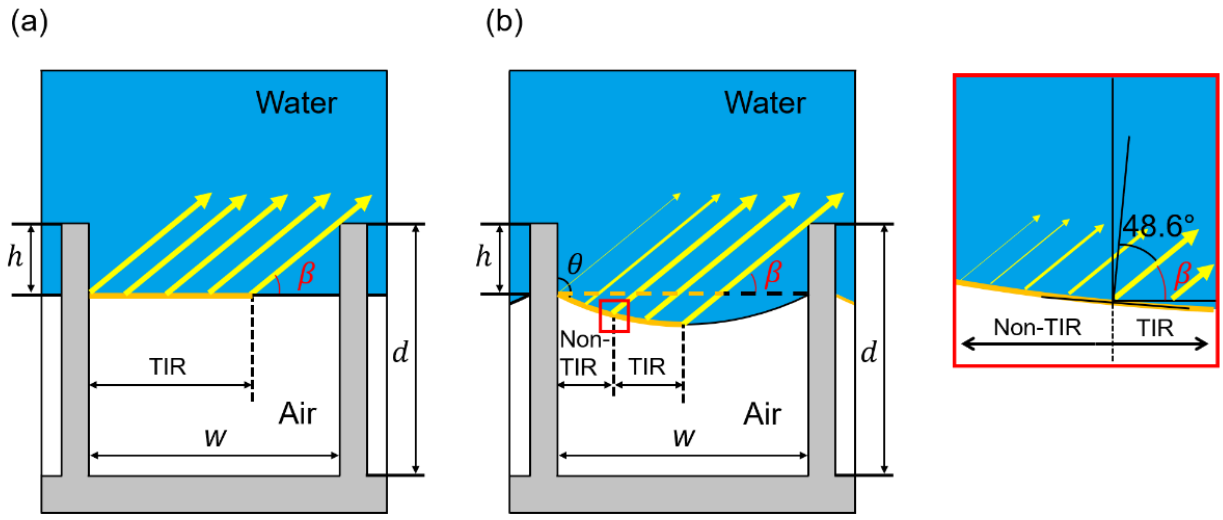

Figure 2-3. Meniscus curvature effect on brightness. Cross-trench profiles (i.e., φ = 0°) of a depinned state with (a) flat and (b) curved meniscus, indicating the reflection light to the viewers at β. The contact angle of water on the sidewall is defined as θ. The thickness of the arrows indicates the reflectance at the corresponding spot. The inset magnifies the area on the curved meniscus where the reflection starts losing the TIR by the curvature.

The water is depinned and slides down the sidewall once the contact angle θ on the sidewall reaches the advancing contact angle θ_a. Under a given elevation angle β, the two (flat and curved) menisci have the same projected area (length) toward the viewer. However, the curved meniscus may have a portion where the angle of incidence is smaller than the critical angle of incidence for TIR with its reflectance R diminished according to the Fresnel equations [45].

$$R = \frac{1}{2}\left[\left(\frac{n_i \cos\theta_t - n_t \cos\theta_i}{n_i \cos\theta_t + n_t \cos\theta_i}\right)^2 + \left(\frac{n_i \cos\theta_i - n_t \cos\theta_t}{n_i \cos\theta_i + n_t \cos\theta_t}\right)^2\right] \tag{2-5}$$

where n_i is water's index of refraction, 1.33, n_t is air's index of refraction, 1, θi is the angle of incidence, θ_t is the angle of reflection, and $n_i \sin\theta_i = n_t \sin\theta_t$ by the law of reflection, resulting in the following relation between R and θi. Equation (2-5) is graphically presented in Figure 2-4 for the water-to-air interface. The effect of the meniscus curvature on the observation results will be discussed in the Section 2.4.3.

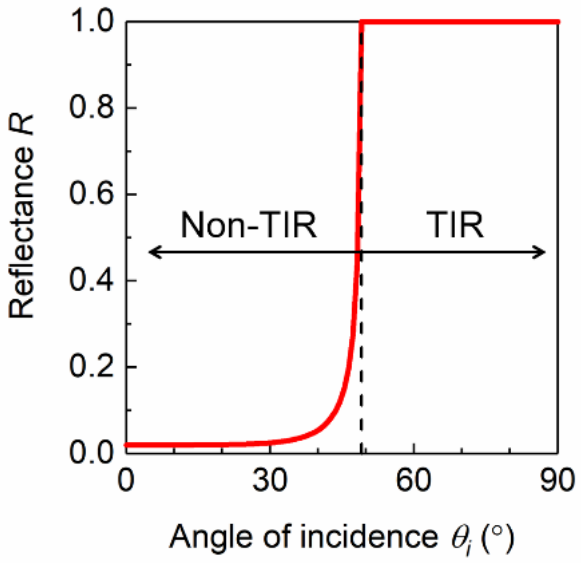

Figure 2-4. Reflectance of light for a water-to-air interface. The dashed line shows the critical angle of incidence for TIR, i.e., θ_i = 48.6° for water-to-air.

2.3 Experimental Section

2.3.1 Sample Preparation

A large series of experiments was performed to put the underlying concept and theory formalized above to the test, using SHPo surfaces decorated with periodic microtrenches. After creating depinned-in states at 4 different intrusion ratios, a range of observation directions that make the surface appear to be $\mu^* = 0.5$ were found and compared with the intrusion ratios through Equation (2-4). Periodic parallel microtrenches were fabricated on a 4-inch (500 μm-thick) silicon wafer covered with a 1 μm-thick silicon dioxide layer using photolithography and deep reactive ion etching in the Nanoelectronics Research Facility of the University of California, Los Angeles (UCLA). After the etching, the wafer was cleaned in piranha solution (sulfuric acid: hydrogen peroxide = 4 : 1) for 10 minutes, rinsed by deionized (DI) water, and blown dry by a nitrogen gun. After the wafer was diced to a square sample (1.3 cm x 1.3 cm including the 1.0 cm x 1.0 cm test area), the samples were cleaned, rinsed, and spin-coated with Teflon AF to make the surface SHPo. The 1.3 cm × 1.3 cm sample has a 1.0 cm × 1.0 cm testing area full of microtrenches in the middle, as shown in Figure 2-5(a), outside which is smooth. The microtrenches have pitch p = 100 μm, width w = 90 μm, and depth $d \approx 90$ μm. The apparent contact angle of water on the fabricated SHPo surface was measured to be 154° (viewed transversely to the trenches) with a tilting angle smaller than 1° in all directions, showing the characteristics of a SHPo surface. The sketches illustrating the fabrication process are shown in Figure 2-5(b).

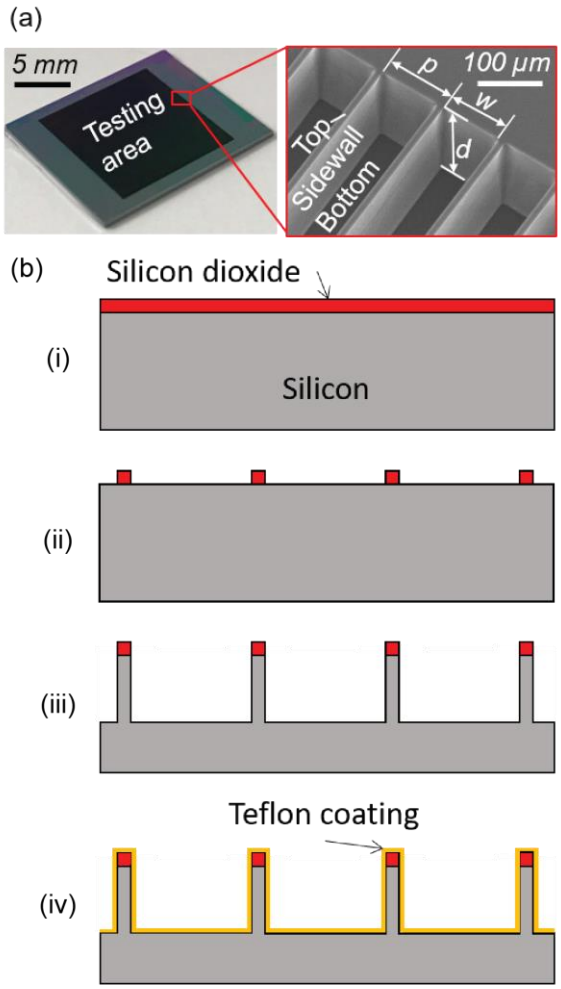

Figure 2-5. Images and fabrication process for the SHPo surface with parallel microtrenches.(a) Optical image of the prepared SHPo surface sample with parallel microtrenches. The inset SEM image shows an end region of the microtrenches and their pitch *p*, width *w*, and depth *d*. (b) The fabrication process for microtrenches SHPo surface. (i) Grow a 1 μm silicon dioxide layer on a silicon wafer by wet thermal oxidation. (ii) Use photolithography and reactive ion etching (RIE) to pattern parallel lines of the silicon dioxide layer. (iii) Using the silicon dioxide lines as an etching mask, form 90 μm-wide and ~90 μm-deep microtrenches of 100 μm pitch by deep reactive ion etching (DRIE), which creates nearly vertical, rough sidewalls. (iv) After wafer dicing, spin coat 2 wt% AF1600 (Chemours) Teflon solution (solvent: FC-40, Sigma-Aldrich) at 1000 rpm for 30

seconds and bake the sample on the hotplate at 165 °C for 15 minutes and then at 335 ºC for 15 minutes.

2.3.2 Optical Microscopy

For the experiments, the sample was placed on a rotational stage in an acrylic container, which was slowly filled with deionized (DI) water, as shown in Figure 2-6. The fluorescent tubes on the ceiling were the main source of lighting during the experiments, and the container was covered with diffuse paper to achieve diffused lighting of the fourth assumption in the previous section. In field conditions, such as underneath watercraft below the wavy water surface, the sunlight is usually dispersed enough to be considered diffusive.

To study the appearance of the microtrench SHPo surface in water, three miniature underwater cameras (7mm 5M Micro USB OTG Endoscope, Ehome) were used, as shown in Figure 2-6(a). Each camera has an IP 67 rating waterproof cylindrical case with a USB cable to transfer real-time images to a computer on the go (OTG). The position and tilting of each camera were carefully adjusted so that the sample was within the focal distance and at the center of view for all cameras. Note the *yz* coordinates in Figure 2-6(a) imply it is drawn for $\varphi = 0°$. In our tests, three cameras were held at three positions of $\beta = 10 \pm 0.3°$, $20 \pm 1°$, $30 \pm 2°$, where the plus-minus deviation covers the width of the testing area. By rotating the rotational stage around the y axis, φ can be quickly set to any value between 0° and 90° with ±2° at the two ends of the tested area, following the fourth assumption in the previous section with minimal deviations.

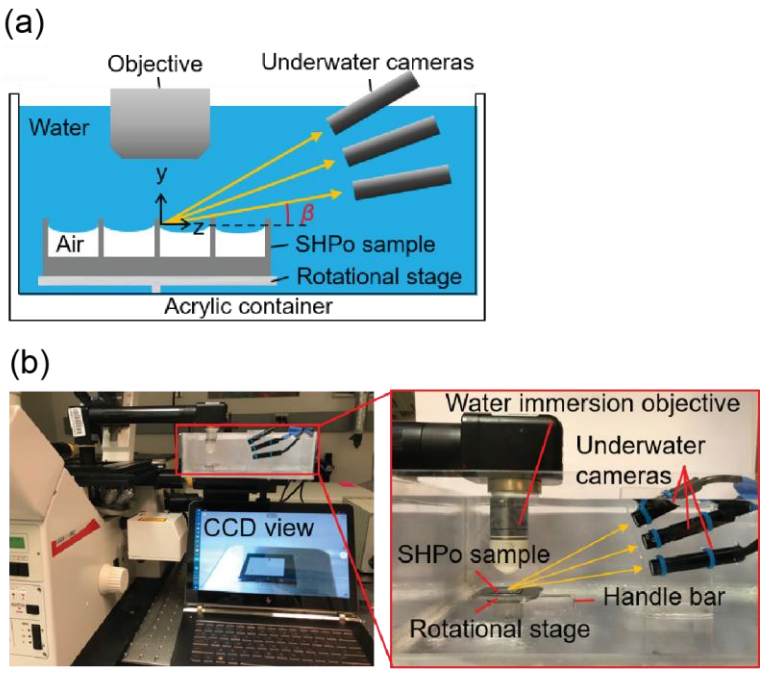

Figure 2-6. Experimental setup with the confocal microscope. (a) Sketch of the experimental setup consisting of a sample and three cameras (not drawn to scale for clarity). Yellow arrows indicate the directions of cameras observing the sample surface. The objective lens is part of the confocal microscope. The cameras are ~8 cm away from the 1 cm × 1 cm testing area. The elevation angle β is labeled for the lowest camera. (b) Images of the experimental setup. The inset picture shows more details with the yellow arrows indicating the observing directions of the three cameras: β = 10° (bottom), 20° (middle), 30° (top).

2.3.3 Controlled Wetting

We achieved several wetting states on one sample and conducted observation tests with large sets of parameters in one immersion, as follows. Water was degassed by boiling it for 30 minutes and cooling it down to room temperature in 2 hours. The air concentration in the prepared water was measured to be ~40% by the Total Gas Pressure meter (Point Four™ Tracker, Pentair). The sample was kept at 35 mm below the water surface throughout the immersion tests, letting the gas diffusion

between the water and trapped air control the wetting states. The confocal microscopy experiments were performed in a suite specially designed for environmental control (low vibration, air-filtered, air conditioned to ±1°C, light-tight, etc.). Although there was no control system for humidity, the humidity level was measured by a hygrometer and found to be 50±2% throughout the experiments. We generated three different wetting states – pinned, depinned-in, and fully wetted – simultaneously on one sample, as follows. In the water with 40% of air saturation, the trenches immediately started to lose the trapped air, transitioning from the pinned to the depinned-in state. The water-air meniscus slid deeper into the trenches slowly and uniformly with the immersion time, reaching the fully wetted state in about 16 hours for the current trench geometry and air concentration in theory without environmental variation [3]. However, the transition during the test was found to be faster than the theory, i.e. ~3 hours for reaching $h^* = 0.8$, due to the disturbance from the handling process when the sample was rotated for imaging. To maintain both a pinned region and a fully wetted region while inducing a depinned-in region with slowly increasing intrusion depth, i.e., all three states simultaneously, on the same sample, we played tricks with a pipette, providing air to locally maintain a pinned state and injecting water to locally create a fully wetted state. After the sample was covered with water at the beginning, a ~2 mm-diameter air bubble was pipetted on one region of the sample surface, making the air pockets of several neighboring trenches merge with the pipetted bubble. Replenished with air from the 2 mm bubble as needed by the Laplace pressure, the trenches underneath the bubble remained in a pinned state. If the air bubble was depleted (consumed) before the testing ended, a new air bubble was pipetted in the same location to prolong the pinned state. On the other hand, to create a fully wetted state immediately (vs. otherwise ~16 hours to reach the fully wetted state naturally), water was squirted into microtrenches towards their ends, pushing the trapped air out of the trenches.

2.3.4 Confocal Microscopy

All three wetting states created as described above were analyzed with a confocal microscope and observed with three underwater cameras in one experiment. To monitor the meniscus location accurately, i.e., measure the intrusion depth h, a real-time confocal microscope (TCS-SP2-MP-FLIM, Leica) was employed. A U-shape beam was used to allow observation of the meniscus from the top, utilizing a 63× water immersion objective (Leica HCX L APO 63X, WD = 0.9 mm). In one scanning test, the starting plane (the bottom of the meniscus) and the end plane (top of the trenches) were firstly detected and defined manually by adjusting the lens height in z-wide reflection mode (wavelength = 543 nm). Then, a series of spatial images in reflection mode was taken between the two planes and integrated to build the 3D model of the meniscus and grating top (i.e., top edge of trenches), from which the exact shape and position of the meniscus could be constructed. Right after each confocal scanning, a series of pictures were taken by three cameras for φ varying from 0° to 90° with 5° intervals, during which the contact line movement was negligible. Since each scanning took 5–10 minutes and the imaging process of the camera took ~1 minute, the sliding down of the meniscus during the measurement could cause variations of only 0.05 on the measured intrusion ratio h^*. All the pictures taken by the underwater camera were converted to greyscale without any adjustment on contrast and brightness. The camera exposure settings and background lighting were kept the same during all the tests. One image was taken for each set of 4 water intrusion depths, 3 camera elevation angles, and 19 camera azimuth angles, amounting to 228 sets of test parameters in total. One sample was used to test $h^* = 0.24, 0.36, 0.57$, and another sample was used to test $h^* = 0.78$. For each of the above 228 images, brightness data from the three wetting states were obtained by reading the average brightness on a region of 3×3

pixels (around 0.5 mm × 0.5 mm) using an image processor (Adobe Photoshop) for each state, amounting to 684 data points in total.

2.3.5 Calibration of Underwater Camera Field of View

The experimental work in this subsection has been performed by Ms. Sarina Kiani. The camera's viewing angles with respect to the sample surface play a key role in the current report. Ideally, the centerline of the camera's field of view (FOV) should coincide with the centerline of the camera's cylindrical case so that we can utilize the centerline of the camera case to characterize the observing angles on the sample surface. However, due to the imperfect manufacturing, the centerlines of FOV are misaligned with the centerline of the camera case, as illustrated in Figure 2-7(a). The CCD of the camera could be shifted away from the center and tilted slightly off the centerline, leading to two types of misalignment: transitional misalignment T (unit: mm) and angular misalignment a (unit: degree). To find T and a for each camera, we developed a calibration setup shown in Figure 2-7(b). The camera is connected to the PC to show its rectangular FOV, as shown in Figure 2-7(c), which is then sketched out with pencils on a piece of paper that the camera is pointing at. The center of FOV is the intersection point of two diagonal lines of the rectangle. By rotating the camera multiples times with respect to the centerline of its case at a 90° interval, we can find the circular path around the center point of its FOV, as shown in Figure 2-7(d). The radius r_c of the circle is related to the distance of the camera to the paper L_c and the misalignment of the camera T and a:

$$r_c = T + L_c \tan a \tag{2-6}$$

By measuring r_c at different distances L_c, the misalignment of each camera used in the experiments is summarized in Table 2-1. The misalignment of the camera is taken into consideration when installing the camera for desired observing angles in our experiments.

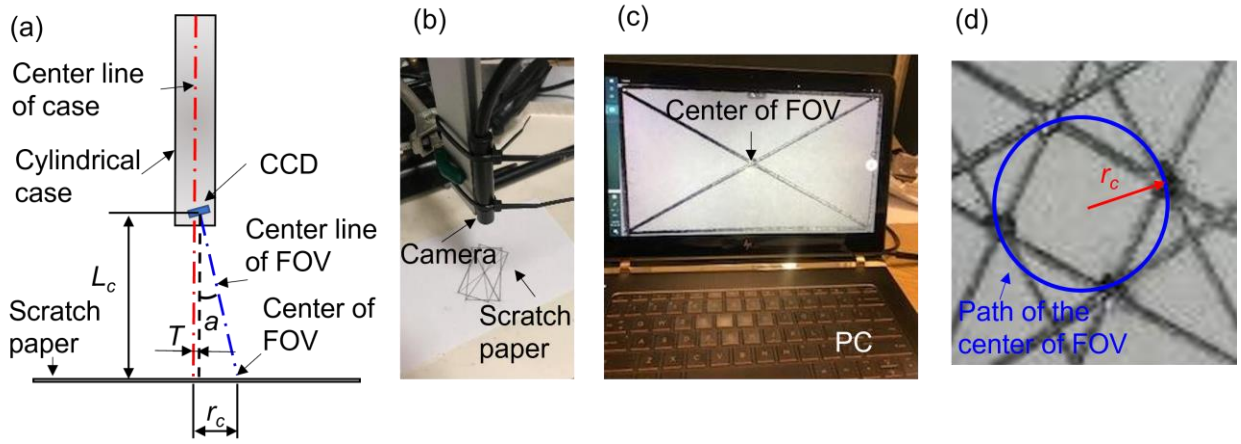

Figure 2-7. Camera field of view calibration illustration. (a) Illustration of misalignment. The misalignments are exaggerated for clarity. (b) The camera attached to a vertical stand looking at line patterns drawn on paper. (c) The center of the camera field of view (FOV) is identified on a PC. (d) Path of the center of FOV. The blue circle is the path, interpreted from the 4 center points of FOV when the camera is rotated at 90° intervals to create 4 overlapped images.

Table 2-1. The transitional and rotational CCD misalignments. The values in the table were used to calibrate the camera's position with respect to the SHPo surface sample.

Position	Transitional misalignment T (mm)	Angular misalignment δ (°)
Camera 1	0.05	1.38
Camera 2	0.29	2.63
Camera 3	0.00	3.34

2.4 Results and Analysis

2.4.1 Brightness vs. Observation Angles

Among the 12 sets of images collected from the three cameras (β = 10°, 20°, 30°) to view the four intrusion ratios (h^* = 0.24, 0.36, 0.57, 0.78) during the above experiments, the one set for β = 20° and h^* = 0.57 is presented in Figure 2-8 as an example. The confocal image of the given intermediate state is shown in Figure 2-8(a) along with those at the pinned and fully wetted states as references: pinned (h^* = 0.00), depinned-in (h^* = 0.57), and fully wetted (h^* = 1.00). Figure 2-8(b) presents a series of greyscale pictures taken by the camera at elevation angle β = 20° with 10 sequentially varying azimuth angles (φ = 0°, 5°, 10°, …, 90°). On each of the 10 pictures, where three colored symbols relate the specified portions to the three different wetting states shown in Figure 2-8(a), brightness was measured for each of the three states. Note the depinned-in state of h^* = 0.57 appears as bright as the pinned state at φ = 90° but becomes slightly darker at φ = 80° and as dark as the fully wetted state when φ < 50°.

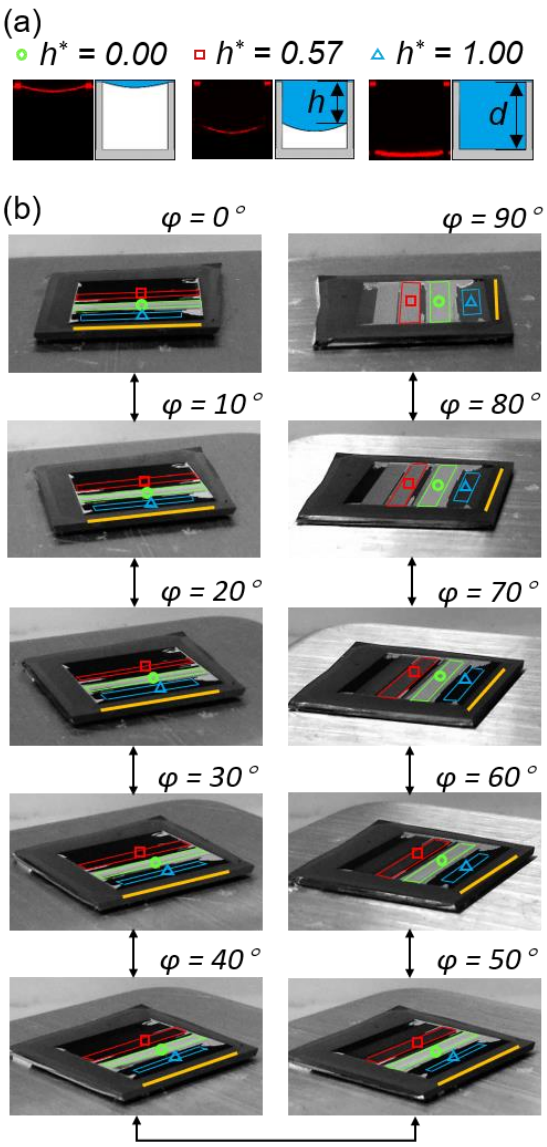

Figure 2-8. An exemplary set of images over the full range of azimuth angles. (a) Cross-trench profiles of the water-air meniscus in a trench obtained with confocal microscopy are paired with schematic interpretations: pinned state, i.e., $h^* = 0.00$ (left); depinned-in state of $h^* = 0.57$ (middle); and fully wetted state, i.e., $h^* = 1.00$ (right). (b) Greyscale images of the immersed SHPo sample at $h^* = 0.57$ taken by a camera of $\beta = 20°$ are listed over varying azimuth $0° \leq \varphi \leq 90°$. The green circles, red squares, and blue triangles identify the regions of $h^* = 0.00$, 0.57, and 1.00, respectively.

The trench directions are indicated by yellow lines. Representing 1 of the 4 intrusion depths tested and recorded by 1 of the 3 cameras used, this set of images is 1 of 12 sets analyzed for this study.

To analyze the collected brightness data, the next step is to establish the brightness range (i.e., μ_{pinned} - $\mu_{fully\ wetted}$) for each viewing direction (β, φ) and convert the brightness values μ to brightness ratios μ^* using Equation (2-2). Figure 2-9 helps explain this process. Figure 2-9(a) collects the brightness values μ obtained from Figure 2-8(b) to reveal the trends of a depinned-in surface (h^* = 0.57) as well as the two reference states (h^* = 0.00 and h^* = 1.00) over the full range of azimuth angle φ at β = 20°. Note that, whatever φ is, the pinned state (h^* = 0.00; green circles) should always appear the brightest (highest μ values), as confirmed in the graph. The fluctuation of its brightness value in the graph is caused mostly by the reflections on the sample rotational stage made of stainless steel – much more than by the none-TIR lights on the sample described in the concept and theorization section. Oppositely, the fully wetted state (h^* = 1.00; blue triangle symbols) should always appear the darkest (lowest μ values) as confirmed in the graph. The unreasonable brightness deviation at small azimuth angles (φ > 75°) is caused by the light reflected from water-silicon interfaces on the trench bottom, as explained as the main deviation from the all-TIR assumption in the concept and theorization section. In contrast, the depinned-in state (h^* = 0.57) appears nearly as bright as the pinned state (h^* = 0.00) at φ = 90°, dims with decreasing φ, and turns nearly as dark as the fully wetted state (h^* = 1.00) at sufficiently small φ. More importantly for our purpose, the calculated values of brightness ratio μ^* are presented in Figure 2-9(b). Since much of the non-TIR reflections, especially those from the surroundings, are shared b all three cases and canceled out in the brightness ratio μ^*, much of the fluctuation and deviation saw in Figure 2-9(a) are filtered out in Figure 2-9(b), explaining the utility of using μ^* instead of μ.

The theoretical brightness ratio μ^* is derived from Equation (2-3) and plotted as solid lines in Figure 2-9(b) for the same condition as the experiment, i.e., $h^* = 0.57$ at $\beta = 20°$. The sloped line indicates that the brightness of a given intrusion ratio would vary depending on the azimuthal angle φ while it is large enough to provide a viewable TIR, i.e., $w_T^* > 0$. However, without viewable TIR the surface would remain equally dark for all smaller φ as represented by the horizontal line of μ^*. To compare the experiments and theory, in Figure 2-9(b), the corresponding azimuth angle for the surface at $\mu^* = 0.5$ is found to be 71.4° theoretically from Equation (2-4) and 75.5° experimentally from data interpolation. The difference of 4.1° between them can be attributed to the uncertainties of φ and β in the apparatus and μ^* in data acquisition.

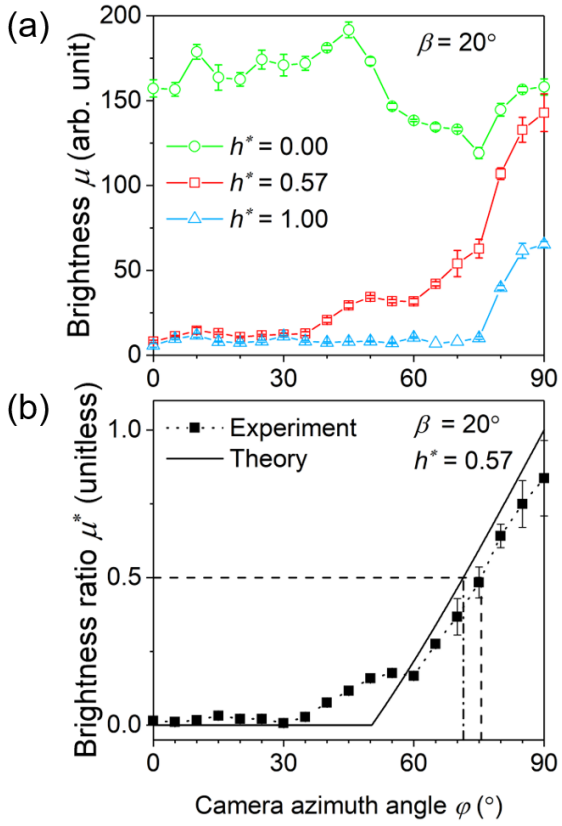

Figure 2-9. An exemplary brightness result obtained for an intermediate (depinned-in) state. Intrusion ratio $h^* = 0.57$ with camera elevation angle $\beta = 20°$. (a) Brightness μ on three states $h^* =$

0.00, 0.57, 1.00 measured from the pictures of Figure 2-8(b). Error bars are statistical error from the standard deviation of brightness data. (b) Brightness ratio μ^* on the depinned-in state of $h^* = 0.57$ relative to the pinned ($h^* = 1.00$) and the fully wetted ($h^* = 0.00$) state. Theoretical predictions (lines) and experimental values (symbols) match despite the reality deviating from the assumptions used for the theory. Dashed and dash-dotted lines relate the experimental and theoretical azimuth angles φ to $\mu^* = 0.5$.

For the experiments, all 4 intrusion depths were created on one sample using the pipetting tricks described in the Section 2.3.3. Using the 3 cameras, which provide 3 different elevation angles at the same time, and the rotational stage, which sets a new azimuth angle quickly, a large number of data points covering a wide range of observation angle sets (β, φ) can be obtained in one test run and processed to draw one row of the three graphs in Figure 2-10. Each graph presents the brightness value μ of the pinned, depinned-in, and fully wetted state on the sample obtained for one of the 4 sequentially obtained intrusion depths. Using the brightness values of the pinned, depinned-in, and fully wetted state, the brightness ratio μ^* of each depinned-in state is shown in Figure 2-11 along with the theoretical values derived from Equation (2-3). In both Figure 2-10 and Figure 2-11, the four rows of graphs, thus, mean four sets of three test runs each with increasing intrusion depth obtained by waiting longer in the undersaturated water.

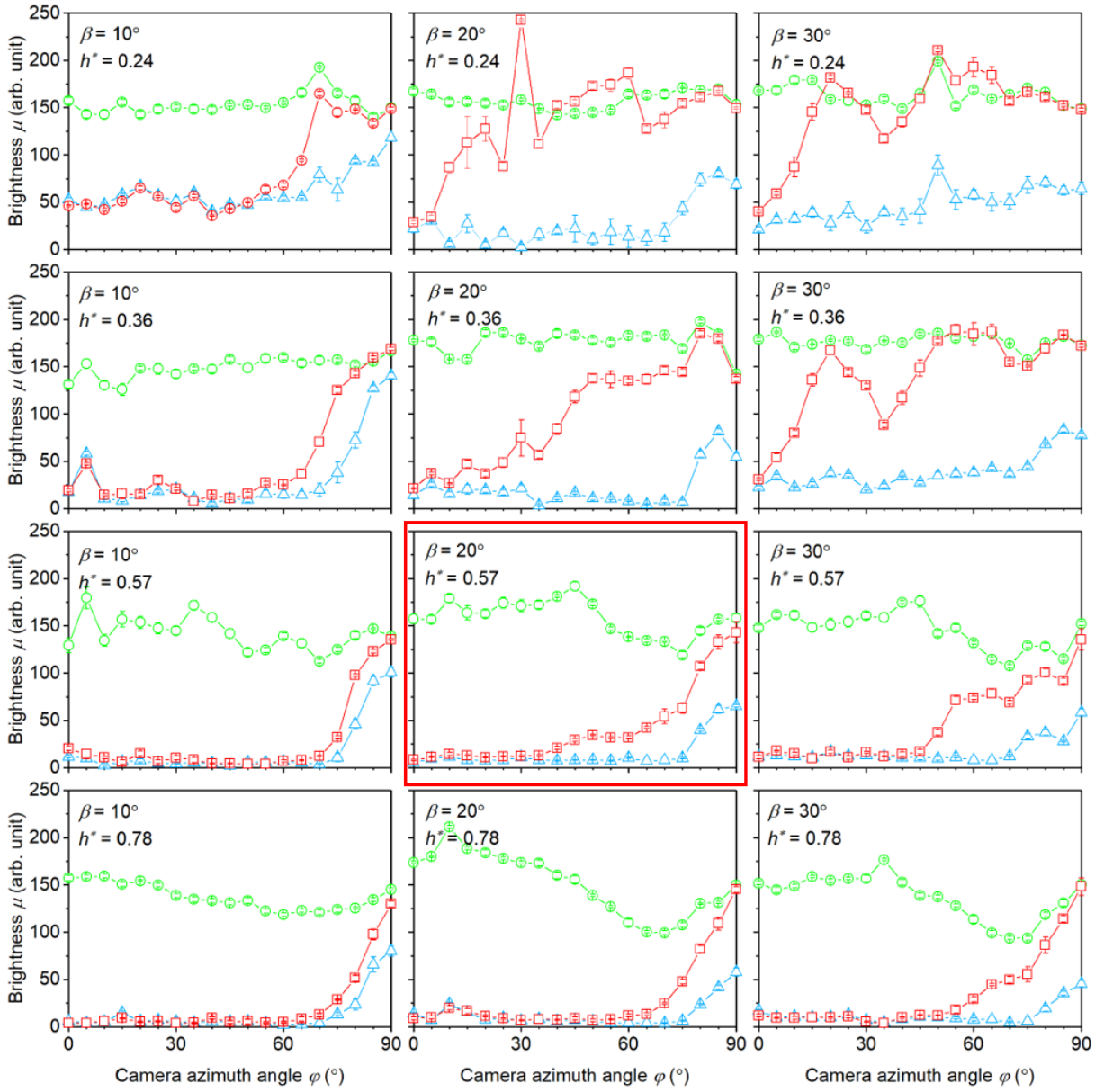

Figure 2-10. Brightness values of pinned, depinned-in, and fully wetted states. Depinned-in states are with 4 different depths (h^* = 0.24, 0.36, 0.57, 0.78), and all states are observed with 3 different elevation angles (β = 10°, 20°, 30°) over a full range of azimuth angles (φ = 0° – 90°). For the symbols and lines in the graphs, the brightness of the pinned, depinned-in, and fully wetted states are shown with green hollow square, red hollow circle, and blue hollow triangle, respectively. The

red-outlined graph is equivalent to Figure 2-9(a). Error bars are statistic error from the standard deviation of brightness data.

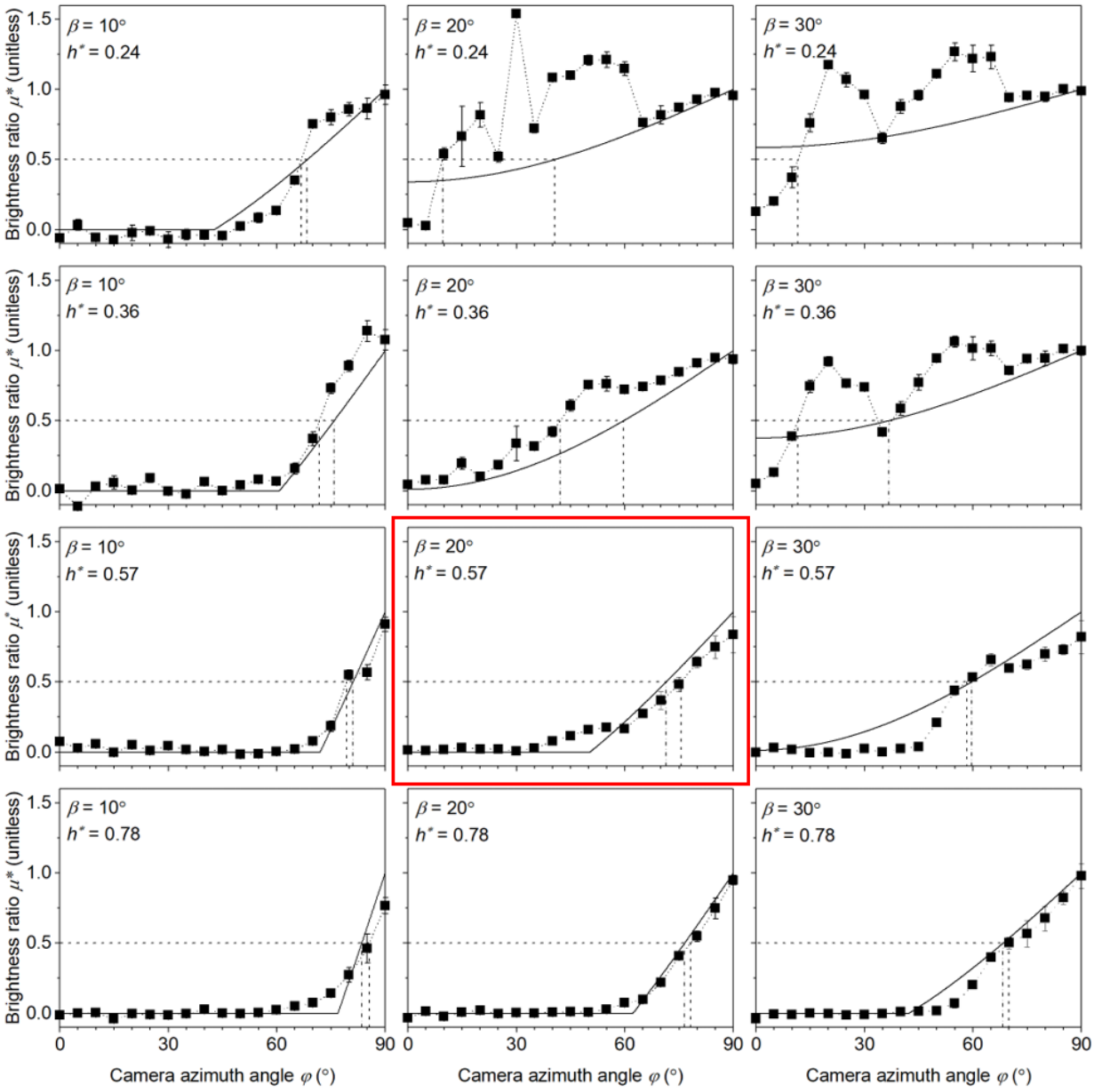

Figure 2-11. The brightness ratios of depinned-in states. Experimental results derived from Figure 2-10 are shown with black solid squares, and theoretical predictions derived from Equation 3 are shown with black lines. Dashed lines and dash-dotted lines are to find experimental φ and

theoretical φ for $\mu^* = 0.5$, respectively. The red-outlined graph is identical to Figure 2-9(b). Error bars are derived from the standard deviation of brightness data at the corresponding states.

2.4.2 Intrusion Depth vs. Observation Angles

By applying the above process to the 12 sets of results as collected in Figure 2-11, the intrusion ratio h^* for 12 combinations of β and φ is summarized in Figure 2-12, where each symbol represents a combination of β, φ, and h^*. Figure 2-12 also includes the theoretical lines from Equation (2-4) for comparison. Each theoretical line represents one intrusion ratio h^* and indicates the observation directions β and φ that would make the brightness ratio $\mu^* = 0.5$. When the surface with a certain h^* is observed with azimuth angle and elevation angle smaller than the corresponding pair, φ and β, the surface will appear darker, i.e., $\mu^* < 0.5$, and become distinguishable from the dewetted surface. In other words, each φ represents the azimuth angle that starts to make the surface half dark (i.e. $\mu^* = 0.5$) for a given elevation angle β. The similar trends of theory and experiments verify how h^* is related to β and φ. Each line shows the ranges of β and φ that can be used to detect the corresponding h^*. For an example, to detect $h^* = 0.24$, one should use $\beta < 26°$; otherwise, Equation (2-3) cannot be solved with $\mu^* = 0.5$ and the surface would always appear brighter than $\mu^* = 0.5$. For another example, to detect $h^* = 0.57$, one should use $\varphi > 39°$; otherwise, Equation (2-3) cannot be solved with $\mu^* = 0.5$ and the surface would always appear darker than $\mu^* = 0.5$. Conversely, each observing direction of β and φ has a certain range of intrusion ratio it can detect. For example, with a large β, only relatively large intrusion ratios are detectable (e.g., $0.35 \leqslant h^* < 1$ with $\beta = 30°$), while a smaller β can detect a wider range of intrusion ratios (e.g., $0.11 \leqslant h^* < 1$ with $\beta = 10°$). Accordingly, to detect h^* over as wide range as possible, β should be as small as possible as far as the imaging capabilities (e.g., image resolution) allow.

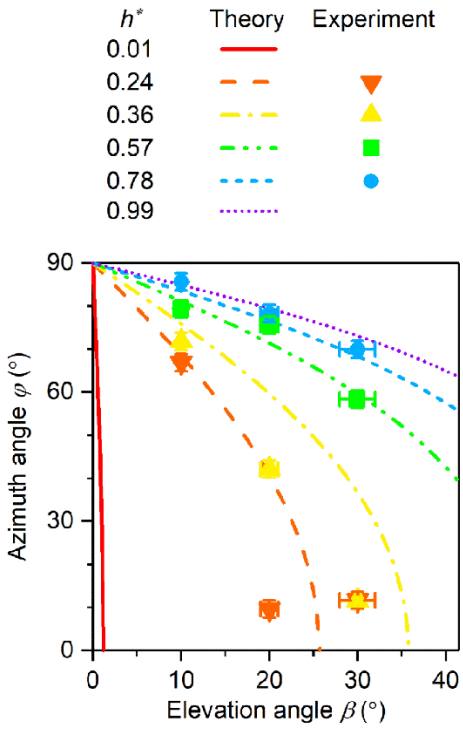

Figure 2-12. The map of intrusion ratio h^* for observation directions. The map uses the nominal brightness ratio $\mu^* = 0.5$. Theoretical predictions (lines) for 6 different values of h^* are derived from Equation 4. Experimental data (symbols) of 4 different values of h^* are from all the graphs in Figure S7. The horizontal axis is limited to $0° < \beta < 41.4°$, where TIR exists. The error bars of β and φ are systematic errors from the range of angles across the sample area.

2.4.3 Analysis of Meniscus Curvature Effect

Obtaining the curvature of the meniscus from the contact angle θ and integrating the brightness over the meniscus in a trench using Equation (2-5), the brightness ratios of the flat and curved meniscus are shown as a function of θ for 6 wetting states ($h^* = 0.00$, 0.01, 0.24, 0.36, 0.57 and 0.78) for 3 elevation angles ($\beta = 10°$, 20°, and 30°) and 2 azimuth angles ($\varphi = 0°$ and 45°) in Figure 2-13. If the overall brightness is lowered by the curvature, one would overestimate the intrusion ratio h^* when using the proposed method (Equation (2-4)), as shown in Figure 2-14. Note some

combinations of h^* and β (e.g., h^* being too large for β) has no solution (i.e., $\mu^* < 0$) and, thus, are irrelevant and not drawn. Figure 2-14 shows that, for a given set of elevation angle β and azimuth angle φ, an overestimation would occur if the contact angle θ (θ_a to be more exact during a wetting process) is larger than a certain value. Since the advancing contact angle θ_a was found to be ~110° from the confocal microscope image in Figure 2-8(a), the overestimation can be mostly ignored in our case. Reviewing Figure 2-14, one can see the meniscus curvature causes no overestimation of intrusion ratio h^* when a relatively small elevation angle (i.e., β = 10°, 20°) is used. Overestimation occurs only if a large elevation angle (β = 30°) is used, and a larger azimuth angle (φ = 45°) prevents the overestimation or lessens the degree of overestimation. So, overall, one can avoid or minimize the curvature effect by avoiding large elevation angles and very small azimuthal angles.

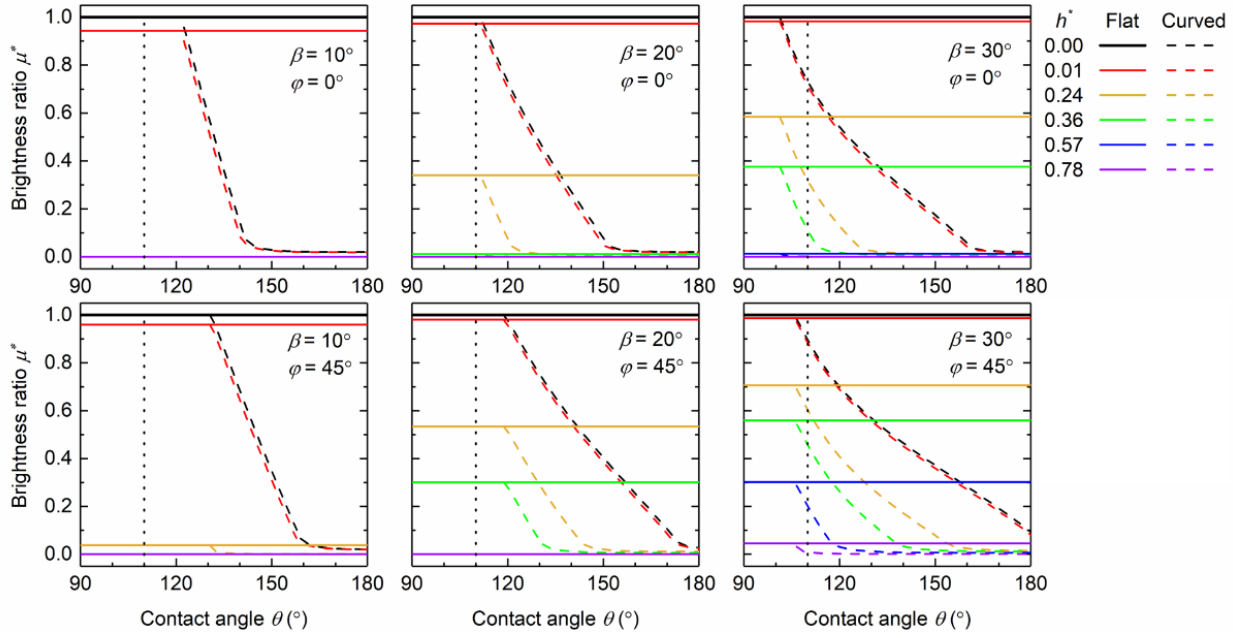

Figure 2-13. The brightness ratio with flat and curved meniscus as a function of water contact angle. Results of three elevation angles (β = 10°, 20°, 30) and two azimuth angles (φ = 0°, 45°) are

shown. The dotted vertical lines represent the contact angle found for the current experiments, θ =110°.

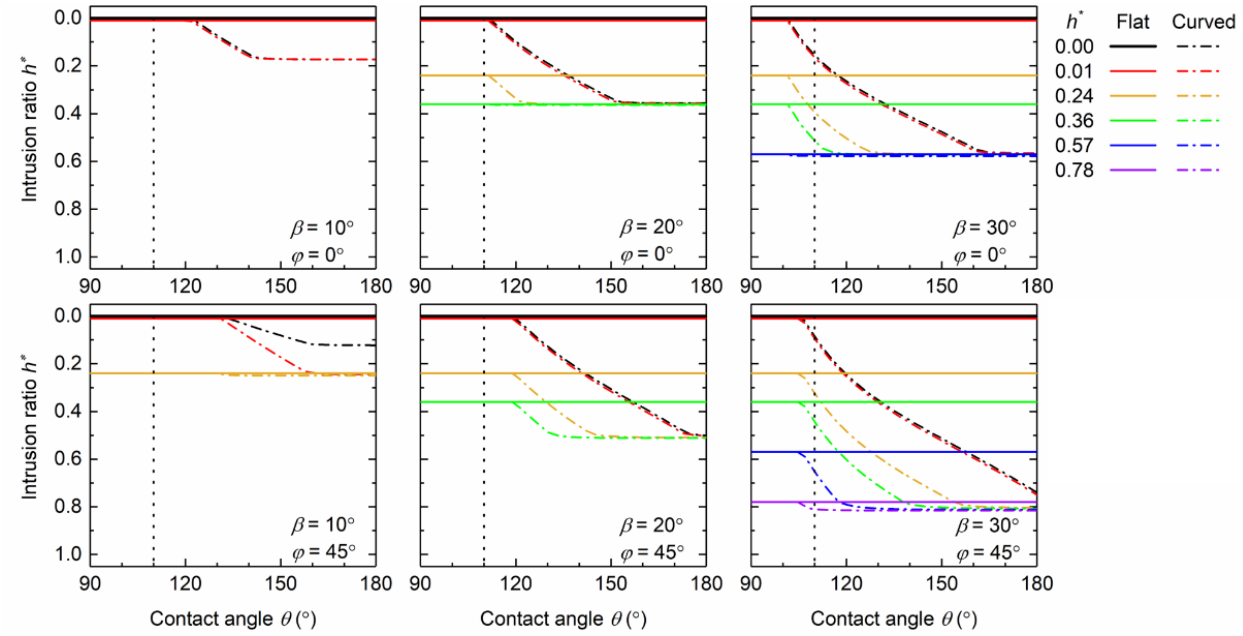

Figure 2-14. The intrusion ratio with flat and curved meniscus as a function of water contact angle. Results of three elevation angles (β = 10°, 20°, 30) and two azimuth angles (φ = 0°, 45°) are shown. The combinations of h^*, β, and φ that result in μ^* = 0 (i.e., no solution) are irrelevant and not drawn. The dotted vertical lines represent the contact angle found for the current experiments, θ =110°.

2.4.4 Discerning the Pinned vs. Intermediate State.

The most prominent application example of this report is to empower one to discern intermediate (i.e., depinned-in) states from the dewetted state on microtrench SHPo surface by simply looking at the surface under water in real-time with naked eyes – extremely useful during field experiments. Based on the underlying theory and testing experience, we will first explain the identification principle and then present step-by-step instructions for the identification. Since differentiation of a depinned-in state from the pinned state becomes more precise as the minimum detectable

intrusion depth becomes smaller, the ideal viewing direction is $\varphi = 0°$ and $\beta \sim 0$, which provides the smallest minimum detectable intrusion; in Figure 2-12, for example, at $\varphi = 0°$ and $\beta = 0.6°$ the minimum detectable intrusion ratio is very small: $h^* = 0.01$. In this condition, any depinned-in state with an intrusion ratio larger than the minimum detectable value will appear half dark, which can be easily differentiated from the pinned state (i.e., shiny with $\mu^* = 1$). For $\beta \sim 0$, one should choose the smallest but still functional value in practice. The minimum intrusion depth detectable, according to Equation (2-4), is $h^* \sim 0.009$ for $\beta = 1°$ and $h^* \sim 0.044$ for $\beta = 5°$, assuming $d = w$. To give a sense of reality, they correspond to $h \sim 0.9$ and 4.4 μm for the trench depth $d = 100$ μm. If larger φ or β is used, the minimum detectable intrusion would be larger. The smallest functional β, which is determined by the trench width and the optical resolution determined by the optical tools, e.g., camera and lighting, was found to be ~5° in most practices including the current study. While the nominal value $\mu^* = 0.5$ is used to represent the region of $0 < \mu^* < 1$ when finding h^* from Equation (2-3) in Figure 2-12, for naked eyes, it is more practical to use $\mu^* = 0$ instead, i.e., determine when the surface appears as dark as a fully wetted state rather than half dark.

The above identification procedure can be implemented with the following step-by-step instructions : (1) Before actual tests, create a pinned site and a fully wetted site within the area of interest on the SHPo surface, and get oneself familiar with the appearances of the two reference states with azimuth angle $\varphi = 0°$ and elevation angle $\beta = 5°$ (i.e., a value very close to 0° and still practical) under the lighting condition of actual tests. (2) Restore the surface to its natural wetting state and start an actual test. Look at the area of interest with the same observing angles, i.e., $\varphi = 0°$, and $\beta = 5°$. (3) The regions that appear as bright as the pinned site are in a pinned state. The regions that appear as dark as the fully wetted site are not pinned; they are either depinned-in or fully wetted. For uncertainties, variation of azimuth angle caused by unsteady human observation,

e.g. ±5°, would not affect the uncertainties of the observation result much. For $\beta = 5°$, the minimum detectable intrusion depth at $\varphi = 5°$ is only 0.3% larger than that at $\varphi = 0°$. However, variation of elevation angle would affect the uncertainties of the observation significantly. For $\varphi = 0°$, the minimum detectable intrusion depth at $\beta \sim 10°$ is twice the depth at $\beta \sim 5°$. By teaching the user to observe the surface with $\varphi = 0°$ and $\beta \sim 0$ with special care to maintain the elevation angle constant, this method allows one to see which regions are properly dewetted (pinned) and which regions are not (i.e., depinned-in by more than the minimum intrusion depth observable), preventing the common misinterpretation of slightly depinned states as a pinned state.

Different procedures can be developed for different goals, using the principle and strategy presented in this chapter. As a relatively simple example, one can discern intermediate (i.e., depinned-in) states from the fully wetted state by developing a procedure that is opposite but analogous to the above. Using $\varphi = 90°$ and any $\beta < 41.4°$, where the meniscus inside the trench is fully visible to the viewer, a surface that appears similarly dark as the fully wetted is in the fully wetted state, and a surface that appears distinctively brighter is in either the pinned or a depinned-in state. Combining this method of discerning depinned-in states from the fully wetted state and the preceding method of discerning depinned-in states from the pinned state, one can now determine whether a surface is dewetted, fully wetted, or in an intermediate state between them.

As shown in the preceding section, it is possible to estimate the degree of wetting (i.e., intrusion depth) quantitatively through a more elaborated process, i.e., not by just looking. Unlike the simple discerning of depinned-in states from the pinned or fully wetted state, quantitative estimation of the intrusion depth requires the user to take a series of pictures and measure their brightness electronically as performed in the preceding section.

2.5 Conclusions

We have proposed and confirmed a theoretical model to predict the brightness of the microtrench SHPo surface under different wetting states by visual observation. The model explained the brightness change on the SHPo surface with the TIR region visible to viewers and how the visible region is affected by the intrusion depth of water and the observation direction defined as elevation angle β and azimuth angle φ. Usual microtrench SHPo surface samples have been fabricated for experiments. After confirming the properly dewetted (i.e., pinned) state appears bright and the fully wetted state appears dark for any observing direction, we verified the model with experiments utilizing confocal microscopy to read the intrusion depths and three underwater cameras to represent visual observations. By quantifying the brightness of the surface as a function of intrusion depth and observation angles, we provided a strategy to detect the intermediate wetting (depinned-in) state as well, not just the usual but crude information of wetting or dewetting.

References

1. N. Yu and C.-J. Kim. *Detecting the sub-states of grating superhydrophobic surfaces with naked eyes*. in *2018 IEEE Micro Electro Mechanical Systems (MEMS)*. 2018. IEEE.

2. N. Yu, S. Kiani, M. Xu, and C.-J. Kim, "Brightness of Microtrench Superhydrophobic Surfaces and Visual Detection of Intermediate Wetting States", *Langmuir*, 37, 1206-1214, 2021.

3. M. Xu, G. Sun, and C.-J. Kim, "Infinite lifetime of underwater superhydrophobic states", *Physical Review Letters*, 113, 136103, 2014.

4. C. Lee, C.-H. Choi, and C.-J. Kim, "Superhydrophobic drag reduction in laminar flows: a critical review", *Experiments in Fluids*, 57, 1-20, 2016.

5. C. Lee and C.-H. Choi, "Structured surfaces for a giant liquid slip", *Physical Review Letters*, 101, 064501, 2008.

6. M. Xu, A. Grabowski, N. Yu, G. Kerezyte, J.-W. Lee, B.R. Pfeifer, and C.-J. Kim, "Superhydrophobic drag reduction for turbulent flows in open water", *Physical Review Applied*, 13, 034056, 2020.

7. K.B. Golovin, J.W. Gose, M. Perlin, S.L. Ceccio, and A. Tuteja, "Bioinspired surfaces for turbulent drag reduction", *Philosophical Transactions of the Royal Society A: Mathematical, Physical and Engineering Sciences*, 374, 20160189, 2016.

8. G.D. Bixler and B. Bhushan, "Rice and butterfly wing effect inspired low drag and antifouling surfaces: a review", *Critical Reviews in Solid State and Materials Sciences*, 40, 1-37, 2015.

9. M. Ferrari and F. Cirisano, "Hydrophobicity and superhydrophobicity in fouling prevention in sea environment", *Advances in Contact Angle, Wettablility and Adhesion; Mittal, KL, Ed*, 241-265, 2018.

10. F. Brocher, "Reserches sur la respiration des insects aquatiques adultes–les haemonia.", *Ann Biol Lac*, 5, 5-26, 1912.

11. A. Cassie and S. Baxter, "Wettability of porous surfaces", *Transactions of the Faraday society*, 40, 546-551, 1944.

12. T.L. Liu, Z. Chen, and C.-J. Kim, "A dynamic Cassie–Baxter model", *Soft Matter*, 11, 1589-1596, 2015.

13. R.N. Wenzel, "Resistance of solid surfaces to wetting by water", *Industrial & Engineering Chemistry*, 28, 988-994, 1936.

14. D.G. Crowdy, "Analytical formulae for longitudinal slip lengths over unidirectional superhydrophobic surfaces with curved menisci", *Journal of Fluid Mechanics*, 791, 2016.

15. T. Biben and L. Joly, "Wetting on nanorough surfaces", *Physical review letters*, 100, 186103, 2008.

16. C.J. Teo and B.C. Khoo, "Flow past superhydrophobic surfaces containing longitudinal grooves: effects of interface curvature", *Microfluidics and Nanofluidics*, 9, 499-511, 2010.

17. H. Park, C.-H. Choi, and C.-J. Kim, "Superhydrophobic drag reduction in turbulent flows: a critical review", *Experiments in Fluids*, 62, 1-29, 2021.

18. M.S. Bobji, S.V. Kumar, A. Asthana, and R.N. Govardhan, "Underwater sustainability of the "Cassie" state of wetting", *Langmuir*, 25, 12120-12126, 2009.

19. R. Poetes, K. Holtzmann, K. Franze, and U. Steiner, "Metastable underwater superhydrophobicity", *Physical Review Letters*, 105, 166104, 2010.

20. M.A. Samaha, H.V. Tafreshi, and M. Gad-el-Hak, "Influence of flow on longevity of superhydrophobic coatings", *Langmuir*, 28, 9759-9766, 2012.

21. B.J. Lee, Z. Zhang, S. Baek, S. Kim, D. Kim, and K. Yong, "Bio-inspired dewetted surfaces based on SiC/Si interlocked structures for enhanced-underwater stability and regenerative-drag reduction capability", *Scientific reports*, 6, 1-11, 2016.

22. B.V. Hokmabad and S. Ghaemi, "Effect of flow and particle-plastron collision on the longevity of superhydrophobicity", *Scientific reports*, 7, 1-10, 2017.

23. H. Rathgen and F. Mugele, "Microscopic shape and contact angle measurement at a superhydrophobic surface", *Faraday discussions*, 146, 49-56, 2010.

24. S. Li, S. Lamant, J. Carlier, M. Toubal, P. Campistron, X. Xu, G. Vereecke, V. Senez, V. Thomy, and B. Nongaillard, "High-frequency acoustic for nanostructure wetting characterization", *Langmuir*, 30, 7601-7608, 2014.

25. P. Wang, J. Su, M. Shen, M. Ruths, and H. Sun, "Detection of liquid penetration of a micropillar surface using the quartz crystal microbalance", *Langmuir*, 33, 638-644, 2017.

26. A. Checco, B.M. Ocko, A. Rahman, C.T. Black, M. Tasinkevych, A. Giacomello, and S. Dietrich, "Collapse and reversibility of the superhydrophobic state on nanotextured surfaces", *Physical Review Letters*, 112, 216101, 2014.

27. D. Reholon and S. Ghaemi, "Plastron morphology and drag of a superhydrophobic surface in turbulent regime", *Physical Review Fluids*, 3, 104003, 2018.

28. K.T. Flynn Bolte, R.P. Balaraman, K. Jiao, M. Tustison, K.S. Kirkwood, C. Zhou, and P. Kohli, "Probing liquid–solid and vapor–liquid–solid interfaces of hierarchical surfaces using high-resolution microscopy", *Langmuir*, 34, 3720-3730, 2018.

29. P. Papadopoulos, L. Mammen, X. Deng, D. Vollmer, and H.-J. Butt, "How superhydrophobicity breaks down", *Proceedings of the National Academy of Sciences*, 110, 3254-3258, 2013.

30. P. Lv, Y. Xue, Y. Shi, H. Lin, and H. Duan, "Metastable states and wetting transition of submerged superhydrophobic structures", *Physical Review Letters*, 112, 196101, 2014.

31. P. Lv, Y. Xue, H. Liu, Y. Shi, P. Xi, H. Lin, and H. Duan, "Symmetric and asymmetric meniscus collapse in wetting transition on submerged structured surfaces", *Langmuir*, 31, 1248-1254, 2015.

32. Y. Xiang, Y. Xue, P. Lv, D. Li, and H. Duan, "Influence of fluid flow on the stability and wetting transition of submerged superhydrophobic surfaces", *Soft Matter*, 12, 4241-4246, 2016.

33. M. Moosmann, T. Schimmel, W. Barthlott, and M. Mail, "Air–water interface of submerged superhydrophobic surfaces imaged by atomic force microscopy", *Beilstein journal of nanotechnology*, 8, 1671-1679, 2017.

34. U.U. Ghosh, S. Nair, A. Das, R. Mukherjee, and S. DasGupta, "Replicating and resolving wetting and adhesion characteristics of a rose petal", *Colloids and Surfaces A: Physicochemical and Engineering Aspects*, 561, 9-17, 2019.

35. A. Elbourne, M.F. Dupont, S. Collett, V.K. Truong, X. Xu, N. Vrancken, V. Baulin, E.P. Ivanova, and R.J. Crawford, "Imaging the air-water interface: Characterising biomimetic and natural hydrophobic surfaces using in situ atomic force microscopy", *Journal of colloid and interface science*, 536, 363-371, 2019.

36. A.T. Paxson and K.K. Varanasi, "Self-similarity of contact line depinning from textured surfaces", *Nature communications*, 4, 1-8, 2013.

37. S. Yang, J. Du, M. Cao, X. Yao, J. Ju, X. Jin, B. Su, K. Liu, and L. Jiang, "Direct Insight into the Three-Dimensional Internal Morphology of Solid–Liquid–Vapor Interfaces at Microscale", *Angewandte Chemie International Edition*, 54, 4792-4795, 2015.

38. S.J. Lm, D. Kim, Y. Kim, S. Jeong, C. Pang, S. Ryu, and B.M. Weon, "Hydrophobicity evolution on rough surfaces", *Langmuir*, 36, 689-696, 2020.

39. Y. Ichikawa, K. Yamamoto, M. Yamamoto, and M. Motosuke, "Near-hydrophobic-surface flow measurement by micro-3D PTV for evaluation of drag reduction", *Physics of Fluids*, 29, 092005, 2017.

40. K. Rykaczewski, T. Landin, M.L. Walker, J.H.J. Scott, and K.K. Varanasi, "Direct imaging of complex nano-to microscale interfaces involving solid, liquid, and gas phases", *ACS nano*, 6, 9326-9334, 2012.

41. S. Wiedemann, A. Plettl, P. Walther, and P. Ziemann, "Freeze fracture approach to directly visualize wetting transitions on nanopatterned superhydrophobic silicon surfaces: More than a proof of principle", *Langmuir*, 29, 913-919, 2013.

42. E. Aljallis, M.A. Sarshar, R. Datla, V. Sikka, A. Jones, and C.-H. Choi, "Experimental study of skin friction drag reduction on superhydrophobic flat plates in high Reynolds number boundary layer flow", *Physics of Fluids*, 25, 025103, 2013.

43. M. Xu, N. Yu, J. Kim, and C.-J. Kim, "Superhydrophobic drag reduction in high-speed towing tank", *Journal of Fluid Mechanics*, 908, A6, 2021.

44. H. Park, G. Sun, and C.-J. Kim, "Superhydrophobic turbulent drag reduction as a function of surface grating parameters", *Journal of Fluid Mechanics*, 747, 722-734, 2014.

45. M. Born and E. Wolf, *Principles of optics: electromagnetic theory of propagation, interference and diffraction of light*. 2013: Elsevier.

Chapter 3 The State of Plastron on Micro-trench Superhydrophobic Surfaces in High-speed Flows of Open Water

3.1 Introduction

Superhydrophobic (SHPo) surfaces have been one of the most popular topics in science and engineering over the last two decades because of their unique potentials, such as hydrodynamic drag reduction [1, 2], self-cleaning [3], anti-icing [4], anti-biofouling [5], and anti-corrosion [6]. Among them, drag reduction of watercraft has been cited as a motivating factor in nearly every publication on SHPo surfaces for its global-scale impact on energy saving and environmental protection [7]. When a SHPo surface is completely immersed in water, a substantially continuous layer of air, commonly called a plastron [8], may be formed on it and produce a slip boundary that reduces skin friction drag. While all numerical studies over the years [9-14] and many experimental studies in the 2010s [15-18] have reported a significant drag reduction, successful drag reduction in fully turbulent flows in open water, which represents the field condition of watercraft, has not been reported until 2020 [19, 20]. These most recent successes have eased the skepticism that had grown against the SHPo drag reduction, after two decades of research without any successful field experiments. Importantly, those works [19, 20] strongly suggested that most of the inconsistent experimental results in the past have been simply due to the loss or deterioration of the plastron. In other words, the original notion of SHPo drag reduction is valid as far as the plastron remains in a good shape. The tortuous path to the current state of knowledge also indicates how difficult, yet important it is to accurately monitor the state of the plastron during experimental

studies of SHPo drag reduction, leading to the two-camera observation technique by Yu [21]. Focusing on longitudinal micro-trench SHPo surfaces, which have been the most effective for drag reduction [7], and to help the design of SHPo surfaces capable of reducing the drag for watercraft, this chapter aims to understand the range of trench geometries on which the plastron maintains a state that is acceptable for drag reduction in high-speed open-water flows.

Over the years, hydrostatic pressure and air diffusion have been found to affect the plastron stability in stationary [22-26] and flowing [27, 28] water. More recently, the shear-driven drainage [29, 30], which was developed to understand the loss of infused oil on liquid infused surfaces (LIS) [31] caused by the shear of flowing water, has been borrowed to explain the plastron loss on trench SHPo surface in very high shear flows [20]. However, while the diffusional loss of the infused oil on LIS in water is negligible and was justifiably ignored in the shear drainage model, the diffusional loss of the trapped air in water is significant and would require a revised theory applicable to SHPo surfaces. To establish a unified model that can describe the plastron morphology on the longitudinal micro-trench SHPo surfaces in high-speed flows under water, in this chapter we combine (i) the plastron stability theory based on the hydrostatic pressure and air diffusion with (ii) the shear-drainage theory modified for plastron (i.e., not oil) stability. In addition, the water pressure on the plastron is expected to deviate from the theory at the front and rear end of the trench by the dynamic effect of flows, leading to a negative effect when compounded with the interfacial contaminations such as surfactants [32].

To evaluate the unified model experimentally, we prepare a combinatorial series of SHPo surfaces and monitor their plastron status in fully turbulent flows under a motorboat at various flow speeds on seawater. For drag reduction applications, one would like to have a full plastron, where the trapped air fills the entire depth and length of the trench. To enable differentiating full or nearly-

full plastron, which can provide an acceptable amount of drag reduction (e.g., > 30% of the reduction by full plastron), from degraded or no plastron, which provides unacceptably small drag reduction (e.g., < 30% of the reduction by full plastron), we devise a new observation scheme using two underwater cameras by applying the approach of Yu [21] to the current goal. Since the plastron was observed intact at all speeds (i.e., 2.3 m/s < flow seed < 5.1 m/s or 10000 s^{-1} < shear rate < 62000 s^{-1}) in the previous boat experiments [19] but found depleted at the higher speeds (i.e., 6.1 m/s < flow speed < 10.1 m/s, or 55000 s^{-1} < shear rate < 140000 s^{-1}) in the towing tank experiments while using similar trench SHPo surfaces [20], we modify the boat used in this paper to increase its top speed to 7.2 m/s (or shear rate up to ~83000 s^{-1}) so that the plastron can be depleted by shear-driven drainage in the current boat study.

3.2 Theory and Model

3.2.1 Acceptable and Unacceptable Plastron for Drag Reduction

Let us consider a micro-trench SHPo surface immersed in water, as illustrated in Figure 3-1, which also defines the pitch *p*, width *w*, and depth *d* of the trenches. The gas fraction of the surface is defined as *w/p*. Although most numerical studies of SHPo drag reduction assume air-water interfaces (or menisci) to be flat and pinned on the trench top edges, in reality, menisci are rarely flat and may not be pinned on the top. For watercraft applications, which usually involve open water in nature (whose air saturation level hovers around 100%) and hydrostatic pressure, menisci would either be pinned and concave, as shown in Figure 3-1(a-1), or depinned-in and concave, as shown in Figure 3-1(a-2). Note that the amount of depinning is expressed as the water intrusion depth *h*, which is the distance between the trench top and contact line. Compared with the pinned-and-flat meniscus, the pinned-and-concave meniscus would degrade the slip only slightly, but the

depinned-in meniscus (even if flat) would degrade the slip significantly, as summarized in Lee [33]. Both numerical [34] and analytical [35] studies have predicted that the slip length, which determines the drag-reducing ability of a SHPo surface, on longitudinal trenches would decrease by ~50% when the contact line slides down from the trench top by merely 10% of the trench width, i.e., h/w = 0.1, and by ~70% when h/w = 0.2. Such a small amount of depinning has been unnoticeable in high-speed flow experiments, where the only practical way to confirm the plastron was by observing its silvery sheen, which indicates its existence but not thickness. Note even a significantly depinned plastron, e.g., Figure 3-1(a-2), may still appear bright, as demonstrated by Yu [21]. Compounded by the fact that even a marginal depinning would lead to substantial degradation of drag reduction, the common practice of confirming the existence of plastron with its brightness helps explain the frustratingly inconsistent experimental results that have been hampering the progress of SHPo drag reduction research. Considering the stringent condition that little depinning is allowable for a successful drag reduction, let us define an acceptable plastron as one with contact lines pinned or slightly depinned on the trench top (e.g., $h/w < 0.1$, or $h/w < 0.2$). Note this new definition of acceptable plastrons, while needed for drag reduction, is a near opposite of the common definition, which acknowledges the plastron until the surface structure is fully or nearly-fully wetted [26]. Assuming the loss of drag reduction by up to 70% is acceptable (somewhat arbitrarily), in this study, we devise and implement a new observation scheme to differentiate the acceptable plastron ($h/w < 0.2$) from the unacceptable plastron ($h/w > 0.2$), as explained in the section for experiments.

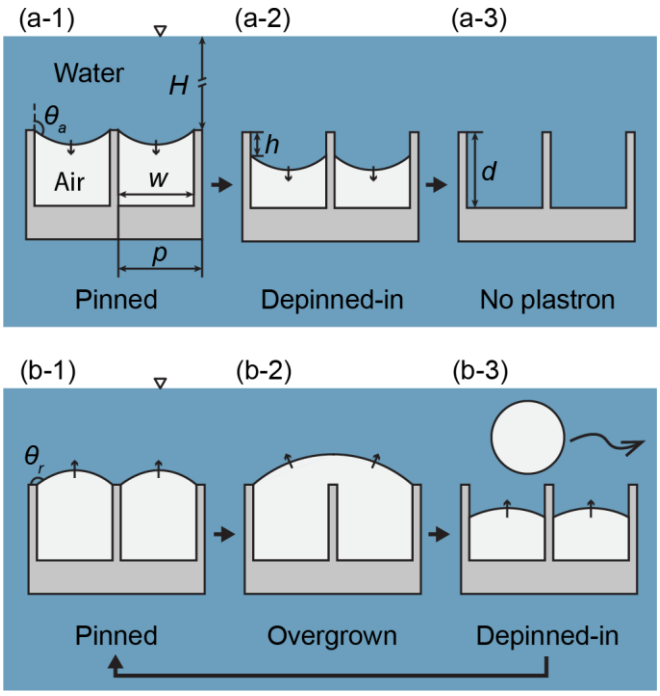

Figure 3-1. Schematic illustration of plastron being compromised on a SHPo surface made of micro-trenches with vertical sidewalls. (a) Since the water pressure is usually higher than the trapped air pressure, the air-water interface is concave when pinned (a-1). If the water pressure is large enough to make the contact angle of water on the trench sidewall exceed the advancing contact angle θ_a, the contact line is depinned from the top edges and slides into the trench (a-2) until the trench is fully wetted (a-3). (b) Although not common, if the water pressure is lower than the trapped air pressure, the meniscus is convex when pinned (b-1). If the contact angle of water on the trench top decreases below the receding contact angle θ_r, the contact line is depinned from the top edges and lets the neighboring air pockets merge (b-2). The merged air may form isolated bubbles off the surface, shrinking the plastron (b-3), which grows back to the pinned state (b-1).

For the contact line to stay pinned as in Figure 3-1(a-1) and (b-1), the pressure difference between the water above and the air inside the plastron, i.e., $\Delta P = P_{water} - P_{air}$, should be balanced by the Laplace pressure of the air-water interface ΔP_σ at the trench top, i.e., $\Delta P = \Delta P_\sigma$. Since the trench

geometry determines the minimum and maximum value of ΔP_σ possible at the trench top, the range of pressure difference allowable for pinning can be expressed as:

$$-\frac{2\sigma\cos\left(\theta_r-90^\circ\right)}{w}=\Delta P_{\sigma,\min}<\Delta P=\Delta P_\sigma<\Delta P_{\sigma,\max}=-\frac{2\sigma\cos\theta_a}{w} \tag{3-1}$$

where σ is the surface tension of water. If the water pressure is higher than the plastron pressure by more than the maximum Laplace pressure, i.e., $\Delta P > \Delta P_{\sigma,max} = -2\sigma\cos\theta_a/w$, the contact line will be depinned in and slide into the trench, as illustrated in Figure 3-1(a-2). Note that the above ranges of Laplace pressure were based on the simple trench geometry with vertical sidewalls. If one adds re-entrant edges to the top of micro-trenches, the maximum Laplace pressure can be as large as $\Delta P_{\sigma,max} = 2\sigma/w$, making the pinned state more robust, as introduced in the previous open-water drag reduction experiments [19]. On the other hand, if the water pressure is lower than the plastron pressure by more than the minimum Laplace pressure, i.e., $\Delta P < \Delta P_{\sigma,min} = -2\sigma\cos(\theta_r - 90°)/w$, the contact lines will be depinned out and let neighboring air pockets merge, as illustrated in Figure 3-1(b-2). The latter case, i.e., Figure 3-1(b), may occur when a SHPo surface is placed shallow in supersaturated water. While the merged air pockets may grow large and leave buoyancy in static water as shown in Figure 3-1(b-3), in fast-flowing water, the overgrown plastron is mostly prevented by the shear.

3.2.2 The Effect of Water Pressure and Air Diffusion on Plastron Morphology

Diffusion of air between the plastron and surrounding water on a hydrophobic trench in stationary water has been well studied using a 2D model and experimentally verified [26]. Based on Henry's law, the partial pressure of dissolved air in water is $p = k_H c$, where k_H is Henry's constant and c is the concentration of dissolved air. The partial pressure of dissolved air in water can also be

expressed as $p = sP_{atm}$, where s is the pressure ratio of the dissolved air in the water to the atmospheric air above the water or the percentage saturation of air in water [36], also simply called the air saturation level. The volumetric diffusion rate of air into the plastron can be approximated by Fick's law as

$$\frac{dV(t)}{dt} = \int k_p \left[sP_{atm} - P_{air}(x,t) \right] dA(x,t) \tag{3-2}$$

where V is the volume of air in the plastron, k_p is the mass transfer coefficient of air across the air-water interface, P_{air} is the air pressure in the plastron, A is the air-water interfacial area, x is the position along the trench, and t is time. In static water, where the condition is uniform along the trench so that $P_{air}(x,t) = P_{air}(t)$ and $A(x,t) = A(t)$, the above diffusion rate can be simplified as

$$\frac{dV(t)}{dt} = k_p A(t) \left[sP_{atm} - P_{air}(t) \right] \tag{3-3}$$

If at a steady-state as well as in static water, so that $dV/dt = 0$, the air pressure in the plastron equals the partial pressure of dissolved air in the surrounding water.

$$P_{air} = sP_{atm} \tag{3-4}$$

Since water pressure on the plastron is $P_{water} = P_H + P_{atm}$, where P_H is the hydrostatic pressure at immersion depth H, Equation (3-4) allows the pressure difference between the two sides of the meniscus to be expressed in the following ways:

$$\Delta P_{st} = P_{water} - P_{air} = P_{water} - sP_{atm} = P_H + (1-s) P_{atm} \tag{3-5}$$

where the subscript *st* indicates static water as opposed to the dynamic water below, which flows and imposes shear stress on the plastron.

3.2.3 The Effect of Shear by Water Flow on Plastron Morphology

SHPo surface vs. LIS: If water is not static, the flowing water will drag the trapped air with it, causing a shear-driven flow of air inside the plastron, hence increasing the air pressure toward the rear (trailing) end of the trench. The increased air pressure at the rear end, in turn, will cause a pressure-driven flow of air in the opposite direction to the water flow. In accordance with the pressure distribution, the plastron morphology can be depicted as shown in Figure 3-2(a), which is drawn for a simple trench with length L, width w, and depth d and assuming $L \gg w$. While the work of Wexler [29] and Liu [30] was developed to understand the loss of oil on LIS, our analysis of the loss of air on SHPo surfaces identifies a new type of internal airflow caused by air diffusion across the air-water interface, as will be elaborated in this section. By combining the three types of air flows (i.e., shear-driven, Laplace pressure-driven, and air diffusion-driven), as indicated in Figure 3-2(b), we will obtain the air pressure in the plastron along the trench and the resulting meniscus morphology.

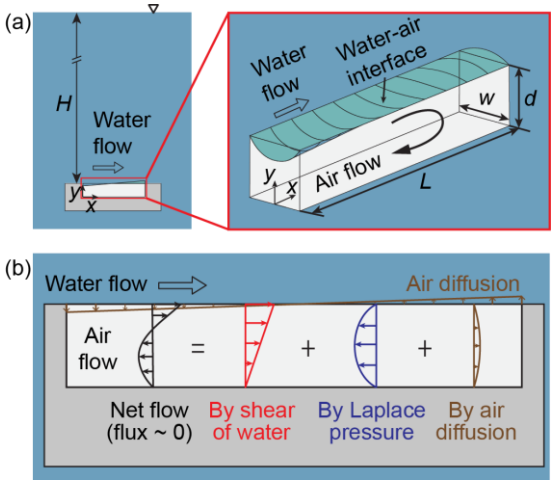

Figure 3-2. A hydrophobic micro-trench submerged in flowing water with the contact lines pinned on top. (a) An exemplary illustration of plastron morphology. The arrow in the trench shows the

air circulation inside the plastron. (b) Profiles of the *x*-direction air flow inside the plastron. The net air flow profile consists of three different flow profiles: shear-driven, Laplace pressure-driven, and air diffusion-driven. The first two profiles follow Wexler [29] developed for LIS, and the third profile is newly introduced to account for the air diffusion across the air-water interface, which varies along the *x*-direction. The net air flux (in the *x*-direction), which is induced by the air diffusion varying along *x*, turns out to be small.

Water shear-driven flux: To analyze the air flux driven by the flowing water, we assume: (i) the air flow inside the plastron is laminar, and (ii) the meniscus is flat. Based on Liu [30], shear-driven flux q_s can be expressed as

$$q_s = \frac{2D}{1+2DN}\frac{c_{sl}\tau w^3}{\mu_{air}} \tag{3-6}$$

where D is the normalized maximum local slip length on the plastron [37] that is determined by trench aspect ratio d/w and gas fraction w/p. For an example, if $d/w = 1$ and $w/p = 0.9$, which are the typical parameters used for the experiments in this study, then $D = 0.201$. N is the viscosity ratio, which is $N = \mu_{water}/\mu_{air} = 55$ for SHPo surfaces, where μ_{water} and μ_{air} are dynamic viscosities of water and air, respectively. c_{sl} is a factor determined by d/w; if $d/w = 1$, $c_{sl} = 0.108$. τ is the shear stress of flowing water applied on the SHPo surface.

Laplace pressure-driven flux: In addition to the above assumptions, for simplicity, we further assume: (iii) the air pressure in the plastron changes linearly with *x*. Following Liu [30], the Laplace pressure-driven flux inside the trench is

$$q_p = -\frac{c_p w d^3}{\mu_{air}}\frac{dP_{air}(x)}{dx} \tag{3-7}$$

where c_p is a factor determined by trench aspect ratio; for $d/w = 1$, $c_p = 0.0351$.

Air diffusion-driven flux: When analyzing the shear-driven flux for LIS, the infused oil was considered to not diffuse into the surrounding water [29]. While such an assumption was reasonable due to the insolubility of silicone oil in water, the same assumption is not reasonable for SHPo surfaces, for which the solubility of air in water is appreciable, e.g., ~0.8 mM [38], compelling us to analyze how the air diffusion between the plastron and flowing water would affect the plastron morphology. Note the diffusion rate across the meniscus varies along the trench because the pressure of trapped air varies along the trench, as indicated with "air diffusion" in Figure 3-2(b). At a steady-state, for example, air would diffuse into the plastron on the leading half of the trench and diffuse out from the plastron on the trailing half of the trench, inducing a new air flux q_d that we call air diffusion-driven flux, as shown with "by air diffusion" in Figure 3-2(d). The varying air pressure along the trench would also change the meniscus curvature, and thus, the meniscus area, which would affect the air diffusion rate across the meniscus. However, we would ignore this secondary effect for simplicity here, leaving it for a future study. In any case, interestingly and somewhat surprisingly, we found that the air diffusion-driven flux, although clearly relevant to SHPo surfaces, is negligibly small when compared with the shear-driven and pressure-driven flow for typical flow conditions of watercraft, as analyzed in the result section with experiment data.

$$q_d \ll q_s; q_d \ll q_p \tag{3-8}$$

The net flux: Following the above approximation, the net flux of the air in the trench is practically zero.

$$q_s + q_p + q_d \approx q_s + q_p = 0 \tag{3-9}$$

which means the shear-drainage model for LIS can be used as a good approximation for SHPo surfaces as well. By integrating Equations (3-6) (3-7) into Equation (3-9), we can get the gradient of air pressure along the trench as

$$\frac{dP_{air}(x)}{dx} = \frac{2D}{1+2DN}\frac{c_{sl}w^2}{c_p d^3}\tau \tag{3-10}$$

3.2.4 A Unified Theory for the Combined Effect on Plastron Morphology

For the typical flow conditions of watercraft, both the water pressure and shear stress are significant, calling for a model that unifies the two to properly predict the morphology and eventually the fate of the plastron. Let us obtain the unified equation by solving the steady-state pressure gradient of air caused by the shear, Equation (3-10), with the boundary condition determined by the steady-state pressure of air in static water, Equation (3-4). Since the linear gradient of air pressure makes the air pressure at the mid-point of the trench the same as the air pressure in static water, i.e., $P_{\text{air}}(L/2) = sP_{atm}$, we can derive a unified equation to approximate the steady-state air pressure distribution inside a plastron that fills a micro-trench of length L and is sheared by the flow of water whose air saturation level is s as

$$P_{air}(x) = sP_{atm} + \frac{2D}{1+2DN}\frac{c_{sl}w^2}{c_p d^3}\tau\left(x - \frac{L}{2}\right) \tag{3-11}$$

which shows the air pressure increasing linearly in the x-direction. The difference between the water pressure on the trench and the air pressure in the plastron along the trench can be expressed with the pressure difference in static water, Equation (3-5), as follows:

$$\Delta P(x) = P_{water} - P_{air}(x) = \Delta P_{st} - \frac{2D}{1+2DN}\frac{c_{sl}w^2}{c_p d^3}\tau\left(x - \frac{L}{2}\right) \tag{3-12}$$

which shows the pressure difference decreasing linearly in the x-direction. In Equation (3-12), note the first term of RHS represents the effects of the hydrostatic pressure and air diffusion, and the second term represents the effects of shear by the flowing water. Due to the increasing air pressure along the trench, $\Delta P(x)$ has its maximum value at $x = 0$ (i.e., the front end of the trench) and minimum value at $x = L$ (i.e., the rear end of the trench) as

$$\Delta P(0) = \Delta P_{st} + \frac{D}{1+2DN}\frac{c_{sl}w^2}{c_p d^3}\tau L \tag{3-13}$$

$$\Delta P(L) = \Delta P_{st} - \frac{D}{1+2DN}\frac{c_{sl}w^2}{c_p d^3}\tau L \tag{3-14}$$

To help conceptualize how the pressure difference is determined on a longitudinal trench SHPo surface moving underwater (e.g., SHPo surfaces on a watercraft), Equation (3-12) is graphically presented in Figure 3-3(a), which visualizes how the pressure difference $\Delta P(x)$ (the vertical arrows in the figure) is determined by the hydrostatic pressure P_H, air saturation level s, and the location along the trench for a given SHPo surface (i.e., w, d, c_s, c_p) and fluid properties (i.e., D, N, s, P_{atm}). If $\Delta P(x)$ is larger than the largest Laplace pressure possible, i.e., $\Delta P_{\sigma,max}$, or smaller than the smallest Laplace pressure possible, i.e., $\Delta P_{\sigma,min}$, depinning would occur at the location x. It also shows the front portion of the trench would be the most vulnerable to the plastron depinning and trench wetting.

To help design trench SHPo surfaces suitable for drag reduction, Figure 3-3(b) visually explains a few important trends that make it more difficult to maintain the full plastron: (i) increasing hydrostatic pressure P_H (i.e., the surface is immersed deeper), (ii) decreasing air saturation level s

(i.e., the water is more undersaturated with air), (iii) increasing shear stress τ by the flowing water (i.e., water flows faster), and (iv) increasing trench length L (i.e., a longer trench is used).

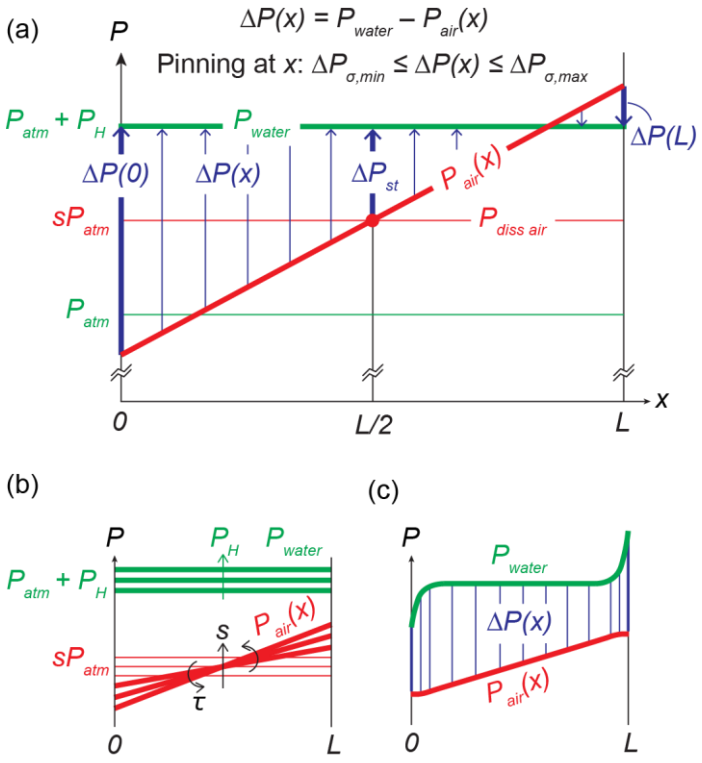

Figure 3-3. Pressure distributions along the trench. (a) The water pressure on the trench surface (thick green line) is $P_{water} = P_{atm} + P_H$. The partial pressure of air dissolved in water, $P_{diss\ air}$, is sP_{atm} (thin red line), which equals P_{atm} (thin green line) if the water at the free surface (in contact with ambient air) is saturated with the atmospheric air. The air pressure in the plastron $P_{air}(x)$ (thick red line) increases linearly with x. For the air-water interface to stay pinned on the trench top at x, the pressure difference between the water and the plastron, $\Delta P(x)$ (blue vertical arrows), should be sustainable by the Laplace pressure of meniscus ΔP_σ. (b) Trends of how the hydrostatic pressure P_H, air saturation level s, shear stress τ, and trench length L affect the pressure difference $\Delta P(x)$. (c) Deviations from the unified model by the dynamic effects of water flow near the front and rear end of the trench.

3.2.5 Plastron Length in the Unified Theory

A trench has a full plastron if the air-water interfaces are pinned on the trench top over its entire length. At a point along the trench, the interface is depinned if the pressure difference between water and air (Equation (3-12) and the vertical arrows in Figure 3-3(a)) exceeds, in magnitude, the maximum or minimum Laplace pressure the interface can counter with Equation (3-1). Wexler [29] used this pressure balance to obtain the length of steady-state plastron L_{ss} from the shear stress and trench geometry, while ignoring the hydrostatic pressure and diffusion, i.e., assuming $P_H = 0$ and $s = 1$. To address watercraft in field conditions, let us derive L_{ss} without the two assumptions by using the unified theory developed in this report. As the flow speed increases (along with the shear stress), the first occurrence of depinning would happen most commonly at the front end when $\Delta P(0) > \Delta P_{\sigma,max}$ (Figure 3-1(a-2)) or rarely at the rear end when $\Delta P(L) < \Delta P_{\sigma,min}$ (Figure 3-1(b-2)) with the hydrostatic pressure, air saturation level, and hydrophobicity of sample material determining which scenario would happen first. First, if the surface is in water with high hydrostatic pressure (large P_H) or low air saturation level (small s) such that $\Delta P_{st} > \Delta P_{\sigma,max}$, the air diffusion will make the plastron depinned inwardly (Figure 3-1(a-2)) and eventually depleted, even in static water. In this case, there is no pinned plastron at a steady state in any part of the trench, i.e., $L_{ss} = 0$ as

$$L_{ss} = 0, \text{ if } \Delta P_{\sigma,\max} < \Delta P_{st} \tag{3-15}$$

Second, if steady-state pinning is possible in static water, i.e., $\Delta P_{\sigma,min} \le \Delta P_{st} \le \Delta P_{\sigma,max}$, and also if the shear stress causes the plastron to be depinned-in (Figure 3-1(a-2)) at the front end, i.e., $\Delta P(0) > \Delta P_{\sigma,max}$, but leaves it pinned (Figure 3-1(a-1) or (b-1)) at the rear end, i.e., $\Delta P_{\sigma,min} \le \Delta P(L) \le \Delta P_{\sigma,max}$, Equations (3-13) and (3-14) are reduced to $(\Delta P_{\sigma,max} + \Delta P_{\sigma,min})/2 < \Delta P_{st} \le \Delta P_{\sigma,max}$. As the shear

stress increases, the pinned plastron becomes shorter, and its length L_{ss} can be derived from Equation (3-13) and $\Delta P(0) = \Delta P_{\sigma,max}$ by replacing L with L_{ss}, as

$$L_{ss} = \left(\Delta P_{\sigma,\max} - \Delta P_{st}\right)\frac{\phi d^3}{w^2\tau}, \text{ if } \frac{\Delta P_{\sigma,\min} + \Delta P_{\sigma,\max}}{2} < \Delta P_{st} \le \Delta P_{\sigma,\max} \tag{3-16}$$

where $\phi = \frac{1+2DN}{D}\frac{c_p}{c_{sl}}$.

Third, if steady-state pinning is possible in static water, i.e., $\Delta P_{\sigma,min} \le \Delta P_{st} \le \Delta P_{\sigma,max}$, and also if the shear stress causes the plastron to depin-out (Figure 3-1(b-2)) at the rear end, i.e., $\Delta P(L) < \Delta P_{\sigma,min}$, but leaves it pinned (Figure 3-1(a-1) or (b-1)) at the front end, i.e., $\Delta P_{\sigma,min} \le \Delta P(0) \le \Delta P_{\sigma,max}$, Equations (3-13) and (3-14) are reduced to $\Delta P_{\sigma,min} \le \Delta P_{st} < (\Delta P_{\sigma,max} + \Delta P_{\sigma,min})/2$. Since the strong shear of high-speed flows has been observed to remove overgrowing air, here we reflect the observed phenomenon by assuming ΔP at the front and rear end of the steady-state plastron equal $\Delta P_{\sigma,max}$ and $\Delta P_{\sigma,min}$, respectively, which essentially ignores the effect of hydrostatic pressure and air diffusion. Under this assumption, the pressure gradient inside a steady-state plastron can be expressed as $(\Delta P_{\sigma,max} - \Delta P_{\sigma,min})/L_{ss} = -dP_{air}(x)/dx$, which reduces Equation (3-10) to

$$L_{ss} = \left(\frac{\Delta P_{\sigma,\max} - \Delta P_{\sigma,\min}}{2}\right)\frac{\phi d^3}{w^2\tau}, \text{ if } \Delta P_{st} \le \frac{\Delta P_{\sigma,\min} + \Delta P_{\sigma,\max}}{2} \tag{3-17}$$

As the shear stress increases, the plastron in the front portion of the trench is depinned inwardly (Figure 3-1(a-2)), while that at the rear end is assumed to be pinned and $\Delta P(L) = \Delta P_{\sigma,min}$. Note that for $\Delta P_{st} = (\Delta P_{\sigma,max} + \Delta P_{\sigma,min})/2$, the values of Equation (3-16) and Equation (3-17) coincide, and the depinning-in at the front portion and depinning-out at the rear portion of trench occur simultaneously. Fourth, if the water has small P_H or large s such that $\Delta P_{st} < \Delta P_{\sigma,min}$, air diffusion

will make the plastron depinned outwardly and repeat the pinning and depinning (Figure 3-1(b)). While not being depleted, the plastron does not maintain a pinned state, either. However, if we assume the overgrowing air is removed by shear so that effectively a full plastron can exist at steady state, L_{ss} can be derived in the same way as the third case and expressed with Equation (3-17) as well.

In reality, a plastron cannot be longer than the trench it is in. In the above cases, if the shear stress is low and the trench is short such that the steady-state plastron is calculated to be longer than the trench, i.e., $L_{ss} > L$, the plastron length should equal the trench length, i.e., $L_p = L$. On the other hand, if the steady-state plastron is shorter than the trench, i.e., $L_{ss} < L$, at least a portion of the trench is depinned, and the trench would not have a full plastron. For drag reduction, one should design trenches to be shorter than the steady-state plastron length, i.e., $L < L_{ss}$, so that the trench can have a full or nearly-full plastron.

To show how the Equations (3-15), (3-16), and (3-17) is utilized to predict the fate of plastron, we present an exemplary map of steady-state plastron length L_{ss} in Figure 3-4, which was drawn for a re-entrant trench SHPo surface with w = 90 μm, p = 100 μm, θ_a = 116°, and θ_r = 101° and immersion depth H = 0.1 m, which was typical for the previous boat tests [19]. Figure 3-4 shows L_{ss} decreasing with the shear stress τ and increasing with the trench depth d and air saturation levels s (s = 99%, 100%, and 101%), which correspond to Equations (3-15), (3-16), and (3-17), respectively. The trench length L = 70 mm used in the previous boat experiments [19] is also plotted on the map as an important reference. For s = 99%, which represents $\Delta P_{\sigma,max} < \Delta P_{st}$, L_{ss} is zero regardless of d and τ because the air will diffuse out from the plastron even in static water. For s = 100%, which represents $(\Delta P_{\sigma,max} + \Delta P_{\sigma,min})/2 < \Delta P_{st} \leq \Delta P_{\sigma,max}$, L_{ss} decreases with τ and

increases with d. If the steady-state plastron is longer than the trench, i.e., $L_{ss} > L$, the trench can have a full plastron; if not, $L_{ss} < L$, the trench cannot have a full plastron. According to the map, the 70 mm long trenches can have a full plastron if the trench is relatively deep (e.g., $d > 100$ μm) and the flow is relatively slow (e.g., $\tau < 30$ Pa). Lastly, for $s = 101\%$, which represents $(\Delta P_{\sigma,max} + \Delta P_{\sigma,min})/2 \geq \Delta P_{st}$, the 70 mm trenches can have a full plastron if the trench is relatively deep (e.g., $d > 100$ μm) even for very high flow speeds (e.g., $\tau < 90$ Pa). Based on the air saturation level measured in this study for the same water (i.e., $s > 101\%$), the above plastron map by the unified theory explains why the 70 mm long trenches used by Xu [19] had a full plastron and provided successful drag reduction.

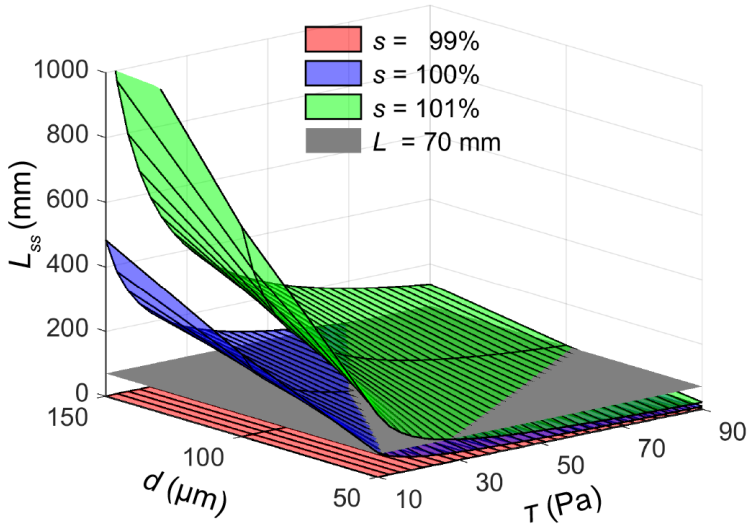

Figure 3-4. Theoretical steady-state length of the plastron. L_{ss} drawn for exemplary immersion depth $H = 0.1$ m and re-entrant trench width $w = 90$ μm as a function of trench depth d and shear stress τ on the SHPo surface, to explain how the air saturation level, shear stress, and trench depth affect the plastron stability. Three curved surfaces show L_{ss} for the water with three different air saturation levels (red: $s = 99\%$; blue: $s = 100\%$; green: $s = 101\%$). Trench length $L = 70$ mm used

by Xu [19] is shown as a flat grey plane. The space above the grey flat plane and below a colored curved plane is where a trench can have a full plastron.

3.2.6 The Effects of Dynamic Water Pressure and Interfacial Contamination

The above subsections focused on the effects of water pressure and shear stress and ignored secondary effects in order to establish the Equations (3-13), (3-14). and Figure 3-3(a). First, the water pressure was assumed to be uniform on the trench, i.e., $P_{water}(x) = P_{water}$, ignoring the effect of solid surfaces before ($x < 0$) and after ($x > L$) the trench for simplicity. However, the water pressure would decrease and increase momentarily as water flows past the front (leading) and rear (trailing) end of the trench, where the boundary condition changes from no-slip to slip and from slip to no-slip, respectively. Such dynamic pressure effect has been studied on SHPo surfaces with posts [39] but not on longitudinal trenches, which are typically modeled to be infinitely long. For now, let us present a qualitative analysis of the dynamic pressures to understand their effects on plastron morphology, as illustrated in Figure 3-3(c). The pressure difference between the water and the plastron at the front end would be smaller than the expected by Equation (3-13), suppressing the depinning-in at the front end. In other words, as the shear stress of water flow increases, depinning-in would start to occur slightly away from the front end. On the other hand, the pressure difference at the rear end would be larger than the expected by Equation (3-14), promoting the depinning-in at the rear end. The current discussion on dynamic pressure is supported by the experimental results later in this chapter. Dedicated investigations would be needed in the future to quantitatively assess how the dynamic pressure affects the plastron morphology on longitudinal trench SHPo surfaces.

Second, the surface tension of the air-water interface was assumed to be constant, ignoring the effects of potential contaminants inevitable in the environmental water. Surfactants in water can adsorb onto the air-water interfaces, where they can be advected by the shear and accumulate at the rear end of the trench [32]. The accumulation may lead to the formation of a stagnant-cap region, where the surfactant reaches its maximum interfacial concentration and reduces the surface tension by ~50% for a typical surfactant such as SDS [40]. Although the surfactant effect may dominate and practically eliminate the drag reduction in some cases [32], the negative effect is confined to a relatively short range (e.g., ~1 mm) at the rear end of the trench for typical flow conditions. Accordingly, the surfactant effect is relatively small for the long (> 10 mm) trenches used for drag reduction in turbulent flows [15, 17, 19, 20]. Nevertheless, the surfactant may induce a premature depinning at the rear end when the lowered surface tension is compounded by the dynamic pressure. Lastly, we would like to note numerous other secondary effects, such as the small particles and micro-organisms that may accumulate on the meniscus and decrease surface tension [41], the impact of solid particles onto the meniscus [42], and the influence of salinity level of seawater [43]. These other unforeseeable environmental effects are important motivations behind performing flow experiments in a field condition, such as a passenger motorboat on natural seawater for this study.

3.3 Experiments and Methods

3.3.1 The Boat and Underwater Cameras

The motorboat (13-foot Boston Whaler) retrofitted for the drag reduction research by Xu [19] was used for the current study. Since shear-induced wetting, which was not observed in the boat test of Xu [19], was found during the high-speed tow tank test by Xu [20] for similar SHPo surfaces,

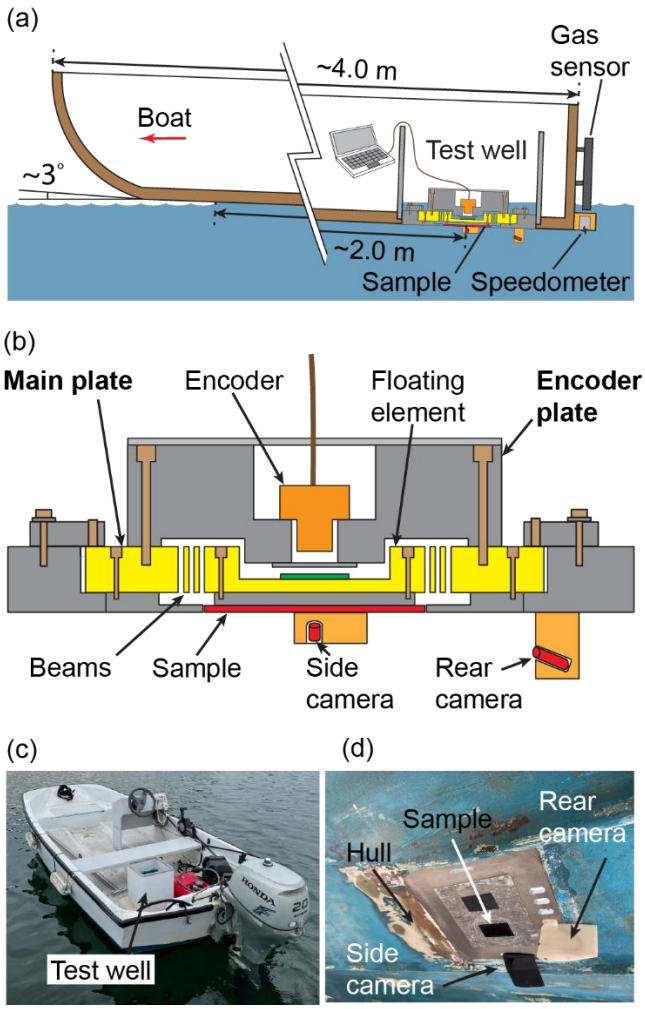

Figure 3-5. Experimental setup. (a) Schematic cross-section view of boat setup. (b) Schematic cross-section view of the testing unit, including shear sensor and camera setup. (c) Picture of the boat. (d) Picture of the bottom of testing well, taken by looking up from below in the air.

the boat was revamped to increase its top speed. By adding a hydrofoil stabilizer (Doel-Fin Hydrofoil, Davis Instruments) to the outboard motor, the boat's top speed was increased from 10 knots to 14 knots, expanding the maximum shear rate attainable on the sample surface from ~5500 s^{-1} to ~8300 s^{-1}. Testing well, which replaces a portion of the boat hull with a testing unit including sample surfaces, was installed on the boat as shown in Figure 3-5(a) (similarly to Xu [19]). A custom-developed shear stress sensor [44, 45] was used, as shown in Figure 3-5(b), to measure

the shear stress on the SHPo surface during the boat test with uncertainties of $0.1\tau_0$, where τ_0 is the measured shear stress on the smooth surface. An overall picture of the retrofitted boat is shown in Figure 3-5(c).

Two miniature underwater cameras with waterproof rating IP67 (TODSKOP 5.5 mm WiFi Borescope) were used to monitor the plastron status on the SHPo surface during the boat test, following the observation strategy by Yu [21]. Each camera was held in its own 3D-printed housing with a streamlined profile and installed as shown in Figure 3-5(d) (one black and one white) to observe the sample from a specific distance and direction so that together, the two cameras can accurately monitor the plastron states over the entire sample surface. The side camera observed the SHPo surface in the spanwise direction of the trench with an elevation angle β = 10±2°, which is the angle between the sample surface and the camera's central axis. When the sample is observed from this specific elevation angle β = 10±2°, the regions with $h/w \leq 0.17\pm0.04$ (i.e., pinned and slightly depinned plastron) appeared bright with the well-known silvery sheen, while the regions with $h/w > 0.17\pm0.04$ (i.e., depinned and no plastron) appeared dark. The smallest detectible depinning is determined by the minimum elevation angle, which is limited by the camera's depth of focus and the size of the surface to observe. On the other hand, from the rear camera, which observed the surface in the parallel direction of the trench, the regions with $h/w < d/w$ (i.e., any plastron) appeared bright, while the regions with $h/w = d/w$ (i.e., no plastron) appeared dark. For the experiments in this chapter, if a type of trenches appears bright from the side camera, it has a full or nearly-full plastron (i.e., deemed acceptable for drag reduction). If a type appears dark from the side camera, it has a degraded or no plastron (i.e., deemed unacceptable). Although not used to determine the acceptable and unacceptable plastron, the rear camera helped

us understand how the plastron is morphed inside the trench by differentiating the depinned from the no plastron.

3.3.2 Preparation of SHPo Samples

A series of SHPo surface samples were prepared, as shown in Figure 3-6. To test different Laplace pressure limitations, 3 different roughness types of longitudinal trenches shown in Figure 3-6(a) were prepared. The first roughness type was micro-trenches with a re-entrant shape at the top edge of the trench (named RE), which is the type used by Xu [19]. The second roughness type was micro-trenches without a re-entrant edge but covered with nano-grass (named NG). The third roughness type had both the re-entrance and nano-grass (named RE+NG). For each roughness type, 4 different trench depths were prepared, making a total of 12 samples (40 mm × 70 mm in size) each diced out from a 4-inch silicon wafer. Since there are 10 different combinations of trench widths and lengths on each sample, we may use a descriptive name for each trench geometry. For example, NG_d90-p75L30 points to the section filled with trenches of 75 μm pitch and 30 mm length on the sample of the nano-grass (but no re-entrance) type and 90 μm trench depth.

The micro-trenches were made on silicon wafers by developing 3 different fabrication processes of micro electro-mechanical systems (MEMS) based on photolithography, deep reactive ion etching (DRIE), and atomic layer deposition (ALD). For the 3 roughness types shown in Figure 3-6(a), the first type (RE) was micro-trenches with re-entrance at the top edge of the trench. The DRIE recipe was modified to create a ~250 nm of undercut below the ~500 nm thick silicon dioxide layer on top of trenches, thus creating the re-entrance, which is shown in the top SEM of Figure 3-6(a). The sawtooth-like sidewall below the re-entrance is by how DRIE works and should be considered smooth in a nanometer scale. The second type (NG) was removed of the re-entrant

edge by adding hydrofluoric wet etching after the DRIE. Following the wafer dicing, the surface was conformally coated with a ~55 nm thick Al_2O_3 layer by ALD and then immersed in a 60 °C deionized water bath for 10 minutes to roughen the Al_2O_3 into a nano-grass. The middle SEM picture of Figure 3-6(a) shows the top edge with no re-entrance and the entire surface uniformly covered with nano-grass with ~100 nm of roughness. The third type (RE+NG) had both the re-entrance and nano-grass, as shown in the bottom SEM picture of Figure 3-6(a), by omitting the hydrofluoric wet etching in the processing steps of the second type. For each of the three roughness types, 4 samples with increasing trench depths (i.e., d = 50.6, 67.5, 90, 153 μm) were prepared by increasing the etching time of DRIE. Hence, each of the 12 samples has a unique roughness type and trench depth. Once the trenches were formed, all the samples were cleaned by O2 plasma and then coated uniformly with the self-assembled monolayer (SAM) of 1H,1H,2H,2H-perfluorodecyltrichlorosilane (FDTS) in a custom-made vapor-based coater to achieve superhydrophobicity. The contact angles of water on FDTS-coated smooth silicon and Al_2O_3 nano-grass were measured with an in-house contact angle measurement apparatus and summarized in Table 3-1.

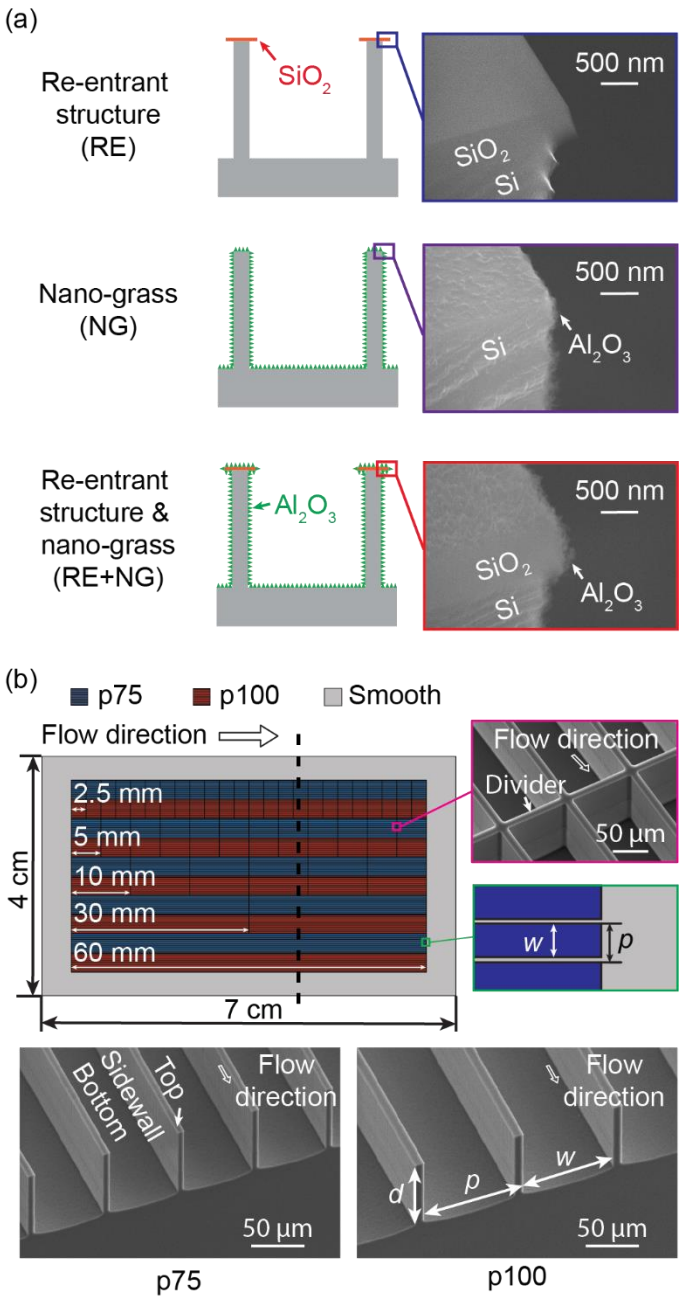

Figure 3-6. The SHPo samples prepared for experimental verification. (a) Illustration of 3 different trench types depending on the edge shape and surface roughness. The SEM pictures reveal the top edges of the cross-cleaved trenches as well as the nano-grass. (b) Each sample carries 10 parallel sections each containing 30 or 42 trenches. All trenches in this study have a gas fraction w/p = 0.9. The 40 mm × 70 mm sample has a 30 mm × 60 mm micromachined surface surrounded by a

smooth surface. The micromachined region has repeated sections of longitudinal trenches with p = 75 μm (drawn blue) and p = 100 μm (drawn red) combined with L = 2.5, 5, 10, 30, 60 mm. The inset SEM picture shows a spanwise divider that partitions a 60 mm trench into shorter trenches. The same arrangement was used for all the 12 samples (3 roughness types × 4 trench depths), providing 120 different trench geometries with one photomask. The SEM pictures of cleaved samples show the trenches of two different pitches and one depth d = 67.5 μm.

Table 3-1. Contact angles of water on FDTS-coated nano-grass and smooth surface.

Type of surface	θ (°)	θ_a (°)	θ_r (°)
FDTS-coated smooth Si	110 ± 1	116 ± 3	101 ± 1
FDTS-coated Al_2O_3 nano-grass	166 ± 1	166 ± 1	165 ± 2

On each sample, trenches with a combination of 2 different pitches (p = 75, 100 μm) and 5 different lengths (L = 2.5, 5, 10, 30, 60 mm) were fabricated, as schematically shown in Figure 3-6(b). A sample was cleaved along the vertical broken line drawn on the schematic to obtain the two SEM pictures (p75 and p100), which show the two different pitches. The gas fraction of all trenches were kept at 90%, i.e., w/p = 0.9. The 30 mm × 60 mm micromachined area in the middle was divided into 10 parallel sections each ~3 mm wide and containing 42 or 30 parallel trenches of p = 75 μm (shaded blue) or 100 μm (shaded red), respectively. The section width was, in part, designed based on the resolution of the side camera. To provide the 5 different trench lengths, 8 of the 10 parallel sections were further divided into multiple (2, 6, 12, or 24) shorter trenches, the top SEM showing one such partition. The smooth area (grey) outside the micromachined area (blue and red) was to prevent the flow disturbances by the gap between the sample and the surrounding

plate, as observed by Xu [20]. Since 12 different samples were fabricated to provide combinations of 3 roughness types (i.e., RE, NG, and RE+NG) and 4 trench depths (i.e., d = 50.6, 67.5, 90, 153 μm), a total of 120 different trench geometries have been prepared for flow experiments.

3.3.3 The Flow Experiments

To comprehensively compare the effects of hydrostatic pressure, air diffusion, and shear stress on different SHPo samples, we performed all the flow tests in brackish water with air saturation levels at 100–101% in the mouth of a creek (Ballona Creek, Los Angeles, California, U.S.A.) meeting the Pacific Ocean. The air saturation level was monitored regularly by a total gas sensor (Point Four^{TM} tracker, PENTAIR), and the specific testing area was determined for each test based on the air saturation level within the 2-mile range inside the creek. One end of the range was the creek's entry point into the ocean, where the air saturation level tended to be 104–106% due to the wind and waves on the ocean, while the other end was the farthest upstream point allowed by the transportation rules, where the air saturation level was measured to be constantly below 99%. The air saturation level gradually decreased away from the ocean but varied significantly by the tide and wind conditions, requiring us to measure the air saturation level regularly and often. At high tide, the ocean water would enter the creek, increasing the air saturation in the upstream end to as high as 100–101%, while at low tide the ocean water would retreat from the creek, decreasing the air saturation in the downstream end (i.e., the entrance point) to as low as 99–100%.

Each sample was tested with boat speeds varying from 2 m/s to 7.2 m/s with ~0.5 m/s intervals. For each test, the boat remained stationary at first, then accelerated to the target speed in ~5 seconds and maintained the target speed for ~40 seconds for observation. The sample was kept under water during the entire test trial (typically 30–40 min), and its immersion depth was measured to be

0.15±0.03 m for all tests. The boat was carefully trimmed (i.e., weight distributed carefully) to maintain a ~3° running (tilting) angle, measured by an inclinometer (H4A1-45 Inclinometer, RIEKER), and a constant waterline at all the target speeds. To estimate the shear stress on the SHPo surface for a given boat speed, a smooth 40 mm × 70 mm silicon sample, diced from 4-inch bare silicon water, was attached to the shear stress sensor [45] and its shear stress τ_0 was measured at different speeds multiple times. The shears stress on a smooth surface τ_0 underneath the boat has been measured with the custom shear sensor [45] over the range of boat speeds U used in the current study and plotted in Figure 3-7. The power regression line, which fits the experimental data reasonably well (especially considering the varying environmental conditions the field tests are subjected to), is used to estimate the shear stress for the plastron observation runs. The power regression also ensures the shear stress is zero when the boat speed is zero. The shear stresses on the SHPo surface were, then, estimated from that on the smooth surface from $\tau \sim 0.7\tau_0$, which was found in the previous research using similar surfaces and the same boat [19].

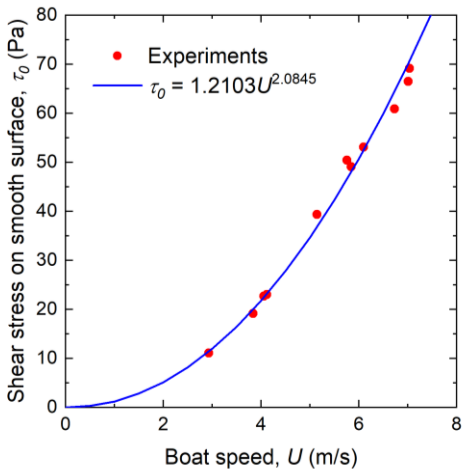

Figure 3-7. Shear stress on a smooth surface at different boat speeds. The experimental data fit the power regression line.

3.4 Results and Discussions

3.4.1 Image Pairs Collected and Key Trends Confirmed

The images from the side and rear cameras were analyzed as pairs to determine the state of plastron: (i) full or nearly-full plastron (i.e., $h/w \leq 0.17$ in this study, limited by the underwater cameras availability), (ii) degraded plastron (i.e., $0.17 < h/w < d/w$), and (iii) no plastron (i.e., $h/w = d/w$). We have analyzed all the sample images obtained from the boat tests – a pair of images at each of ~10 different boat speeds for each of the 12 samples, i.e., a total of ~120 image pairs with each covering 10 different trench types, producing ~1200 data points of plastron length. Among them, 4 sets of images for 4 selected flow speeds, with each set collecting the image pairs of all the 12 samples, are presented in Figure 3-8, Figure 3-9, Figure 3-10, and Figure 3-11, where colored outlines are often used on the two types (p = 75 μm and 100 μm) of 60 mm long trenches to assist readers in identifying the state of the plastron.

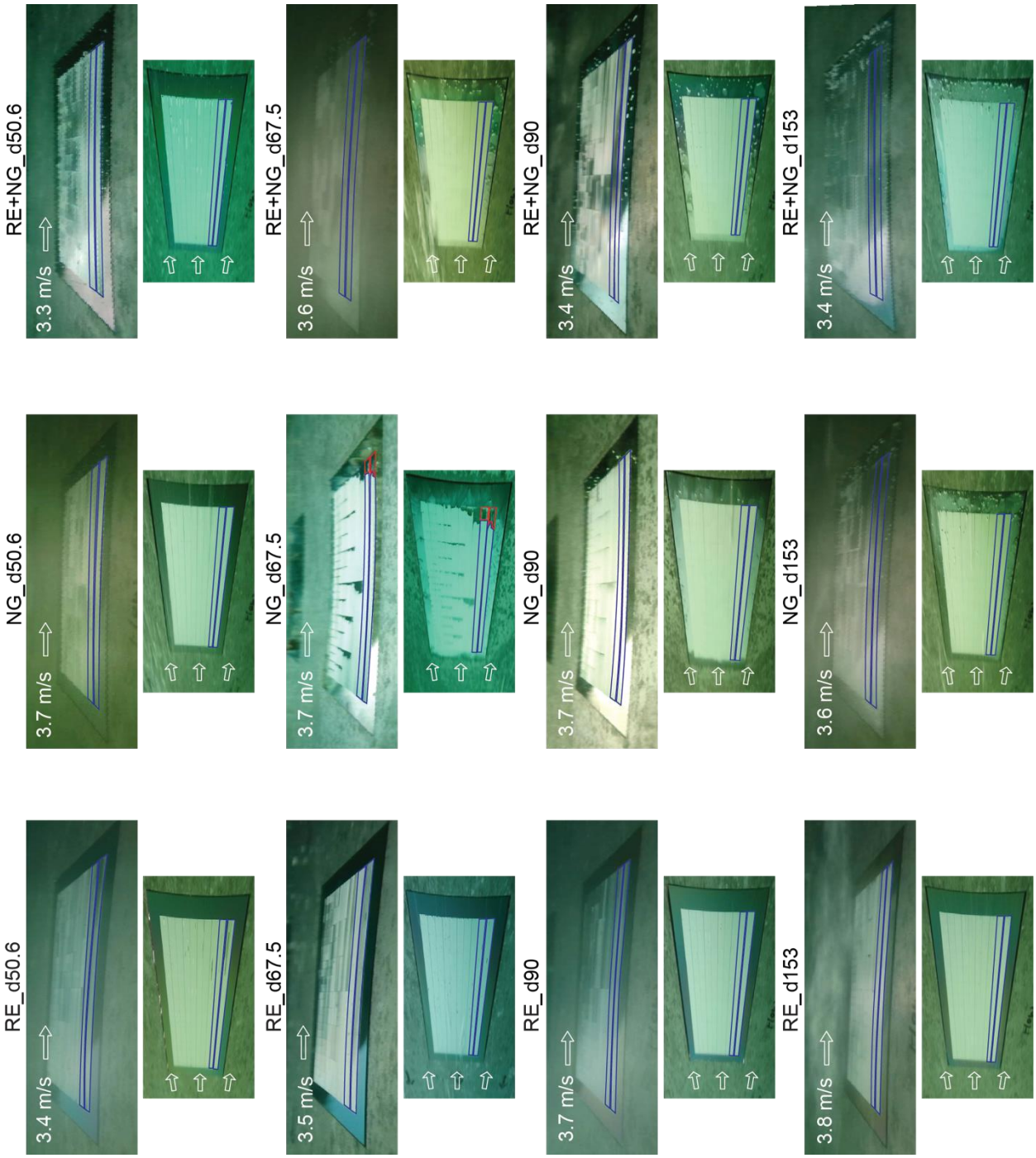

Figure 3-8. Sample images at speeds between 3.3–3.8 m/s. Blue indicates a pinned or slightly depinned plastron (i.e., $h/w \leq 0.17$); yellow indicates a depinned plastron (i.e., $0.17 < h/w < d/w$); and red indicates no plastron (i.e., $h/w = d/w$).

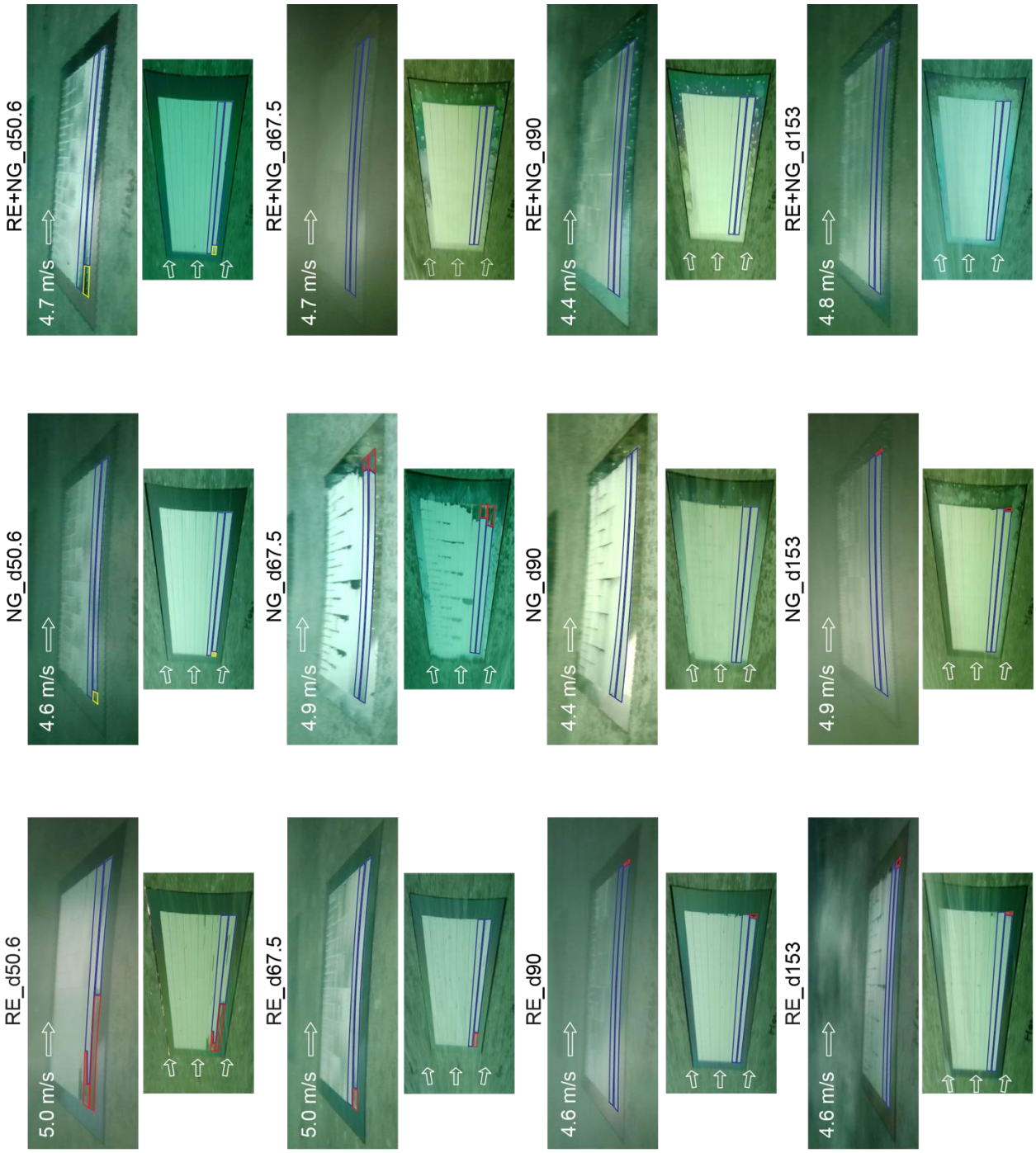

Figure 3-9. Sample images at speeds between 4.4–5 m/s. Blue indicates a pinned or slightly depinned plastron (i.e., $h/w \leq 0.17$); yellow indicates a depinned plastron (i.e., $0.17 < h/w < d/w$); and red indicates no plastron (i.e., $h/w = d/w$).

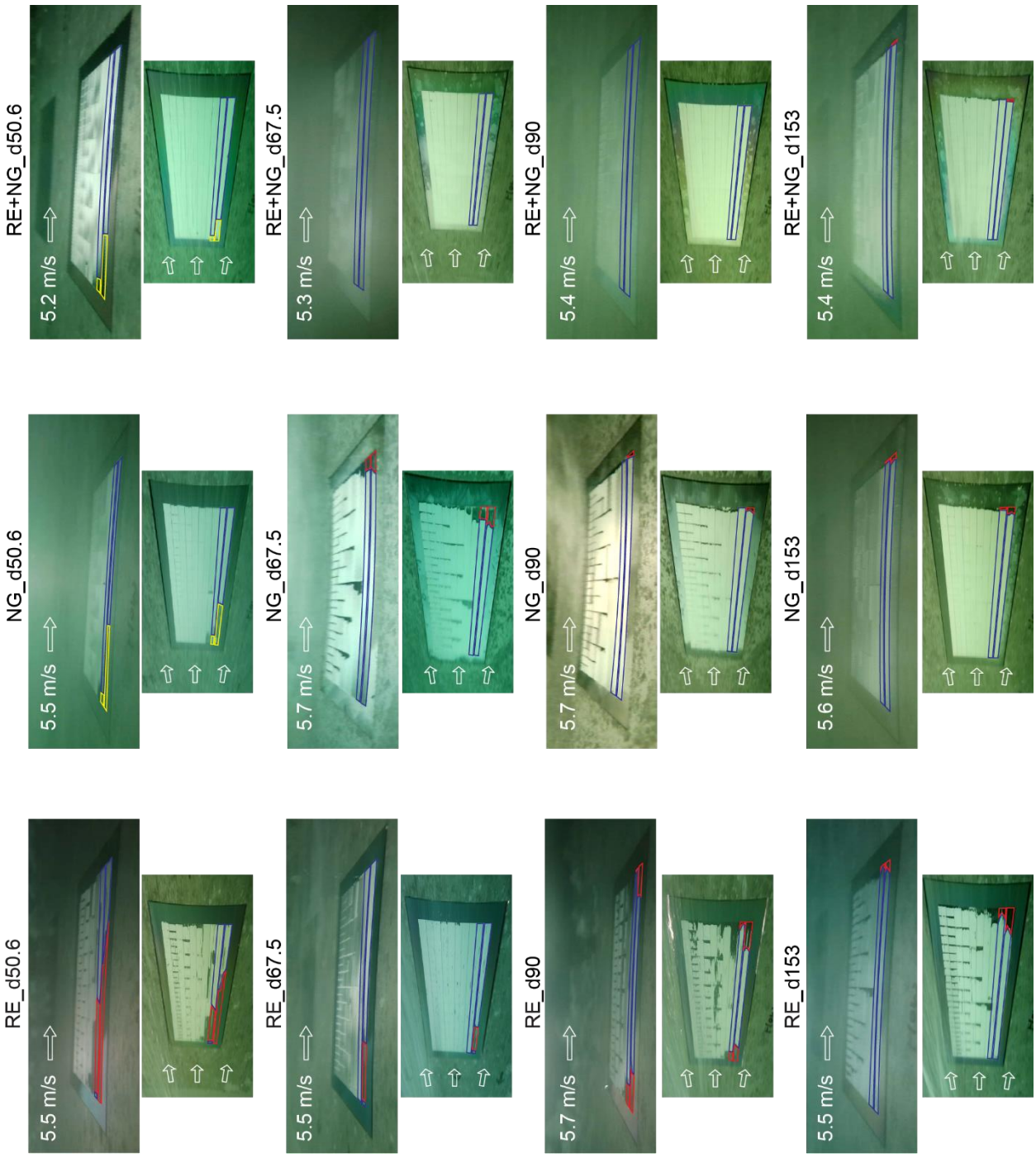

Figure 3-10. Sample images at speeds between 5.2–5.7 m/s. Blue indicates a pinned or slightly depinned plastron (i.e., $h/w \leq 0.17$); yellow indicates a depinned plastron (i.e., $0.17 < h/w < d/w$); and red indicates no plastron (i.e., $h/w = d/w$).

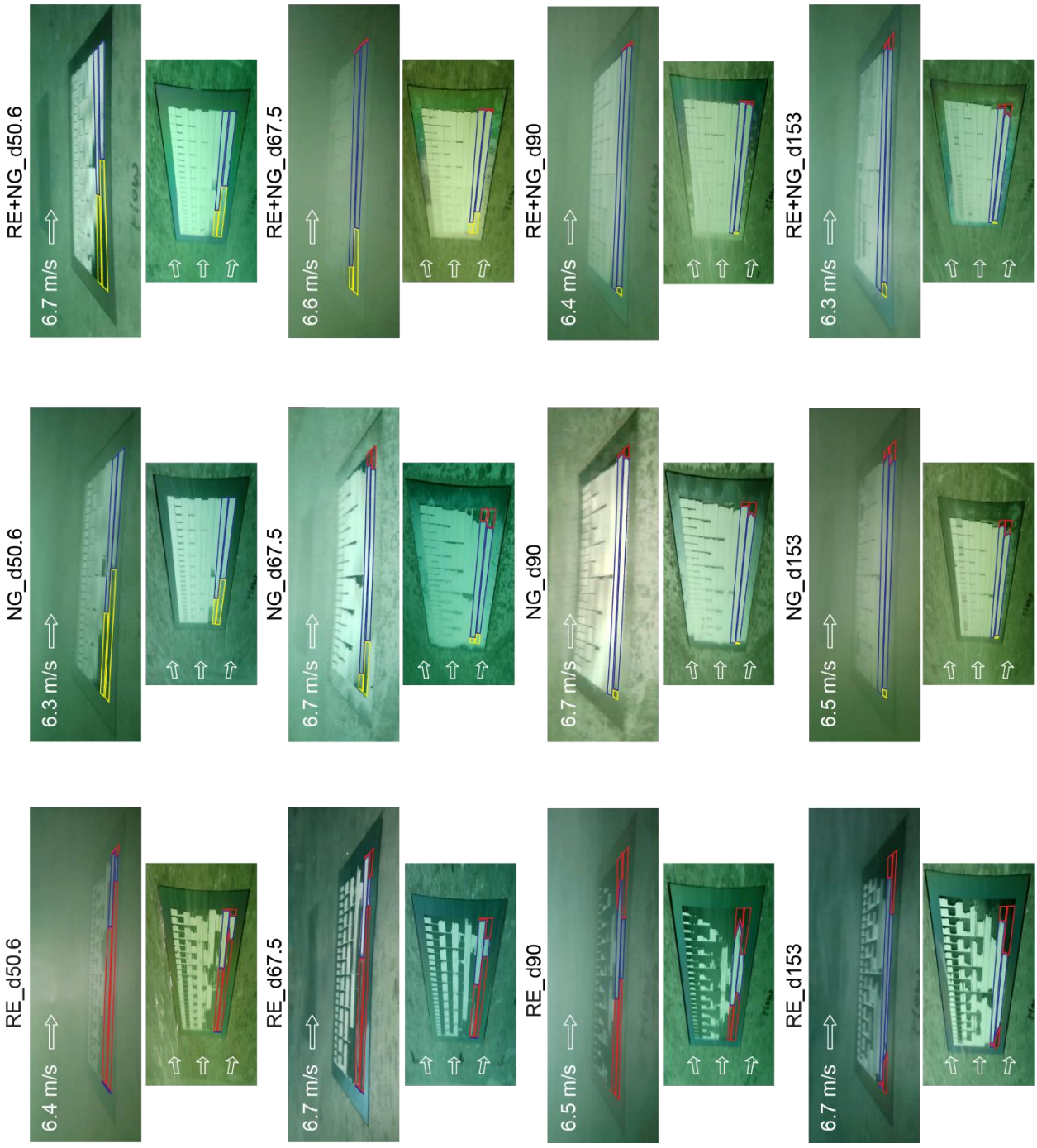

Figure 3-11. Sample images at speeds between 6.3–6.7 m/s. Blue indicates a pinned or slightly depinned plastron (i.e., $h/w \leq 0.17$); yellow indicates a depinned plastron (i.e., $0.17 < h/w < d/w$); and red indicates no plastron (i.e., $h/w = d/w$).

Throughout the collected data, the plastron length L_p increased with trench depth d and decreased with trench width w (or pitch p) and boat speed U, as expected from the theory. Several sample images were selected in Figure 3-12 to reveal key trends. The selected ones were more often RE samples because the loss of plastron was rare (i.e., difficult to spot trends) on NG and RE+NG samples. Figure 3-12(a) shows a rear-view picture of an RE sample with d = 67.5 μm (i.e., RE_d67.5) at U = 5.5 m/s. The image revealed trenches with p = 75 μm had longer plastron than those with p = 100 μm on 60 mm long trenches, indicating stronger plastron stability on narrower trenches, as expected. Figure 3-12(b) presents 4 side-view pictures of 4 RE samples with d = 153 μm (i.e., RE_d153) taken at 4 different flows speeds (U = 3.8, 4.6, 5.5, 6.7 m/s). The images of 60 mm long trenches revealed full or nearly-full plastrons, i.e., ($L_p = L < L_{ss}$) at speeds up to U = 5.5 m/s but degraded plastron ($L_p = L_{ss} < L$) at U = 6.7 m/s, indicating weakened plastron stability at higher flow speeds, as expected. Incidentally, most of the 60 mm long trenches on RE sample (i.e., RE_d153-p75L60 and RE_d153-p100L60) were found to maintain a full or nearly-full plastron up to U = 5.5 m/s, corroborating the existence of plastron reported in Xu [19]. Figure 3-12(c) presents 4 side-view pictures of 4 RE+NG samples with 4 different trench depths (i.e., RE+NG_d50.6, RE+NG_d67.5, RE+NG_d90, and RE+NG_d153) at a high speed (U = 6.3–6.7 m/s). While the depinning of plastron by high shear stress was apparent on shallow trenches (RE+NG_d50.6), the degraded plastron on the front region of the trench was shortened and disappeared with increasing trench depth, as predicted by the theory.

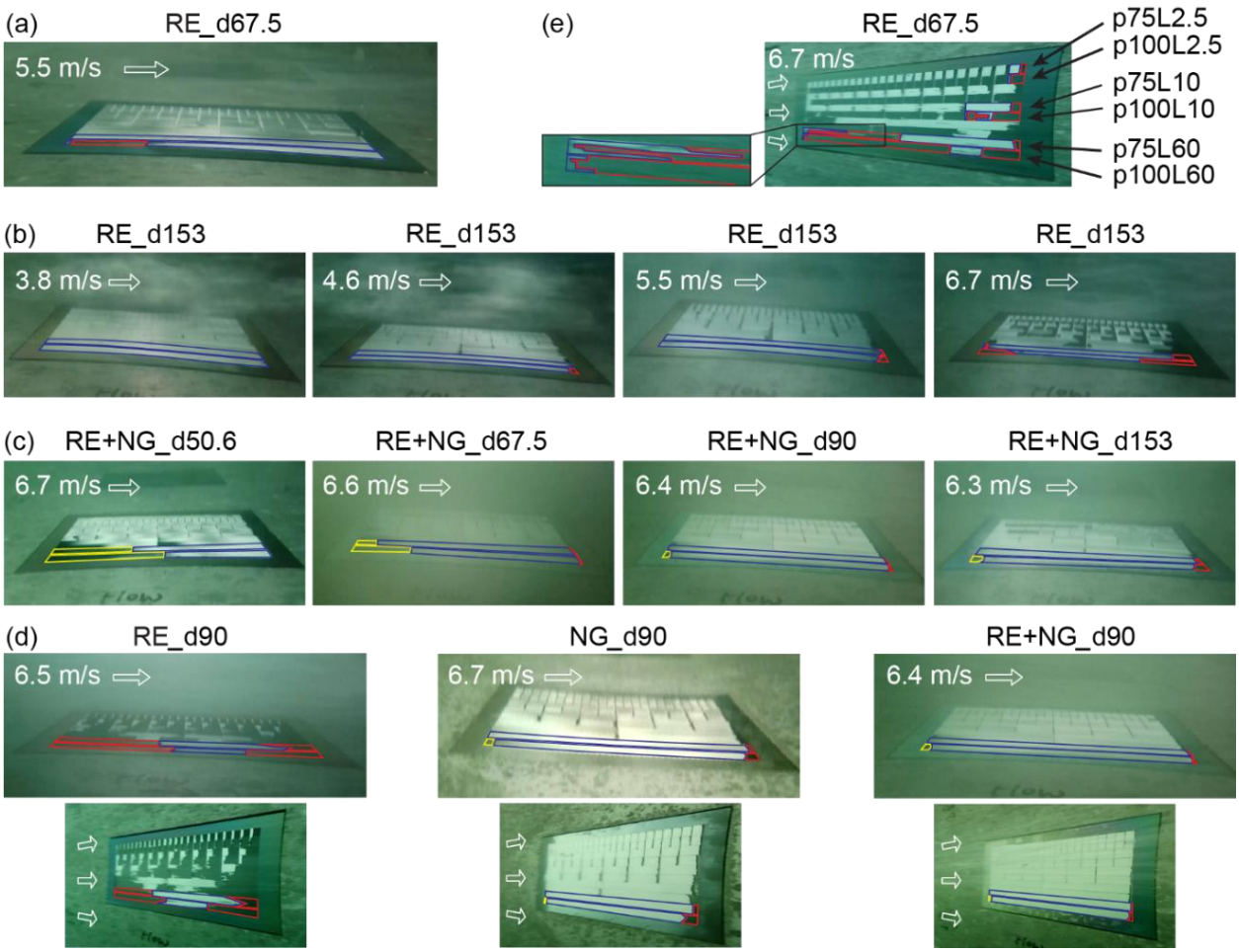

Figure 3-12. Sample images for key trends. Some regions are color-outlined to help identify the plastron states, which were determined using the corresponding image pairs in Appendix E. Blue, yellow, and red indicate the pinned or slightly depinned (i.e., $h/w \leq 0.17$), depinned (i.e., $0.17 < h/w < d/w$), and no (i.e., $h/w = d/w$) plastron, respectively. (a) The effect of trench width w. Narrower trenches maintained the plastron better. (b) The effect of shear stress τ. Slower flows maintained the plastron better. (c) The effect of trench depth d. Deeper trenches maintained the plastron better. (d) The effect of nano-grass. For each pair of images, the top image was taken by the side camera, and the bottom image was taken by the rear camera. While the plastron was lost significantly on RE at this high flow speed (U = 6.4–6.7 m/s), a full or nearly-full plastron was

found for all trenches on NG and RE+NG, demonstrating the effectiveness of adding nano-grass. (e) Effects of dynamic water pressure and interfacial contamination. Regions with trench lengths L = 2.5 mm, 10 mm, and 60 mm are outlined. The inset picture shows the pinned or slightly depinned plastrons at the front end of the 60 mm trenches.

Figure 3-12(d) presents 3 pairs of pictures taken from 3 samples of different roughness types with d = 90 μm at a high speed (U = 6.4–6.7 m/s). On the sample with re-entrance but without nano-grass (i.e., RE_d90), most trenches had regions of no plastron. In comparison, on the samples with nano-grass regardless of re-entrance (i.e., NG_d90 and RE+NG_d90), nearly all trenches were found to have a full or nearly-full plastron, demonstrating the effectiveness of adding nano-grass to the micro-trench. Incidentally, note the RE sample was populated with no plastron and full or nearly-full plastron but no degraded plastron. The same was true for all other RE samples as shown in Figure 3-8 to Figure 3-11. The lack of the degraded plastron on RE was likely because once the meniscus is depinned from the top edge, where the re-entrance (on which θ_a = 180°, effectively) maximizes the Laplace pressure, the smooth sidewalls (on which θ_a ~ 116°) could not provide the same level of Laplace pressure, letting the contact line slide down quickly to the fully wetted state (i.e., no plastron). The unstable meniscus on the smooth sidewall may also explain the loss of plastron by the high pressure fluctuations in turbulent flows [46]. On the other hand, while the region of no plastron was negligible on the NG and RE+NG samples, degraded plastrons were found in shallow trenches at high speeds, as shown in Figure 3-10 and Figure 3-11. The degraded plastron was likely because the rough sidewalls (on which θ_a ~ 166°) provided a similarly large Laplace pressure as the top edge. In other words, the nano-grass, while increasing the plastron stability, especially calls for an appropriate observation method to differentiate the acceptable (i.e.,

full and nearly-full) plastron from the unacceptable (i.e., degraded and no) plastron on SHPo surfaces for drag reduction.

3.4.2 Deviations from the Linear Increase of Air Pressure in Plastron

Recall the secondary effects that may cause the plastron morphology to deviate from the theoretical prediction of linearly increasing pressure difference along the trench, as discussed in Section 3.2.6. First, for an example, as shown on the 60 mm length trenches in Figure 3-12(e) (i.e., p75L60, p100L60), while a significant portion of the front region had no plastron, the very front end was found to have a plastron. This is a deviation from the linear theory, which predicts the pressure difference increasing toward the front of the trench up to the very end. We believe that this small but interesting deviation from the front wetting can be explained by the pressure of the flowing water decreasing right past the front end, as explained in Figure 3-3(c). Second, throughout the collected images, including Figure 3-12(e), the plastron was frequently found to be lost at the rear end. This is a deviation from the linear theory, which predicts the pressure difference decreasing toward the rear of the trench up to the very end (note $P_{water} > P_{air}$ under large enough P_H, which is the current experimental condition). We believe this deviation, which we will call "rear wetting", may be partially explained by the water pressure increasing near the rear end, as explained in Figure 3-3(c). However, the deviation at the rear end was found to be more common and more pronounced, when compared with the deviation at the front end. For example, rear-wetting was observed on all trenches of all RE samples at $U > 4.6$ m/s and some trenches on NG and RE+NG samples, as shown in Figure 3-8 to Figure 3-11. The stronger deviation at the rear end may be explained by the pressure increase by the dynamic flow exasperated by the negative effects of interfacial contaminants, as explained in Section 3.2.6. Also, the rear wetting was not directly affected by the trench length, making its wetting effect more significant in shorter trenches. For

example, on the RE_d67.5 sample shown in Figure 3-12(e), the rear wetting had a relatively small effect (< 5%) on p75L60, but a large effect (~50%) on p100L2.5. In addition, the rear wetting tended to be more significant on deeper trenches, possibly because the trapped air there was more compressible and provided less dynamic resistance against depinning. In any case, the rear wetting was found to be ~4 times shorter on NG and RE+NG than on RE, which shows a significant benefit of nano-grass to prevent rear wetting in future applications.

The mechanism of rear wetting calls for a significant investigation in the future, as it seems inevitable for drag-reducing SHPo surfaces. As discussed in Section 3.2.6, the rear wetting may arise from the increased local water pressure when the boundary condition changes from slip to no-slip at the trench end, combined with the stagnant cap formed by the surfactant (or particles) advected to the trench end. While the former would require numerical and experimental studies of hydrodynamic issues involving free surfaces, the latter would further involve diffusion and interfacial phenomena. Regarding the surfactant effect, the two-dimensional simulations of Landel [32] reported a stagnant cap region on the SHPo trench with Peclet number $Pe = LU/D_I > 10^3$, where U is bulk velocity and D_I is the diffusion coefficient of the interfacial surfactant. Assuming a typical environmental surfactant sodium dodecyl sulfate (SDS), which has $D_I = 7 \times 10^{-10}$ m^2/s, for our trenches, i.e., $L = O(10^{-3}–10^{-2}$ m), and the maximum speed, i.e., $U = 7.2$ m/s, $Pe = O(10^7–10^8)$, which suggests a stagnant cap region at the rear end. Since the theory of Landel [32] only fits two regimes where the stagnant cap either covers the entire plastron or does not exist, additional advancement would be desired to estimate the distribution of stagnant cap on a SHPo trench, which is likely affected by the trench dimensions, water speed, and surfactant concentration and properties, as discussed in the studies of stagnant cap on arising bubbles [47, 48].

3.4.3 Comparisons with the Unified Theory

The actual plastron lengths L_p on 60 mm long trenches were measured from all the images using ImageJ and plotted in Figure 3-13, and the steady-state (theoretical) plastron lengths L_{ss} calculated from Equation (3-16) were drawn as color-shaded ranges in the same figure for comparison. For the calculation, the flow conditions of the experiments were used: air saturation level within s = 100–101%, immersion depth at H = 0.15 m; and the shear stress τ on the SHPo surface estimated from the boat speeds U measured using the regression equation in Section 3.3.3. Since the maximum trench length fabricable was 60 mm (i.e., L_{max} = 60 mm, limited by the wafer size), plastron lengths greater than 60 mm (i.e., $L_p > L_{max}$ = 60 mm) were not possible and could not be tested in this study. Instead, we increased the boat speed beyond the ones used by Xu [19], which did not observe any shear-driven wetting, to decrease the theoretical plastron length L_{ss}, so that the actual plastron length can be revealed experimentally (i.e., $L_p = L_{ss} < L_{max}$). If $L_{ss} < L_{max}$ = 60 mm, the front of the 60 mm long trench should be wetted, and the plastron length can be observed as $L_p = L_{ss}$. In the graphs the experimental data fit the unified theory reasonably well for NG and RE+NG; deviations occurred only on RE at U > ~6 m/s. Even though the theoretical L_{ss} on RE is similar to those on NG and RE+NG, the actual (experimental) L_p on RE was found to be significantly smaller, which may be caused by the high pressure fluctuations in turbulent flows [46] and rear wetting, which were not reflected in the unified theory. The rear wetting made the plastron shorter than the theory also on NG and RE+NG, especially for d = 90, 153 μm, but the effect was negligible (< ~8%). There was no significant difference between NG and RE+NG, as expected from the theory. It should be noted that, for simplicity, the theoretical shear stress on the SHPo surface was estimated using the shear stress on a smooth surface by assuming 30% drag reduction for all the speeds, which was the typical drag reduction value from the previous works for p100 [19, 20] with

gas fraction w/p = 0.9 in turbulent boundary flows for U > ~5 m/s. Although the theoretical shear stress should be 10–20% larger than the estimated ones used in Figure 8 for U < ~5 m/s, this effect was expected to be negligible because a larger L_{ss} would not change the fact that all the surfaces should have a full plastron over the entire trench length at low speeds (i.e., U < ~5 m/s) due to small shear stress. Besides, the theoretical shear stress for p75 should be 5–10% larger than that on p100 in the same water flow due to the smaller pitch [20], increasing L_{ss} values for p75 surfaces by 5–10%, while the experimental values will still fit the theoretical ranges reasonably well. Overall, the unified theory derived in this paper has been proven to be valid in estimating the plastron length on micro-trench SHPo surfaces in turbulent flows, providing useful guidance for designing SHPo surfaces for drag reduction. In addition, NG and RE+NG have been demonstrated to maintain a full plastron in the 60 mm long trench in turbulent boundary layer flows up to 7.2 m/s in accordance with the theory, suggesting a direction toward high-performance SHPo surfaces for drag reduction.

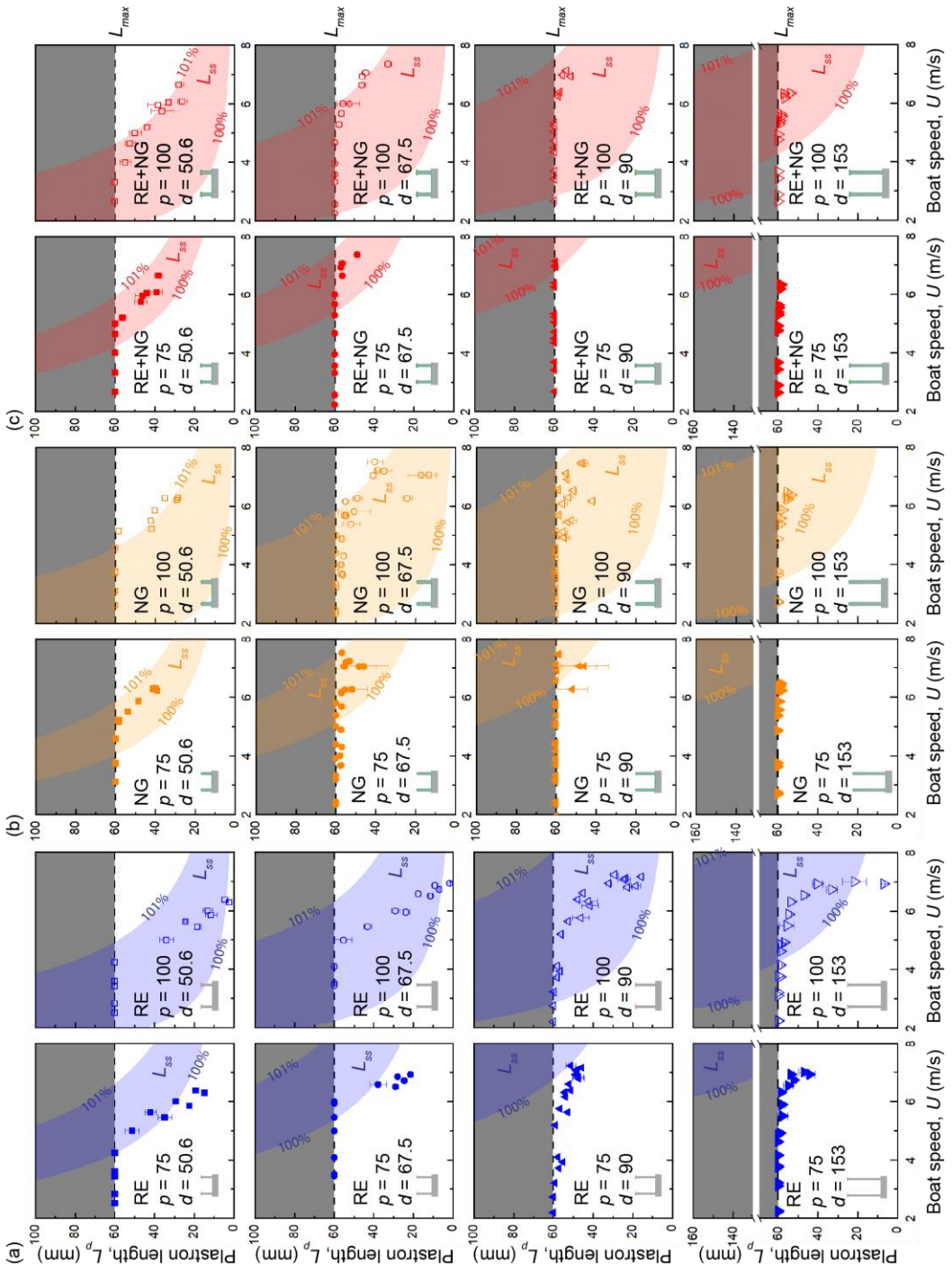

Figure 3-13. Comparison of experimental results and theory. Experimentally obtained plastron length L_p and theoretically predicted ranges of steady state plastron length L_{ss} as function of boat speed U for the experimental conditions in this study. (a) RE: trench with the re-entrant top edge and smooth surface, drawn blue. (b) NG: trench without the re-entrant top edge and nano-grass

surface, drawn orange. (c) RE+NG: trench with re-entrant top edges and nano-grass surface, drawn red. The boat speed varied between ~2 m/s < U < ~7 m/s. On each graph, the area above L_p = 60 mm was made dark to indicate an impossible range. For comparison, the theoretical prediction is drawn as a shaded area for the experimental conditions used: air saturation level 100% < s < 101%, immersion depth H = 0.15 m. Considering the numerous factors that were uncontrollable during the boat tests over several months, the experimental results match the theoretical predictions quite well.

3.4.4 Scaling Comparison of the Three Air Fluxes in a Trench

The air diffusion across the air-water interface (meniscus) will lead to a diffusion-driven air flow inside the plastron. Since air diffusion rate across the meniscus varies with the Laplace pressure and meniscus area, the diffusion-driven flow flux scales as $q_d \sim k_p \sigma L$, where k_p is the interfacial mass transfer coefficient, σ is the air-water interfacial tension. In turbulent boundary layer flows, k_p is defined by "film theory" [49] as

$$k_p = \frac{D}{\delta_c} \frac{M}{k_H \rho_{air}} \tag{3-18}$$

where D is the diffusion coefficient of air (i.e., 1.75–2.00×10^{-5} cm^2/s); M is the molecular weight of air (i.e., 29 g/mol); ρ_{air} is the density of air (i.e., 0.0012 g/cm^3); δ_c is diffusion length, which depends on the flow condition. Henry's constant k_H (i.e., 1.21–1.34 atm/mM) is irrelevant to the hydrostatic pressure unless the immersion depth is very large (e.g., k_H increases ~14% at immersion depth ~1000 m [50]). Ling [27] studied the effect of Reynolds number on diffusion length in turbulent boundary layer flow over a SHPo surface and found the relation between the Sherwood number $SH_{\Theta 0}$ and friction Reynolds number $Re_{\tau 0}$, where subscript 0 indicates a smooth

surface, as $SH_{\Theta 0} = 0.34Re_{\tau 0}^{0.913}$. Here, $SH_{\Theta 0} = \Theta_0/\delta_c$, where Θ_0 is the momentum boundary layer thickness on a smooth surface and approximated to be $\Theta_0/\hat{x} = 0.01277Re_x^{-0.1341}$ [51] for the purpose of scaling estimation, with the Reynolds number defined as $Re_x = U\hat{x}/\nu$, where $\hat{x}$ is the streamwise distance from the leading edge of immersed boat hull to the sample surface ($\hat{x}$ is labeled as ~2 m in Figure 5(a)). Since the boat is tilted and elevated (by planing) when it speeds up, i.e., $\hat{x}$ decreases slightly with U, the tilting angle and waterline of the boat were measured for all the individual experiments to estimate $\hat{x}$ for each test run. For the purpose of estimating frictional Reynolds number $Re_{\tau 0} = \delta_0(\tau_0/\rho)^{0.5}/\nu$, the boundary layer thickness on the smooth surface δ_0 can be approximated to be $\delta_0/\hat{x} = 0.16Re_x^{-1/7}$ [52] for the purpose of scaling estimation, and the shear stresses on smooth surface τ_0 were established in (a) The friction coefficients of two smooth surfaces attached to two floating elements of the shear comparator and subjected to different boat speeds. The nearly identical shear stress values measured from the two floating elements as well as the similar empirical curve at various boat speeds show the reliability of the sensor and also confirm the two surfaces experience the same flow condition. (b) The friction coefficient of a smooth surface attached to one floating element of the shear comparator and subjected to different Reynolds numbers. The results were obtained on smooth surface while performing drag reduction tests for the 8 SHPo samples which was attached to the other floating element in the shear comparator. . In the turbulent boundary layer flow under the boat setup, using the relations above, we can estimate δ_c at the minimum and maximum Reynolds number ($Re_x = 5.17\times10^6$ and 1.29×10^7, corresponding to the minimum and maximum boat speed U = 2.0 m/s and 7.2 m/s) to be 6.75 and 1.93 μm, respectively. The parameters estimated using the relations above are listed in Table 2. By inputting these values in Equation (3-18), we obtain $k_p = 0.5\times10^{-10} – 1.8\times10^{-10}$ m/(s·Pa).

Table 3-2. Approximation for parameters on boat tests. U and $\hat{x}$ were measured from experiments, and other parameters were estimated from theoretical equations.

U (m/s)	$\hat{x}$ (m)	Re_x	Θ_0 (10^{-3} m)	$Re_{\tau 0}$	δ_c (10^{-6} m)
2.0	2.3	5.17×10^6	3.70	3255	6.75
7.2	1.6	1.29×10^7	2.27	7548	1.93

By considering micro-trenches with aspect ratio d/w = 1 and gas fraction w/p = 0.9, based on Equations (3-6) and (3-7) the shear-driven flow and the pressure-driven flow scale as $q_{sl} \sim 10^{-3}\tau w^3 \mu_{air}^{-1}$ and $q_p \sim 10^{-2} h^3 \sigma \mu_{air}^{-1} L^{-1}$, respectively. Then, we can estimate the magnitude of each flux inside the trench by substituting the exemplary values into the scaling equations. By assuming (i) the trench has a width and depth of $w = h$ = 90 μm and length of L = 60 mm and (ii) the shear stress on the SHPo surface is $\tau \sim$ 50 Pa, the scaling equations lead to $q_d/q_{sl} \sim O(10^{-4})$ and $q_d/q_p \sim O(10^{-4})$. Therefore, we conclude that, for the trench geometries and flow conditions relevant to the current study, the diffusion-driven flow is negligibly small compared with the shear-driven flow and pressure-driven flow.

3.5 Conclusions

To predict the state of plastron on longitudinal micro-trench SHPo surfaces in a high-speed flow of open water, which represents the conditions of a common watercraft in service, we have developed a unified theory by expanding the shear-driven drainage model for SHPo surfaces and combining it with the pressure-driven diffusion model. While the theory portrayed a linearly increasing air pressure, which usually translates to decreasing pressure difference between water

and air, along the trench in the downstream direction, deviations were anticipated at the front and rear ends of the trench due to the dynamic effect of flows. To evaluate the developed model, we have prepared micro-trench SHPo surfaces with combinatorial variations of nano-roughness, trench width, trench depth, and trench length, and tested them underneath a 13-foot motorboat in brackish water at a sea mouth to emulate field conditions. A unique observation technique using two underwater cameras was employed to differentiate the full and nearly-full plastron from the degraded plastron, not just from the no plastron surface. The experimental results corroborated the unified theory reasonably well, especially considering the uncertainties in the field tests. When the trench surfaces were coated with nano-grass, all the trenches tested were confirmed to have a full plastron except for some deteriorations on the longest trench (60 mm) made with a small depth. Reporting a unified model and robust SHPo surfaces, this work opens the door to designing SHPo surfaces geared toward field studies for drag reductions, anti-biofouling, anti-corrosion, etc.

References

1. J. Ou, B. Perot, and J.P. Rothstein, "Laminar drag reduction in microchannels using ultrahydrophobic surfaces", *Physics of Fluids*, 16, 4635-4643, 2004.

2. C.-H. Choi and C.-J. Kim, "Large slip of aqueous liquid flow over a nanoengineered superhydrophobic surface", *Physical Review Letters*, 96, 066001, 2006.

3. W. Barthlott and C. Neinhuis, "Purity of the sacred lotus, or escape from contamination in biological surfaces", *Planta*, 202, 1-8, 1997.

4. L. Cao, A.K. Jones, V.K. Sikka, J. Wu, and D. Gao, "Anti-icing superhydrophobic coatings", *Langmuir*, 25, 12444-12448, 2009.

5. A. Marmur, "Super-hydrophobicity fundamentals: implications to biofouling prevention", *Biofouling*, 22, 107-115, 2006.

6. T. Liu, Y. Yin, S. Chen, X. Chang, and S. Cheng, "Super-hydrophobic surfaces improve corrosion resistance of copper in seawater", *Electrochim. Acta*, 52, 3709-3713, 2007.

7. H. Park, C.-H. Choi, and C.-J. Kim, "Superhydrophobic drag reduction in turbulent flows: a critical review", *Experiments in Fluids*, 62, 1-29, 2021.

8. F. Brocher, "Reserches sur la respiration des insects aquatiques adultes–les haemonia.", *Ann Biol Lac*, 5, 5-26, 1912.

9. T. Min and J. Kim, "Effects of hydrophobic surface on skin-friction drag", *Physics of Fluids*, 16, L55-L58, 2004.

10. K. Fukagata, N. Kasagi, and P. Koumoutsakos, "A theoretical prediction of friction drag reduction in turbulent flow by superhydrophobic surfaces", *Physics of Fluids*, 18, 051703, 2006.

11. M.B. Martell, J.B. Perot, and J.P. Rothstein, "Direct numerical simulations of turbulent flows over superhydrophobic surfaces. ", *Journal of Fluid Mechanics*, 620, 31-41, 2009.

12. H. Park, H. Park, and J. Kim, "A numerical study of the effects of superhydrophobic surface on skin-friction drag in turbulent channel flow", *Physics of Fluids*, 25, 110815, 2013.

13. A. Rastegari and R. Akhavan, "On the mechanism of turbulent drag reduction with super-hydrophobic surfaces", *Journal of Fluid Mechanics*, 773, 2015.

14. H.J. Im and J.H. Lee, "Comparison of superhydrophobic drag reduction between turbulent pipe and channel flows", *Physics of Fluids*, 29, 095101, 2017.

15. R.J. Daniello, N.E. Waterhouse, and J.P. Rothstein, "Drag reduction in turbulent flows over superhydrophobic surfaces", *Physics of Fluids*, 21, 085103, 2009.

16. R.A. Bidkar, L. Leblanc, A.J. Kulkarni, V. Bahadur, S.L. Ceccio, and M. Perlin, "Skin-friction drag reduction in the turbulent regime using random-textured hydrophobic surfaces", *Physics of Fluids*, 26, 085108, 2014.

17. H. Park, G. Sun, and C.-J. Kim, "Superhydrophobic turbulent drag reduction as a function of surface grating parameters", *Journal of Fluid Mechanics*, 747, 722-734, 2014.

18. J.W. Gose, K. Golovin, M. Boban, J.M. Mabry, A. Tuteja, M. Perlin, and S.L. Ceccio, "Characterization of superhydrophobic surfaces for drag reduction in turbulent flow", *Journal of Fluid Mechanics*, 845, 560-580, 2018.

19. M. Xu, A. Grabowski, N. Yu, G. Kerezyte, J.-W. Lee, B.R. Pfeifer, and C.-J. Kim, "Superhydrophobic drag reduction for turbulent flows in open water", *Physical Review Applied*, 13, 034056, 2020.

20. M. Xu, N. Yu, J. Kim, and C.-J. Kim, "Superhydrophobic drag reduction in high-speed towing tank", *Journal of Fluid Mechanics*, 908, A6, 2021.

21. N. Yu, S. Kiani, M. Xu, and C.-J. Kim, "Brightness of Microtrench Superhydrophobic Surfaces and Visual Detection of Intermediate Wetting States", *Langmuir*, 37, 1206-1214, 2021.

22. M.S. Bobji, S.V. Kumar, A. Asthana, and R.N. Govardhan, "Underwater sustainability of the "Cassie" state of wetting", *Langmuir*, 25, 12120-12126, 2009.

23. R. Poetes, K. Holtzmann, K. Franze, and U. Steiner, "Metastable underwater superhydrophobicity", *Physical Review Letters*, 105, 166104, 2010.

24. M.A. Samaha, H. Vahedi Tafreshi, and M. Gad-el-Hak, "Sustainability of superhydrophobicity under pressure", *Physics of Fluids*, 24, 112103, 2012.

25. P. Lv, Y. Xue, Y. Shi, H. Lin, and H. Duan, "Metastable states and wetting transition of submerged superhydrophobic structures", *Physical Review Letters*, 112, 196101, 2014.

26. M. Xu, G. Sun, and C.-J. Kim, "Infinite lifetime of underwater superhydrophobic states", *Physical Review Letters*, 113, 136103, 2014.

27. H. Ling, J. Katz, M. Fu, and M. Hultmark, "Effect of Reynolds number and saturation level on gas diffusion in and out of a superhydrophobic surface", *Physical Review Fluids*, 2, 124005, 2017.

28. H. Kim and H. Park, "Diffusion characteristics of air pockets on hydrophobic surfaces in channel flow: Three-dimensional measurement of air-water interface", *Physical Review Fluids*, 4, 074001, 2019.

29. J.S. Wexler, I. Jacobi, and H.A. Stone, "Shear-driven failure of liquid-infused surfaces", *Physical Review Letters*, 114, 168301, 2015.

30. Y. Liu, J.S. Wexler, C. Schönecker, and H.A. Stone, "Effect of viscosity ratio on the shear-driven failure of liquid-infused surfaces", *Physical Review Fluids*, 1, 074003, 2016.

31. T.-S. Wong, S.H. Kang, S.K. Tang, E.J. Smythe, B.D. Hatton, A. Grinthal, and J. Aizenberg, "Bioinspired self-repairing slippery surfaces with pressure-stable omniphobicity", *Nature*, 477, 443-447, 2011.

32. J.R. Landel, F.J. Peaudecerf, F. Temprano-Coleto, F. Gibou, R.E. Goldstein, and P. Luzzatto-Fegiz, "A theory for the slip and drag of superhydrophobic surfaces with surfactant", *Journal of Fluid Mechanics*, 883, 2020.

33. C. Lee, C.-H. Choi, and C.-J. Kim, "Superhydrophobic drag reduction in laminar flows: a critical review", *Experiments in Fluids*, 57, 1-20, 2016.

34. C.-O. Ng and C. Wang, "Stokes shear flow over a grating: implications for superhydrophobic slip", *Physics of Fluids*, 21, 087105, 2009.

35. D.G. Crowdy, "Slip length formulas for longitudinal shear flow over a superhydrophobic grating with partially filled cavities", *Journal of Fluid Mechanics*, 925, 2021.

36. C.H. Mortimer, "The oxygen content of air-saturated fresh waters, and aids in calculating percentage saturation: With 2 tables and 5 figures in the text", *Internationale Vereinigung für Theoretische und Angewandte Limnologie: Mitteilungen*, 6, 1-20, 1956.

37. C. Schönecker, T. Baier, and S. Hardt, "Influence of the enclosed fluid on the flow over a microstructured surface in the Cassie state", *Journal of Fluid Mechanics*, 740, 168-195, 2014.

38. R. Sander, *Compilation of Henry's law constants for inorganic and organic species of potential importance in environmental chemistry*, Citeseer. 1999.

39. J. Seo, R. García-Mayoral, and A. Mani, "Pressure fluctuations and interfacial robustness in turbulent flows over superhydrophobic surfaces", *Journal of Fluid Mechanics*, 783, 448-473, 2015.

40. F.M. Menger and S.A. Rizvi, "Relationship between surface tension and surface coverage", *Langmuir*, 27, 13975-13977, 2011.

41. X. Zhang, L. Wang, and E. Levänen, "Superhydrophobic surfaces for the reduction of bacterial adhesion", *RSC Advances*, 3, 12003-12020, 2013.

42. B.V. Hokmabad and S. Ghaemi, "Effect of flow and particle-plastron collision on the longevity of superhydrophobicity", *Scientific reports*, 7, 1-10, 2017.

43. F.O. Ochanda, M.A. Samaha, H.V. Tafreshi, G.C. Tepper, and M. Gad-el-Hak, "Salinity effects on the degree of hydrophobicity and longevity for superhydrophobic fibrous coatings", *Journal of Applied Polymer Science*, 124, 5021-5026, 2012.

44. UCLA-TAMNS *Surface Shear Force Comparator*. Available: https://eps.tanms-erc.org/services/analytics-characterization-testing-modeling/DCJ2100900.

45. M. Xu, B. Arihara, H. Tong, N. Yu, Y. Ujiie, and C.-J. Kim, "A low-profile wall shear comparator to mount and test surface samples", *Experiments in Fluids*, 61, 1-13, 2020.

46. L. Piao and H. Park, "Two-dimensional analysis of air–water interface on superhydrophobic grooves under fluctuating water pressure", *Langmuir*, 31, 8022-8032, 2015.

47. Z. He, C. Maldarelli, and Z. Dagan, "The size of stagnant caps of bulk soluble surfactant on the interfaces of translating fluid droplets", *Journal of Colloid and Interface Science*, 146, 442-451, 1991.

48. S. Dukhin, V. Kovalchuk, G. Gochev, M. Lotfi, M. Krzan, K. Malysa, and R. Miller, "Dynamics of Rear Stagnant Cap formation at the surface of spherical bubbles rising in surfactant solutions at large Reynolds numbers under conditions of small Marangoni number and slow sorption kinetics", *Adv. Colloid Interface Sci.*, 222, 260-274, 2015.

49. E.L. Cussler and E.L. Cussler, *Diffusion: mass transfer in fluid systems*. 2009: Cambridge university press.

50. T. Enns, P. Scholander, and E. Bradstreet, "Effect of hydrostatic pressure on gases dissolved in water", *The Journal of Physical Chemistry A*, 69, 389-391, 1965.

51. H.M. Nagib, K.A. Chauhan, and P.A. Monkewitz, "Approach to an asymptotic state for zero pressure gradient turbulent boundary layers", *Philosophical Transactions of the Royal Society A: Mathematical, Physical and Engineering Sciences*, 365, 755-770, 2007.

52. F.M. White and J. Majdalani, *Viscous fluid flow*. Vol. 3. 2006: McGraw-Hill New York.

Chapter 4 Drag Reduction on Full-plastron Superhydrophobic Surfaces Underneath a Motorboat on the Natural Sea

4.1 Introduction

Superhydrophobic (SHPo) surfaces, which may capture a thin air layer (called plastron [1]) on them underwater, have been studied intensively since the 2000s, most notably due to their potential drag-reducing ability for water vessels [2-6]. However, despite many reports of successful drag reduction in both laminar and turbulent flows in laboratory settings [7, 8] and laminar flows on the open water [9-11], similar success in fully turbulent flows on the open water, which represents typical watercraft, has long been elusive until very recently [12]. Building on this earlier success and leveraging a couple of other advancements as discussed in Chapter 2 and 3, in this chapter, we expand the range of boat speed and improve the repeatability of experimental results significantly, leading to a clear and quantitative trend of how the drag reduction increases with the flow speed with a speedboat in a natural sea environment.

Drag reduction with SHPo surfaces was analytically predictable [13, 14] and experimentally verifiable [15] for laminar flows, but the same was not valid for turbulent flows. While numerical studies have consistently reported a successful drag reduction, which comes from the streamwise effective slip velocity on the air-water interface and mitigation of turbulent structures in the near-wall region [16-19], experimental results have long been inconsistent and controversial until the mid-2010s mainly because, looking back, the status of plastron was not known and unaccounted for. Consistent drag reduction has been observed when plastron was found to persist on the SHPo

surface [12, 20-24], while less drag reduction or even drag increase has been reported when the plastron was found to be depleted [25, 26]. For high-speed turbulent flows, until very recently, all the successful drag reduction experiments were conducted in closed water, such as the Taylor-Couette apparatus [24] and water tunnel [20], with the only experiment conducted in open water (done in towing tank) reporting a drag increase [25]. The first successful drag reduction with highly turbulent flows in open water was reported in 2020 by Xu [12] with a 4 m long motorboat on ocean water. Using a 4 cm × 7 cm sized SHPo surface with longitudinal microtrenches, about 30% (up to 40%) of drag reduction was reported with the boat speed up to ~10 knots (~5 m/s) or friction Reynolds number up to $Re_{\tau o}$ ~ 5800, where $Re_{\tau o} = \delta\sqrt{\tau_o/\rho}/\nu$, δ is the boundary layer thickness, τ_o is the wall shear stress of a smooth surface (i.e., no-slip surface), ρ is the density of water, and ν is the kinematic viscosity of water. Subsequently, similar SHPo surfaces were used to obtain up to about 25% of drag reduction in a high-speed towing tank with the flow speed ~5 m/s or $Re_{\tau o}$ ~ 3600 but drag reduction was hindered at higher speeds. While the plastron was observed at all speeds in the boat experiments [12], depletion of plastron was observed on portions of the sample surface at high speeds in the towing tank experiments of Xu [23] accompanied with deterioration of drag reduction.

Because of the plastron's central role in drag reduction, it is worth noting that the plastron can assume various statues on given surface asperities, as detailed in Park [8]. However, for this chapter, the discussion can be simplified to one of the microtrenches on a longitudinal trench SHPo surface, as shown in Figure 4-1. The air trapped in the trench is sheared by the flowing water and circulated, creating a pressure gradient along the trench. Following Chapter 3, which revised the shear-stress based oil drainage model by Liu [27] for SHPo surfaces, Figure 4-1 shows the states of plastron along the trench except for the excessive pinned-out state, where the air would merge

with that of the neighboring trenches and leave the surface as bubbles because it is not observed in high shear flows like the current experiment. The trench SHPo surfaces used in this chapter are designed to avoid the wetted and deteriorated plastron of Figures 1(b) and 1(c) so that the plastron is pinned at the trench top (i.e., Figures 1(d-f)) over the entire length of the trench. Note that the depinned-in state with only slight depinning, chosen to be $h/w < 0.13$ in this chapter, is considered a pinned state. The effect of h/w on drag reduction will be reviewed in the next section.

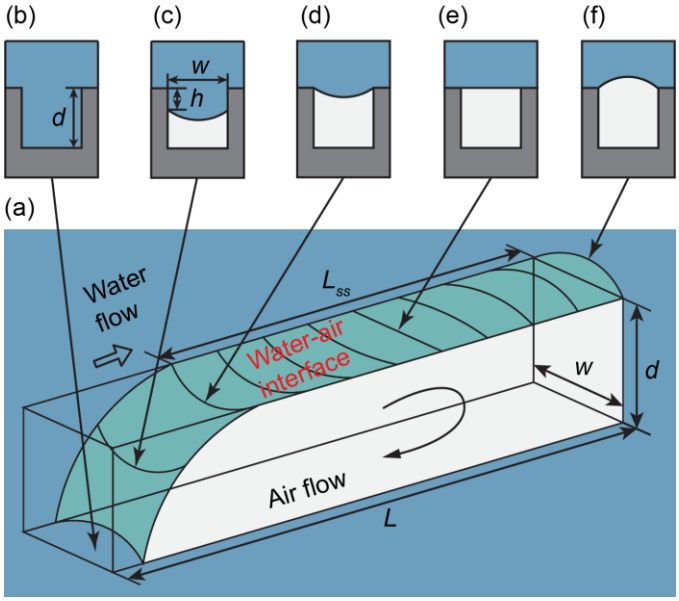

Figure 4-1. The plastron states in a hydrophobic trench illustrated to represent a trench SHPo surface moving longitudinally underwater. (a) If the trench is longer than the steady-state plastron length, i.e., $L > L_{ss}$, the trench would be wetted over the extra length at the leading end. Cross-sectional views of the plastron at several locations along the trench are shown in (b-f). (b) Fully wetted state with no plastron. (c) Depinned-in state, i.e., the interface inside the trench, with intrusion depth h. (d) Pinned-in state, i.e., the interface pinned and deformed inwardly. (e) Pinned-flat state, i.e., the interface pinned and flat. (f) Pinned-out state, i.e., the interface pinned and deformed outwardly. The trench SHPo surfaces used in this chapter is designed to maintain a

pinned state, i.e., (d-f), over the entire trench length, thus called full-plastron SHPo surfaces, throughout the drag reduction experiments.

For field tests to find a drag-reducing trend with SHPo surfaces over a range of flow speeds, one would need SHPo surfaces that maintain a full plastron for most of the flow conditions in the field. Such a high-performance SHPo surface was developed and confirmed to maintain a full plastron under the motorboat even at high speeds (up to 14 knots or ~7 m/s) as explained in Chapter 3. The development required: a unified theory to predict the maximum trench length that can maintain a full plastron; a new microfabrication method to make microtrenches with hierarchical roughness; and the use of a field-compatible observation method devised by Chapter 2, which can differentiate full plastrons from deteriorated and depleted plastrons. Following the same microfabrication method in Chapter 3, we design longitudinal trench SHPo surfaces with geometrical parameters that would allow the full plastron under up to the maximum shear rate (~69000 s^{-1}) imposed by the boat. Trench SHPo surfaces with different slip lengths are fabricated and tested to study the drag reduction in open water turbulent flows free of the deteriorated plastron. Empowered by the high-performance SHPo surfaces that can maintain a full plastron and the observation method that can confirm full plastron, we study the drag-reducing trend of full-plastron SHPo surfaces underneath a motorboat on a natural sea environment. By improving the boat and test procedures, which led to more reliable drag ratio data over a wider range of boat speeds than before (i.e., by Xu [12]), we obtain a clear trend of drag ratio vs. nondimensional slip length of the SHPo surfaces. While our main interest is in the drag reduction on longitudinal trench SHPo surfaces, transverse trench and post SHPo surfaces are also tested to see the effect of transverse slip on drag reduction in the same flows. They are designed to have the same longitudinal slip length as the longitudinal trenches.

4.2 The Slip Length for Drag Reduction

The amount of slip on a surface is quantified as a slip length, which is the virtual distance into the wall where the extrapolated flow velocity vanishes to zero, expressed as $\lambda = u_s/(\partial u/\partial y)|_{wall}$ where u_s is the slip velocity on the wall. For laminar flows, drag reduction can be calculated from the slip length, which is unique for a given SHPo surface, and the flow geometry imposed by a given flow system, such as Couette flow [6]. In turbulent flows, on the other hand, drag reduction required numerical analysis for the asperities of a given SHPo surface and the given flow geometry by a given flow system [16-19]. Note the drag reduction in turbulent flows is affected by the turbulent structures. While drag is affected (reduced) only by the longitudinal slip in laminar flows, it is affected (increased) by the transverse slip as well in turbulent flows because the spanwise slip aggravates the turbulence [16, 28]. Despite the lack of direct relationship with the drag reduction in turbulent flows, the slip length of a slip surface is still the best indication to predict its drag-reducing ability, as a large longitudinal slip length would lead to a large drag reduction.

The slip lengths of SHPo surfaces with a regularly patterned roughness, including longitudinal trenches that tend to provide the largest drag reduction, have been analytically derived. For modeling, SHPo surfaces are usually assumed to have water-air interfaces that are flat, shear-free, and pinned at the top edges of surface asperities. Furthermore, for trench SHPo surfaces, the trenches are considered infinitely long with no ends. It was theoretically derived [13, 29] and experimentally proven [15] that the slip length on the SHPo surface with longitudinal trenches (LT) is

$$\lambda_{LT} = -\frac{p}{\pi}\ln\left(\frac{\pi\phi_g}{2}\right) \tag{4-1}$$

where p is the periodic length of the trenches and ϕ_g is the gas fraction, i.e., the fraction of the shear-free (i.e., infinite slip) interface, and that with the transverse trench (TT) is

$$\lambda_{TT} = -\frac{p}{2\pi}\ln\left(\frac{\pi\phi_g}{2}\right) \tag{4-2}$$

Also, it was theoretically derived [30] and experimentally obtained [7] that the slip length on the SHPo surfaces with aligned posts (AP) in a square pattern is:

$$\lambda_{AP} = \left[\frac{3}{16}\sqrt{\frac{\pi}{1-\phi_g}} - \frac{3}{2\pi}\ln\left(1+\sqrt{2}\right)\right]p \tag{4-3}$$

However, in reality, the interfaces are not flat and not shear free, not to mention that the trenches must have a finite length for most applications. To address the deviation from the shear-free interface, Belyaev [31] derived the slip length of trench SHPo surfaces with non-zero shear stress, which is caused by the viscosity of the air circulating inside the trench, as

$$\lambda_{LT,\nu} = -\frac{p\ln\left[\cos\left(\pi\phi_g/2\right)\right]}{\pi + \frac{p}{\tilde{\lambda}_{LT}}\ln\left[\frac{1+\sin\left(\pi\phi_g/2\right)}{\cos(\pi\phi_g/2)}\right]} \tag{4-4}$$

$$\lambda_{TT,\nu} = -\frac{p\ln\left[\cos\left(\pi\phi_g/2\right)\right]}{2\pi + \frac{p}{\tilde{\lambda}_{TT}}\ln\left[\frac{1+\sin\left(\pi\phi_g/2\right)}{\cos(\pi\phi_g/2)}\right]} \tag{4-5}$$

where $\tilde{\lambda}_{LT}$ and $\tilde{\lambda}_{TT}$ are the constant local slip lengths for longitudinal trenches and transverse trenches, respectively. Chang [32] derived these local slip lengths explicitly by assuming an elliptic slip-length profile and nearly constant shear rate on the interface as

$$\tilde{\lambda}_{LT,\nu} = \frac{1.12}{\pi}\mu_R w \tanh\left(\pi d/w\right) \tag{4-6}$$

$$\tilde{\lambda}_{TT,\nu} = \frac{0.342}{\pi}\mu_R w \tanh\left(\pi d/w\right) \tag{4-7}$$

where μ_R is the water-to-air ratio of dynamic viscosities, $\mu_R = \mu_{water}/\mu_{air}$, w is the width of the trench, and d is the depth of the trench. However, the slip length on the surface with the aligned post with a non-zero shear at the interface has not been reported yet, to the best of our knowledge. We will use Equations (4-1), (4-2), and (4-3) for simplicity when designing all the SHPo surfaces with a target slip length but will use Equations (4-4) to (4-7) when analyzing the experimental data of the LT and TT surfaces.

Next, let us review how deviations from the flat and pinned interfaces affect the slip length. For the deviation from the assumption of a flat interface, on LT surfaces with pinned interfaces, the slip lengths on inwardly and outwardly deformed interfaces (Figure 4-1(d) and Figure 4-1(f), respectively) were found to be similar to that of the flat interfaces (Figure 4-1) [33-35], leading us to treat the curvature of the interface as a secondary influence to drag reduction. However, for the deviation from the assumption of the pinned interface, depinning was found to have a significantly negative effect. On LT surfaces with flat interfaces, the slip length decreased by ~50% when the depinning was h/w = 0.1, by ~70% when h/w = 0.2, and to zero or even a negative value when fully wetted [36, 37]. Accordingly, it is essential to detect when the plastron has deteriorated non-negligibly (i.e., depinned more than slightly) for successful drag reduction research. Despite the importance of maintaining a full plastron for successful drag reduction, not many studies in the literature even confirmed the existence of plastron throughout the flow experiments, explaining why there have been so many inconsistencies and confusion among the experimental results of

SHPo drag reduction in turbulent flows. To make things worse, the widely popular practice of confirming the plastron by the brightness (i.e., the silvery sheen appearance), while reliable to detect the loss of plastron (by the dark appearance), may miss the deterioration of plastron even when the deterioration is severe enough to negate the drag reduction altogether (e.g., $h/w > 0.5$), as proven by Chapter 2. This previously unknown possibility of mistakenly taking a deteriorated plastron for a full plastron, possibly including our previous boat experiment [12], is one of the main motivations for the current study.

4.3 Experiments and Methods

4.3.1 Design and Fabrication of SHPo Surfaces

To have a non-negligible drag reduction, the slip length of the SHPo surface should be comparable to the viscous sublayer thickness of turbulent flows [8]. Considering the sublayer thickness for a wide range of watercraft in motion is around 50 μm, we designed longitudinal trenches (LT) SHPo surfaces with pitches p = 50 μm, 75 μm, and 100 μm and widths w = 45 μm, 67.5 μm, and 90 μm, respectively, which result in a constant gas fraction $\phi_g = w/p = 0.9$, resulting in the nominal longitudinal slip length of λ = 29.5 μm, 44.3 μm, 59.0 μm, respectively, according to Equation (4-1). The depths of trenches, d, were set to be the same as the trench width, w, to achieve an aspect ratio $w/d = 1$. Based on the maximum trench length for full plastron LT estimated by Chapter 3, we used trenches not longer than 2 cm, which is estimated to be short enough to avoid shear-induced drainage with sufficient safety margin to counter the uncertainties of boat experiment on the sea. The surface is expected to maintain a full plastron, but the status of the plastron is monitored throughout each test. Our design for the LT surface was the 7 cm long sample divided into 4 trenches of 1 cm + 2 cm + 2cm + 2cm, as shown in Figure 4-2(a). The overall size of the

sample (4 cm × 7 cm) was limited by the 100 mm diameter silicon wafer the sample is made from. The first trench at the leading region was chosen to be 1 cm (shorter than the others) to make it more robust against wetting, considering the abrupt change from the smooth surrounding surface to the slippery SHPo surface as well as the horizontal gap (50–100 μm) and a potential vertical step (< 15 μm) between them.

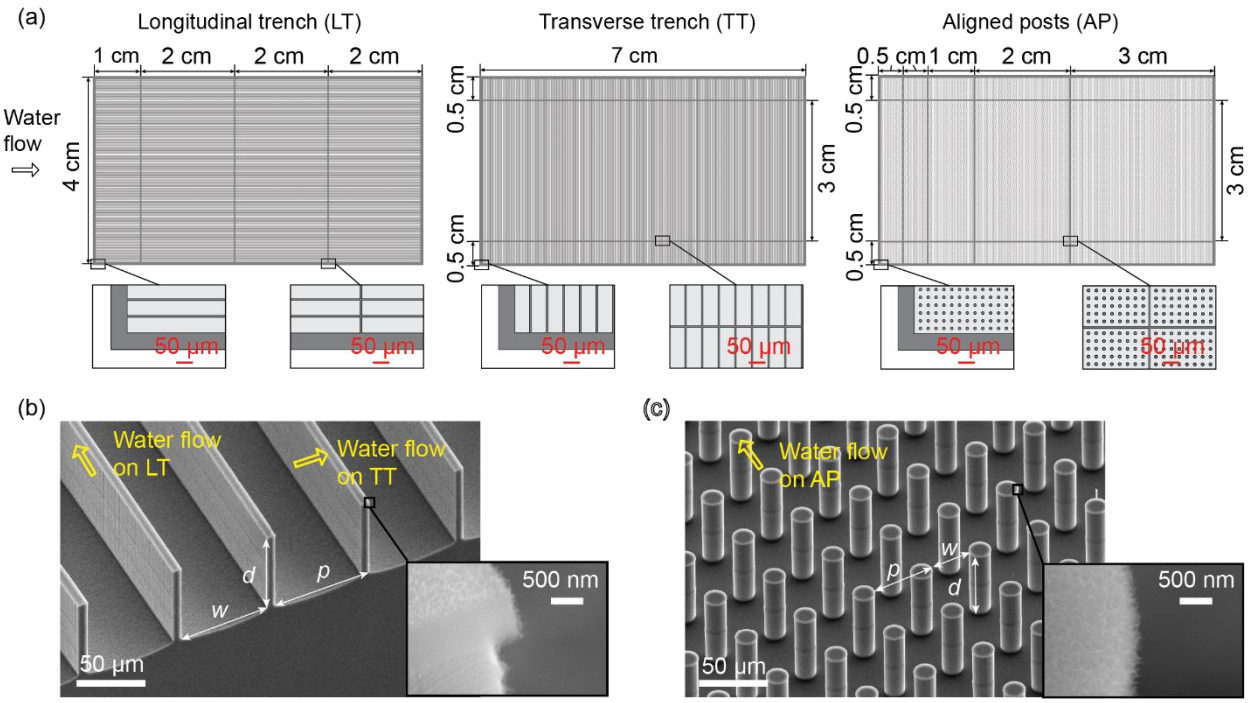

Figure 4-2. Schematics and pictures of the 4 cm × 7 cm SHPo surface samples. (a) Arrangement of microstructures on the samples. Left: longitudinal trenches (LT). Middle: transverse trenches (TT). Right: aligned posts (AP). The zoomed-in figures at corresponding locations drew the structures to scale. (b) SEM pictures of a cleaved trench sample. Yellow arrows indicate the water flow directions on longitudinal trenches and transverse trenches. The inset SEM picture shows the microstructures are covered with Al_2O_3 nano-grass and reveals the cross-section view of the re-entrant shape at the top edge of the trench. (c) SEM pictures of an aligned post sample. The pitch *p*, space width *w*, and depth *d* of posts are labeled. The inset SEM picture shows that the

microstructures are covered with Al_2O_3 nano-grass. However, the re-entrant top edge is not revealed in this non-cross-sectional picture.

To further study the effect of structure types on the drag-reducing ability, we designed two other patterns of SHPo surface: transverse trenches (TT) and aligned posts (AP), as schematically drawn in Figure 4-2(a). For a fair comparison with the LT sample of p = 50 μm, the TT and AP samples were designed to have the same gas fraction (i.e., ϕ_g = 0.9) and the same longitudinal slip length (λ = 29.5 μm) based on Equations (4-1), (4-2), and (4-3) for simplicity, as shown in Table 1. The depth of TT was set to be d = 90 μm to maintain the same trench aspect ratio as LT. The depth of AP was set to be d = 50 μm to alleviate the shear-induced wetting, to which the AP is expected to be more susceptible than LT. For the 3 LT types studied, 2 samples have been fabricated and tested for each type, while for the TT and AP types, 1 sample has been fabricated and tested for each type. All the SHPo surfaces were prepared using micro-electro-mechanical-systems (MEMS) fabrication technology, as described in Chapter 3, and involving standard photolithography, reactive ion etching (RIE), deep reactive ion etching (DRIE), atomic layer deposition (ALD), and self-assembled monolayer (SAM) coating of 1H,1H,2H,2H-perfluorodecyltrichlorosilane (FDTS). All the microstructures have the re-entrant edges on top and their surfaces covered with nano grass, as shown in the inset SEM pictures of Figure 4-2(b,c).

Table 4-1. The types and names of SHPo surfaces with their geometric parameters. The slip lengths are from the analytical equations, which assume shear free interface for comparison. The slip lengths of the surface in both streamwise and spanwise directions are listed.

Sample name	Sample type	Pitch, p (μm)	Gas fraction, ϕ_g	Depth, d (μm)	Streamwise slip length, λ (μm)	Spanwise slip length, λ (μm)
LT_p100	Longitudinal trenches	100.0	0.9	90	59.0	29.5
LT_p75		75.0	0.9	67.5	44.3	22.2
LT_p50		50.0	0.9	45	29.5	14.8
TT_p100	Transverse trenches	100.0	0.9	90	29.5	59.0
AP_p47	Aligned posts	46.9	0.9	50	29.5	29.5

4.3.2 Low Profile Shear Stress Comparator

A house-developed shear, shown in Figure 4-3, was used to measure the drag ratio of each SHPo surface, where the drag ratio is defined as the ratio of the shear stress on the SHPo surface, τ, to that on the smooth surface, τ_o. A SHPo surface was placed next to a smooth surface of the same size diced out from a silicon wafer during each flow test. Each surface was attached to its own floating element on the shear comparator, whose displacement is proportional to the shear force

on the surface attached to it. The floating elements were monolithically machined from a titanium plate, and their natural resonant frequency was designed not to affect the measurement. The flexure beams of the floating elements have a high-aspect-ratio cross-section so that they are flexible only in the streamwise direction and rigid in all other directions. Two optical interference encoders (M2000 linear encoder, Celera Motion Inc.), one for each floating element, were sealed in a waterproof encoder plate with silicone for underwater usage and used to measure the displacement of the floating elements with 78 nm spatial resolution and 512 Hz sampling frequency. To minimize disturbing the flows past the sample surface, the sample was placed so that its surface was flush with the surface of the surrounding cover sheet. The provision developed before [12, 23, 38] was further refined to maintain the step height and the frontal horizontal gap between the sample and the cover sheet below 15 μm and about 100 μm, respectively. The displacements of the two surfaces were simultaneously measured by the two optical encoders and recorded by a computer. While this sensor is used as a shear stress comparator most times, when desired, the shear stress on each sample can be calculated based on the spring constant of the flexure beams and the sample surface area. The measurement uncertainties were less than 10% of the measured values [38]. The shear stress comparator was proven to work in field conditions, such as under a boat [12], on a wind tunnel [38], and for a towing tank [23]. The low profile configuration (1.8 cm thick) makes the sensor versatile by allowing it to fit in a small space, even on a towing plate [23].

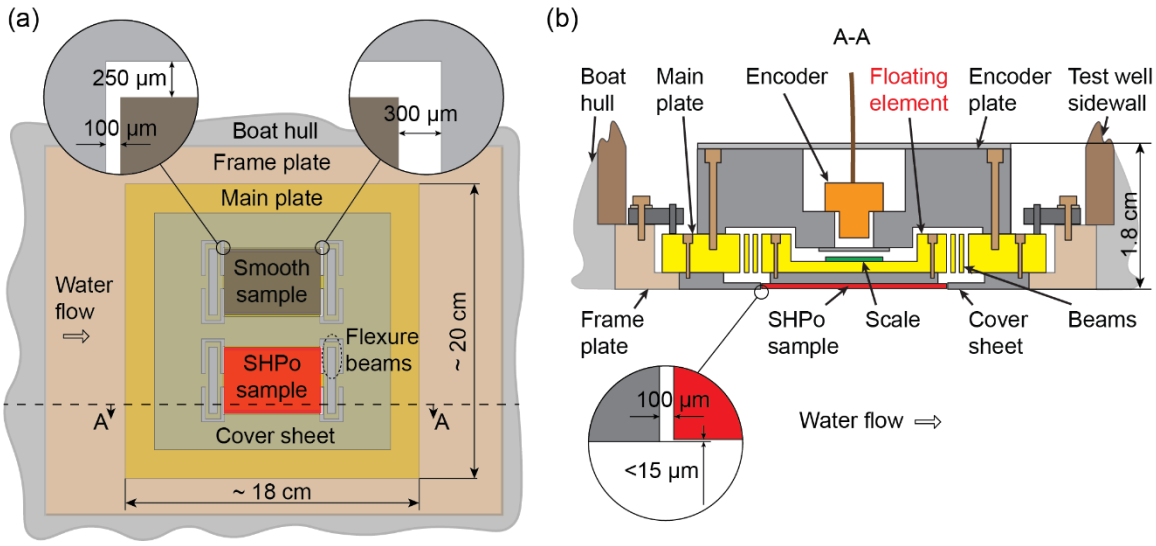

Figure 4-3. Shear stress comparator (UCLA-TAMNS) installed under the boat.Schematic top view. One smooth silicon sample and one SHPo sample are attached to the two floating elements in the main plate made of titanium. (b) Schematic cross-section view. For each test run, the main plate with a new sample is fastened to the frame plate, which stays affixed to the frame plate fixed to the test well, and the height gaps between the sample and the surrounding cover sheet are adjusted to be within 15 µm. Adapted from [38], the figures are not drawn to scale for clarity.

4.3.3 Motorboat and Underwater Camera System

The 4 m long motorboat retrofitted for the drag reduction experiments by Xu [12] has been revamped, as shown in Figure 4-4, to increase the maximum boat speed from ~10 knots to ~14 knots. A hydrofoil (Doel-Fin Hydrofoil, Davis Instruments) was installed on the outboard motor (Honda Marine 20 HP) to reduce the bow rise while speeding up and improve the boat's balance performance, leading to higher speeds and a smoother ride. The boat speed, *U*, was measured by a paddlewheel speedometer (D800 Thru-Hull Smart Multisensor Transducer, Raymarine) installed below the boat transom and connected to a display instrument (i40 Speed Instrument Display,

Raymarine). The trim (tilt) angle of the boat, α, was measured by an inclinometer (H4A1-45 Inclinometer, RIEKER) fixed in the boat during the drag ratio measurement. Both the boat speed and trim angle were monitored as a function of time and recorded by the computer. The shear stress comparator was installed at the bottom hull of the boat and used to measure drag ratios (or shear stress when desired) at various boat speeds. For each test, the boat would stay stationary for 5 seconds initially, accelerate to reach a target speed in 5 seconds, and maintain the target speed for 40 seconds before the shear stresses on the two surfaces were measured simultaneously and recorded. The wetting length, $\hat{x}$, which is the streamwise distance from the leading edge of the immersed hull to the center of sample, was measured with a ruler attached on the side of the hull.

Following Yu [39], the immersed SHPo surface was monitored by a system of two underwater cameras, as shown in Figure 4-4, to assure the sample had a full plastron on its entire surface. For LT surfaces, a departure from full plastron could be detected by the side camera. We set the elevation angle of the side camera to $\beta_e = 8\pm2°$, which would detect the depinned when $h/w > 0.13\pm0.3$. For TT surfaces, a departure from full plastron could be detected by the rear camera, which was set to have the same elevation angle as the side camera, therefore detecting $h/w > 0.13\pm0.3$ on the TT surface. For AP surfaces, although their brightness with different observation angles has not been systematically studied, the depinning of the plastron could lead to a slightly darker appearance due to the loss of the total internal reflection (TIR) region on the plastron.

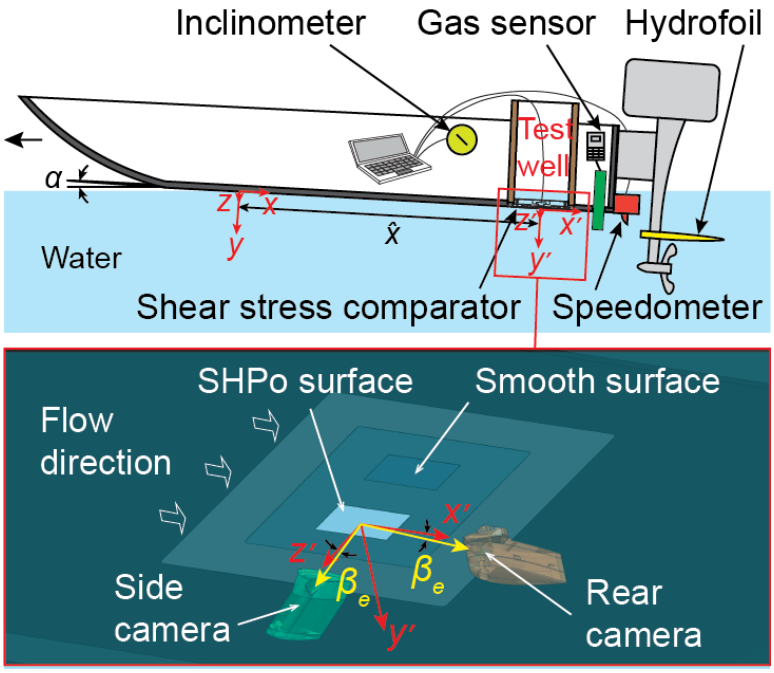

Figure 4-4. Revamped boat installed with various instruments to monitor the flow conditions and underwater camera system. The black arrow labels the boat traveling direction. The origin of the *xyz* coordinate is the starting point of the hull in contact with water. The origin of the *x'y'z'* coordinate is the center point of the SHPo sample. Looking up from below in the water, the inset figure shows the shear comparator installed underneath the boat and the two underwater cameras, observing the sample surface in the directions of the yellow arrows, forming an elevation angle, β_e.

4.3.4 Field Test Conditions

All the tests have been performed in the ocean area of Santa Monica Bay near Los Angeles, California, ~20 miles from the land. Testing times on different days were chosen so that the tide and wind conditions were similar for all the test runs. The wave heights and periods were 1–1.5 feet and 13±3 seconds, respectively, according to the online forecast website [40]. For each test, the boat was driven against the wave direction to avoid the effect of transverse flow on the sample.

The weight distribution on the boat was carefully controlled to maintain similar flow conditions, including the wetting length and trim angle, for tests on different days. The air saturation level in the ocean water was monitored periodically by a total gas sensor (Point Four^{TM} tracker, PENTAIR) and measured to be 104–109% for all the tests. Unlike the 99–101% found in the water at the mouth of the creek to the ocean, which was chosen to study the plastron status in Chapter 3, this supersaturated water helped sustain the full plastron. The seawater temperature was measured to be constant during the test on a given day and 20±5°C over the period of our experiments (6? months). The salinity of the ocean water was measured to be 35±1 g/kg using a salinity refractometer (Xin Da Cheng), and the surface tension was measured to be 73.46±0.24 mN/m using a tensiometer (K100, Krüss). These values are comparable to the properties reported by Nayar [42], where the ocean water had a salinity of 35.28 g/kg and surface tension of 73.477 mN/m. Although natural seawater likely contains multiple types of surfactants, the measured surface tension is comparable to that of water containing sodium dodecyl sulfate (SDS) at a concentration of less than 10^{-3} mM [43].

4.4 Results and Discussions

A total of 8 SHPo surface samples (i.e., 2 samples each of 3 LT types, 1 TT sample, and 1 AP sample, as listed in Table 1) have been fabricated and tested under the boat with speeds varying from ~ 2.5 m/s to ~7.5 m/s with ~0.5 m/s increments. For each SHPo sample, the drag ratio between the SHPo and smooth surface was measured at ~9 different boat speeds. In addition, smooth surface samples were used to calibrate the drag measurements and to assess the effect of boat trim angle.

4.4.1 Calibration with Smooth Surfaces

The derivation of the empirical equations in this subsection has been performed by Mr. Francisco del Campo Melchor.

To assess the reliability of the shear comparator for the current drag reduction experiment, we placed two smooth silicon surfaces, which were diced from two silicon wafers, on the two floating elements of the shear comparator and tested their shear stresses with increasing boat speeds. As shown in Figure 4-5(a), the shear stresses measured on the two floating plates were similar with less than a 5% difference, indicating the flow conditions on the two floating elements were similar during the flow tests. In addition, the shear stress values from the empirical equations are also plotted for comparison further to support the shear comparator for the current study.

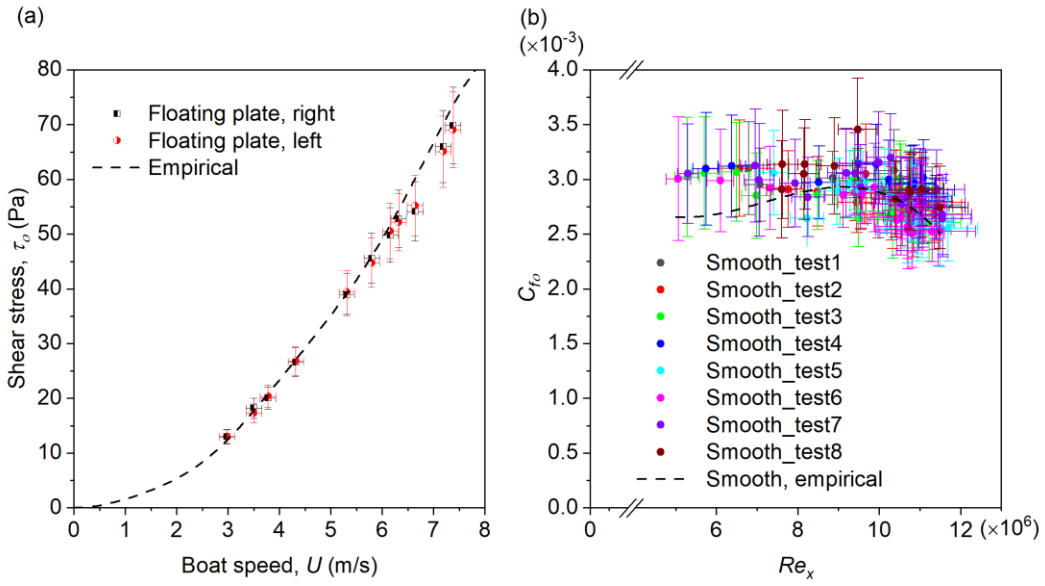

Figure 4-5. Measurement results with smooth surfaces. (a) The friction coefficients of two smooth surfaces attached to two floating elements of the shear comparator and subjected to different boat speeds. The nearly identical shear stress values measured from the two floating elements as well

as the similar empirical curve at various boat speeds show the reliability of the sensor and also confirm the two surfaces experience the same flow condition. (b) The friction coefficient of a smooth surface attached to one floating element of the shear comparator and subjected to different Reynolds numbers. The results were obtained on smooth surface while performing drag reduction tests for the 8 SHPo samples which was attached to the other floating element in the shear comparator.

The friction coefficient on the smooth surface was obtained during each drag reduction test with all 8 SHPo samples, as collected in Figure 4-5(b), to assess the effect of trim angle on the friction drag, which is our interest. Because the trim angle is non-zero when the boat travels (it planes) for the tests, there exists a pressure gradient under the bottom of the boat, and the hydrodynamic pressure varies along the bottom surface. To establish the reference values of the shear stress under the boat, we estimate the empirical skin friction coefficient on the smooth surface. The boat, a 4 m Boston Whaler, is assumed to have a simplified outline with a V-shape hull, as shown in Figure 4-6. The total wetting length of the boat is L_b, which is the distance between the leading edge of the immersed hull and the boat transom, and the boat's width is W_b. Since the sample is placed 55 cm upstream of the transom in the current boat configuration, we have $L_b = \hat{x} + 55$ cm. The displacement thickness, δ^*, and the momentum thickness, θ, are assumed to be [45]:

$$\frac{\delta^*}{x} = \frac{0.048}{\mathrm{Re}_x^{1/5}} \tag{4-8}$$

$$\frac{\theta}{x} = \frac{0.037}{\mathrm{Re}_x^{1/5}} \tag{4-9}$$

where Reynold number is defined as $Re_x = \rho U x/\mu_{water}$, ρ is the density of water, x is the immersed length with respect to the starting point of the immersed hull. Based on the Karman momentum

integral equation, the skin friction coefficient in the turbulent boundary layer with the velocity gradient outside the boundary layer is

$$\frac{C_{fo}(x)}{2} = \frac{d\theta}{dx} + \left(2 + \frac{\delta^*}{\theta}\right)\frac{\theta}{U}\frac{dU}{dx} \tag{4-10}$$

The velocity gradient and pressure gradient can be related using the Euler equation since it holds at the edge of the boundary layer:

$$\frac{dP}{dx} + \rho U \frac{dU}{dx} = 0 \tag{4-11}$$

By introducing the Euler equation into the Karman momentum integral equation, Equation (4-10) becomes

$$C_{fo}(x) = 2\frac{d\theta}{dx} - \left(2 + \frac{\delta^*}{\theta}\right)\frac{\theta}{\frac{1}{2}\rho U^2}\frac{dP_{hd}(x)}{dx} \tag{4-12}$$

where dP_{hd}/dx is the local gradient of hydrodynamic pressure.Inputting Equations (4-8) and (4-9) into Equation (4-12), we can get:

$$C_{fo}(x) = \frac{0.059}{\mathrm{Re}_x^{1/5}} - \frac{0.244x}{\rho U^2 \mathrm{Re}_x^{1/5}}\frac{dP_{hd}(x)}{dx} \tag{4-13}$$

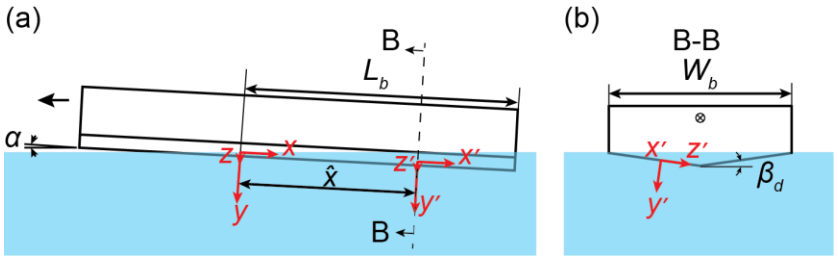

Figure 4-6. Illustration of the flow condition under a simplified boat shape. (a) Side view of the boat. The total wetting length of the boat under the water is L_b. The wetting length at the sample location is $\hat{x}$. The trim angle is α. The origin of the *xyz* coordinate is the leading edge of the immersed hull. The origin of *x'y'z'* coordinate is the center of the sample. The dashed line shows the cross-section position B-B. The single black arrow indicates the boat traveling direction. (b) The cross-section view of the boat. The simplified boat has a symmetric V-shape hull with a deadrise angle β_d.

To estimate the hydrodynamic pressure gradient on the sample, we assume that the leading edge of the immersed hull has the maximum hydrodynamic pressure, P_{max}, which can be approximated as [44]

$$P_{\max} = \frac{q\pi^2 \tan^2(\alpha)}{\pi^2 \tan^2(\alpha) + 4\tan^2(\beta_d)} \tag{4-14}$$

where β_d is the deadrise angle of the boat hull, which was measured to be $\beta_d = 8°$, and $q = \rho U^2/2$. Starting from its maximum value at $x = 0$, the hydrodynamic pressure, P_{hd}, decreases in the streamwise direction until it becomes zero at the boat's transom. The hydrodynamic pressure profile has two segments, which can be expressed as [44]

$$P_{hd}(x) = \frac{0.006\alpha^{1.3} X^{1/3} q}{X + \frac{\left(0.006\alpha^{1.3}\right)^{1.5}}{2.588\left(P_{\max}/q\right)^{1.5}}}, \text{ if } 0 \le x \le L_b - 0.5W_b \tag{4-15}$$

$$P_{hd}(x) = \frac{0.006\alpha^{1.3} X^{1/3} q}{X + \frac{\left(0.006\alpha^{1.3}\right)^{1.5}}{2.588\left(P_{\max}/q\right)^{1.5}}} \frac{\left(\Gamma - X\right)^{1.4}}{\left(\Gamma - X\right)^{1.4} + 0.05}, \text{ if } L_b - 0.5W_b \le x \le L_b \tag{4-16}$$

where $X = x/W_b$ and $\Gamma = L_b/W_b$. The trim angles and wetting lengths at various speeds of ~60 tests are plotted in Figure 4-7. The data from ~60 tests (i.e., boat speed U, trim angle α, and wetting length L_b) are firstly utilized to get the hydrodynamic pressure gradient $dP_{hd}(\hat{x})/dx$ on the smooth sample for each test by inputting the values from Figure 4-7 to Equations (4-14) to (4-16), then the empirical value of the skin friction coefficient of the smooth surface of each test is derived by inputting Re_x at sample location $x = \hat{x}$ and $dP_{hd}(\hat{x})/dx$ into Equation (4-13). Due to the variation of the measured parameters, for simplicity, a 3rd order polynomial fitting line of the ~60 data points of empirical values of C_{fo} of different Re_x was used in Figure 4-5(b) to be compared with the measured skin friction coefficient of the smooth surface.

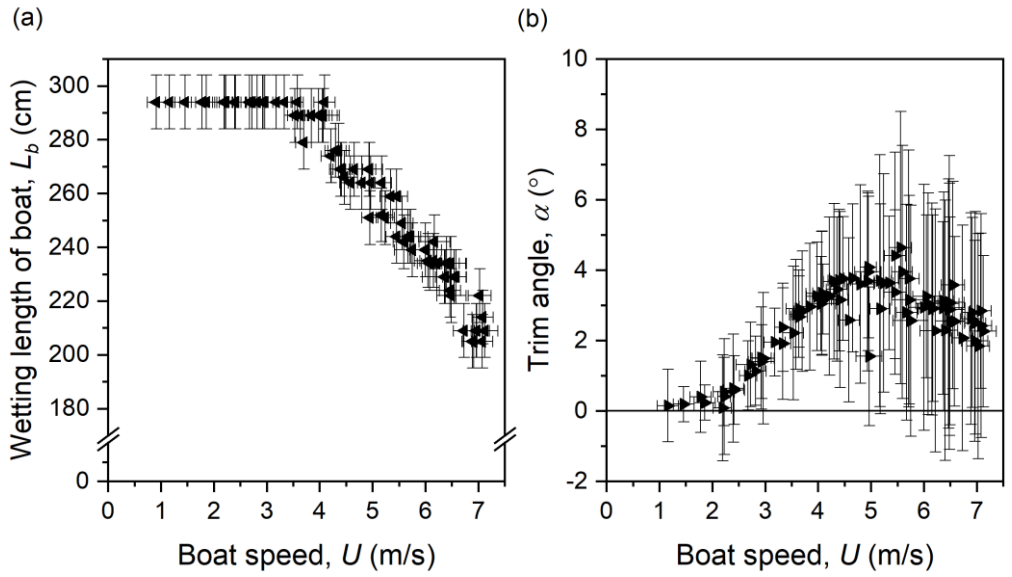

Figure 4-7. Parameters of the boat at various speeds. (a) Wetting length of the boat. The vertical uncertainties are estimated as random errors in wetting length measurement. The horizontal uncertainties come from the standard deviation of the measured boat's speed. (b) Trim angle of the boat. The vertical and horizontal uncertainties come from the standard deviations of the measured boat's trim angle and speed.

The empirical line in Figure 4-5(b) shows that the skin friction coefficient increases with Re_x up to 9×10^6 (boat speed 4 – 5 m/s) and then decreases with Re_x, which is similar to the measured data. The increasing skin friction coefficient is caused by the increasing hydrodynamic pressure gradient when the boat trim angle increases with the boat speed. As the boat speed becomes higher than ~5 m/s, the boat starts planing, and the trim angle starts decreasing with the boat's speed, which leads to decreasing skin friction coefficient. Considering the varying field conditions in the ocean, the measured data fit the empirical line reasonably well with $Re_x > \sim8\times10^6$ (i.e., $U >$ ~3.5 m/s). The discrepancy between empirical and experimental values at boat speeds lower than 3.5 m/s could come from the different velocity profiles in turbulent boundary layer at lower boat speeds; however,

the data in such a range is trivial due to the effect of merged air bubbles on SHPo surfaces as discussed in the next section.

4.4.2 Full Plastron Monitored by Images

Two miniature underwater cameras monitored all the surfaces during the boat tests to ensure the entire sample had full plastron. For each surface type, 7 exemplary pairs of images taken at 7 different boat speeds are shown in Figure 4-8 through Figure 4-10. For the characterization of the flow condition, the boat speed and the friction Reynolds number on the smooth surface $Re_{\tau o}$ of each test are also shown next to the image pairs. For estimating $Re_{\tau o}$, the boundary layer thickness δ is estimated by $\delta/x = 0.38/Re_x^{1/5}$ [45].

Figure 4-8 to Figure 4-10 were taken with one of the two samples of LT_p100, LT_p75, and LT_p50. On the LT samples, at low speeds (< 4.5 m/s), bubbles were found to persist on the surface along the rear end of the sample, as indicated by the yellow boxes in the top pictures of Figure 4-8 to Figure 4-10, possibly due to the high air concentration level in the surrounding water, creating own form drag that hinders the intended measurement, but these bubbles were sheared away when the boat sped up. When the boat was faster than ~4.5 m/s, all the LT samples (i.e., LT_P75, LT_P50, and LT_p100) maintained a full plastron on the entire surface, as shown in Figure 4-8 to Figure 4-10, except one of the two LT_p100 samples. For this one exception, which is indicated by the red boxes in the bottom pictures of Figure 4-8, depinning (i.e., $h/w > 0.13$) was found at the leading end of trenches at the highest boat speed (~7.3 m/s) but only in the first and the shortest of the 4 segmented trenches, indicating it may have been caused by the horizontal gap and vertical step in front of the sample. The sample also had depinning-in (albeit over a limited length) at the rear ends of each of the 4 segmented trenches when the boat was faster than 7.1 m/s, for which we speculate

hydrodynamic pressure due to the trim angle, stagnant pressure at rear ends of trenches, and even the decreased surface tension by the surfactant accumulated at the rear ends of trenches as potential culprits. Since this depinning was found for only one of the two LT_p100 samples tested on different days, the culprit could have been an unusual environmental condition on a particular day or just a low-quality sample. Figure 4-11 andFigure 4-12 were taken with one sample of TT_p100 and AP_P47, respectively. The bubbles were also observed at low speed for the TT and AP samples, as indicated by the yellow boxes in the top pictures, while depinning-in was found at boat speeds higher than ~6 m/s. Only the surfaces with a full plastron were used for the drag ratio measurement. The samples with bubbles or deteriorated plastrons were excluded from the measurement to avoid the form drag by the bubbles or the decreased slip by the depinned plastron affecting the drag reduction measurement.

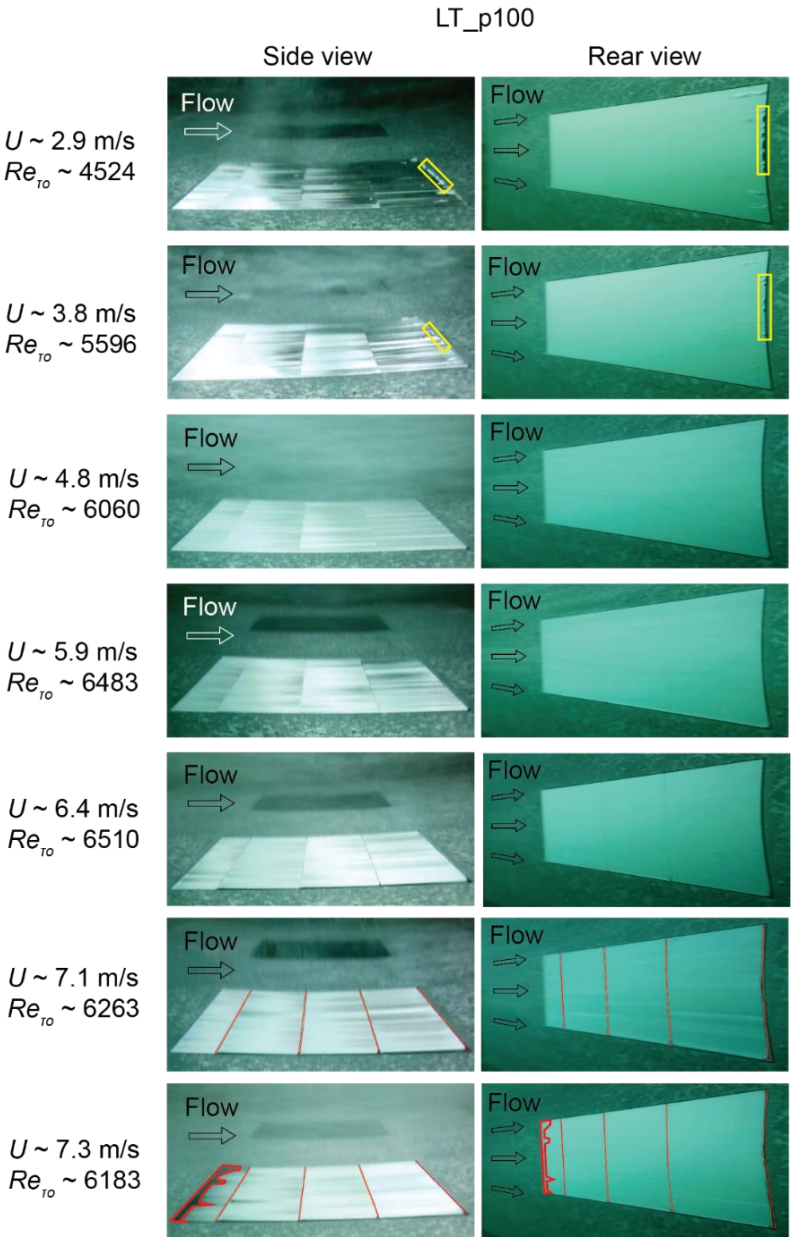

Figure 4-8. Image pairs of one of the two longitudinal trench samples with the pitch of 100 µm. The merged bubbles on the SHPo surface are labeled with yellow boxes. The depinned areas are labeled with red outlines. The depinning was not found on the other LT_p100 sample, which maintained a full plastron up to the top speed. The dark patches on surface in some of the side view pictures were found to vary in videos, which came from uneven background lighting caused by the water flow and the boat strake.

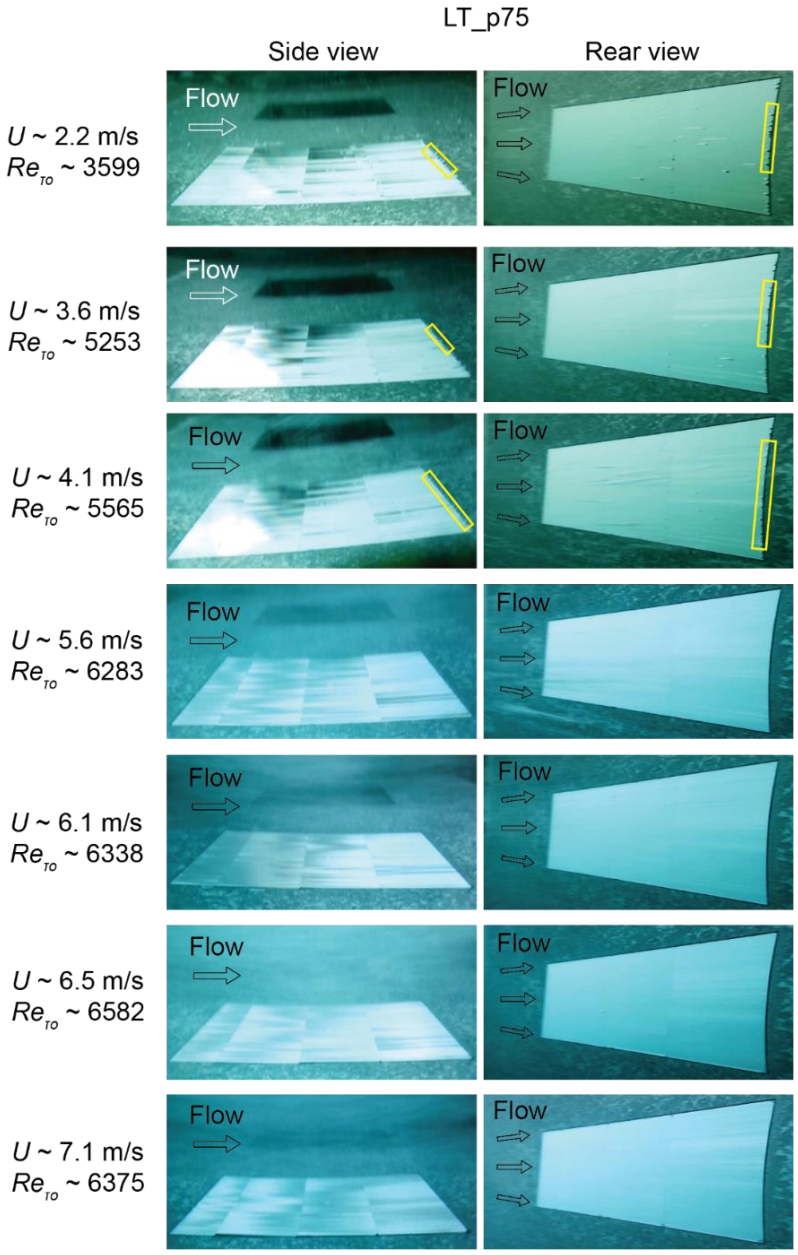

Figure 4-9. Image pairs of one of the two longitudinal trench samples with the pitch of 75 μm. The merged bubbles on the SHPo surface are labeled with yellow boxes. Full plastron was maintained up to the top speed. The dark patches on surface in some of the side view pictures were found to vary in videos, which came from uneven background lighting caused by the water flow and the boat strake.

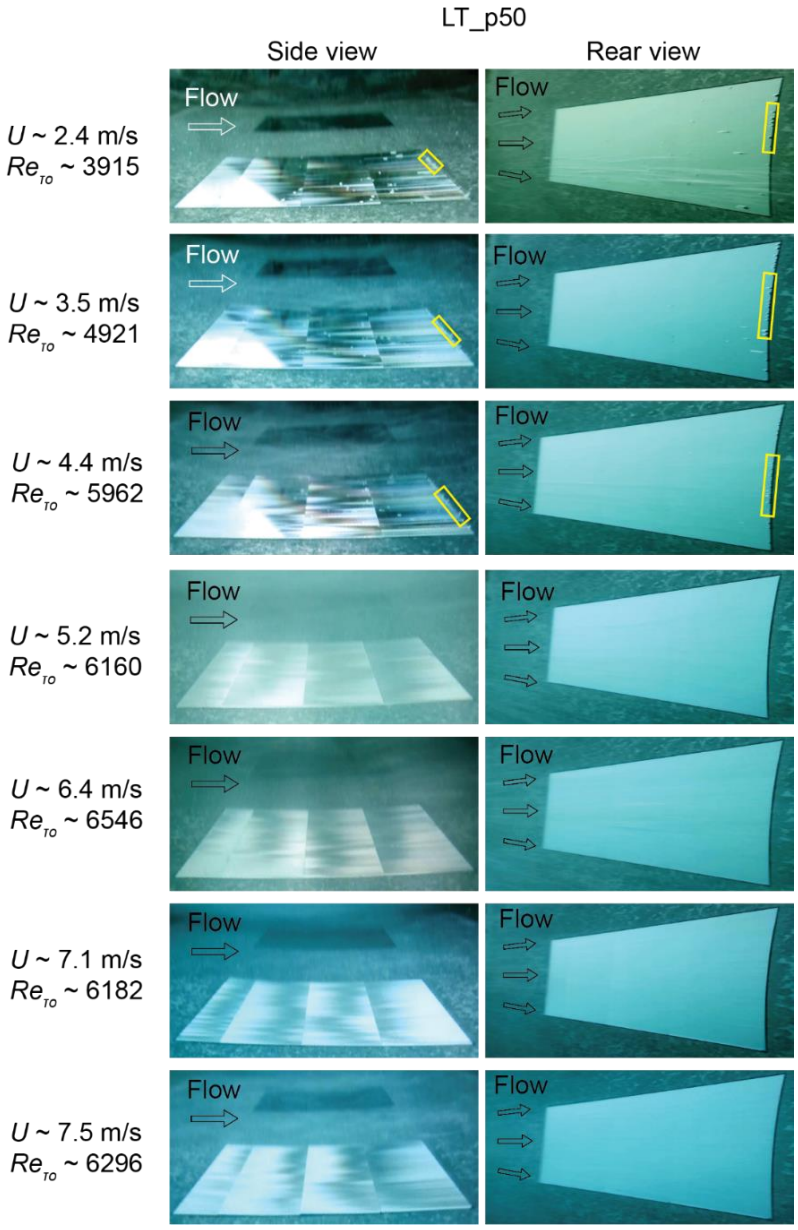

Figure 4-10. Images pairs of one of the two longitudinal trench samples with the pitch of 50 μm. The merged bubbles on the SHPo surface are labeled with yellow boxes. Full plastron was maintained up to the top speed. The dark patches on surface in some of the side view pictures were found to vary in videos, which came from uneven background lighting caused by the water flow and the boat strake.

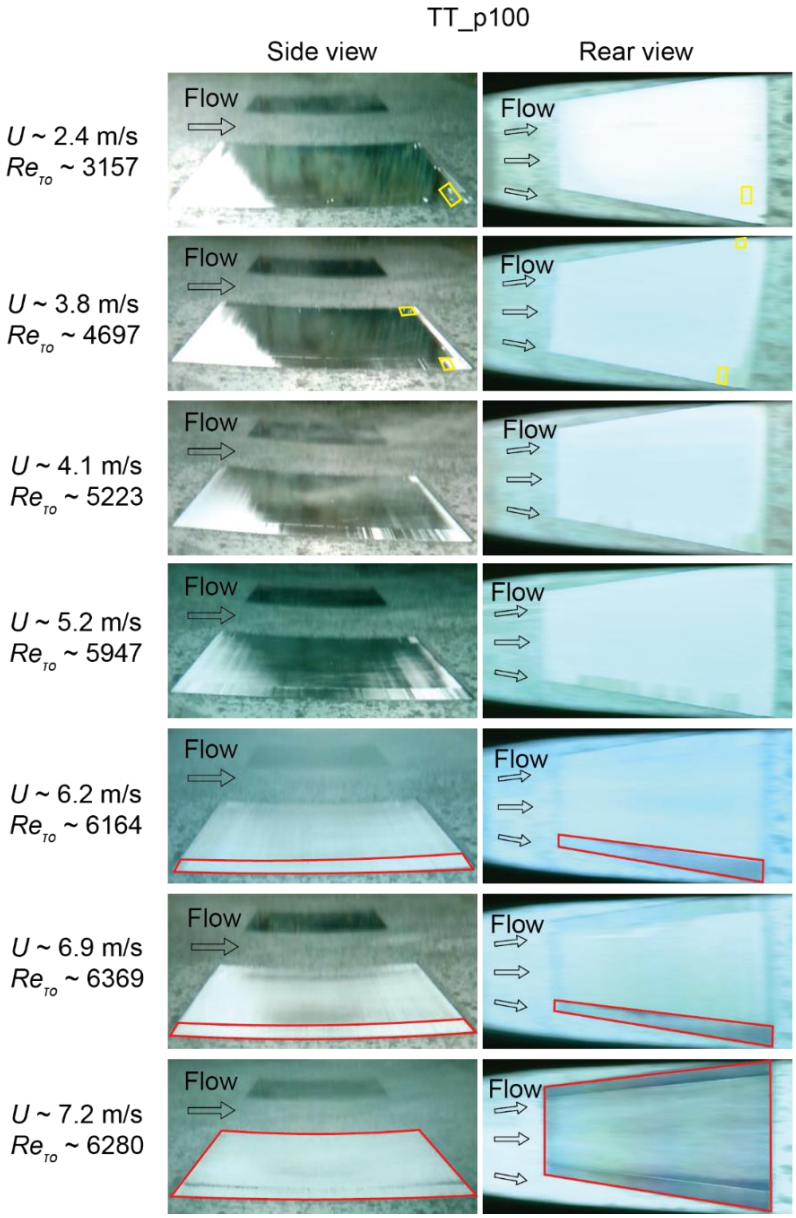

Figure 4-11. Image pairs of the transverse trench sample with the pitch of 100 µm. The merged bubbles on the SHPo surface are labeled with yellow boxes. The depinned areas are labeled with red outlines. The dark patches on surface in some of the side view pictures were found to vary in videos, which came from uneven background lighting caused by the water flow and the boat strake.

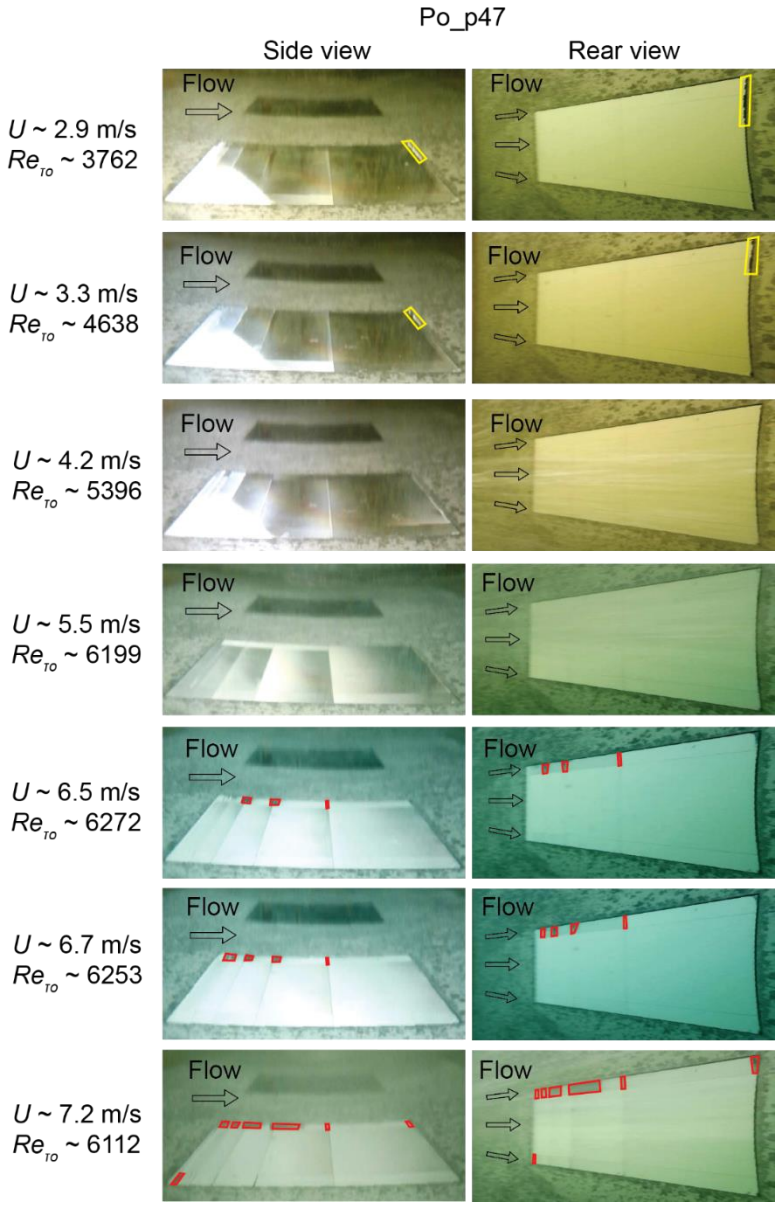

Figure 4-12. Image pairs of aligned post samples with the pitch of 47 μm. The merged bubbles on the SHPo surface are labeled with yellow boxes. The depinned areas are labeled with red outlines. The dark patches on surface in some of the side view pictures were found to vary in videos, which came from uneven background lighting caused by the water flow and the boat strake.

4.4.3 Drag Reduction of Longitudinal Trenches (LT)

Let us first report the drag ratio of the LT surfaces over a range of friction Reynolds number in Figure 4-13(a), following the common practice of presenting the drag ratio as a function of Reynolds number [12, 18, 23, 25, 46]. While the drag ratio data on LT obtained from the similar boat tests by Xu [12] were scattered and did not show more than a general trend, in this much-improved boat experiment, the drag ratio results of 6 LT samples revealed a clear trend of how the drag ratio decreases with the trench pitch (for ϕ_g = 0.9). Note that the drag reduction of ~30% on p = 100 μm is rough twice that of ~15% on p = 50 μm. Expecting the trenches with a larger pitch resulted in a smaller drag mostly due to the larger slip length, next we present the same results with respect to the normalized slip length of the surface, λ^{+o}, as shown in Figure 4-13(b), where $\lambda^{+o} = \lambda/\delta_{vo}$, δ_{vo} is the wall unit in the turbulent boundary layer on the smooth surface, defined as $\delta_{vo} = \nu/\sqrt{\tau_o/\rho}$, following the practice common for numerical studies [17, 18, 28, 32, 47, 48]. We calculated the slip length value by Equations (4-4) and (4-6) for this graph, which considers the viscous shear by the air in the trench. Note, for Figure 4-13(b), the nondimensional slip length was obtained using the theoretical slip length, which is derived by assuming laminar flows, while most of the numerical studies [18, 32, 47, 48] obtained the nondimensional slip length by solving the flow on a SHPo surface with certain surface geometry. All the data points obtained from LT samples with 3 different pitches (6 samples in total) collapsed to a single line, indicating that the normalized slip length is a good candidate parameter for determining the drag reduction of slip surfaces in turbulent flows. Likely, the current understanding that the drag decreases with the Reynolds number in turbulent flows is just a consequence of the wall unit decreasing with the Reynolds number. The linear regression fitting of all the data points in Figure 4-13(b) shows that the drag ratio is extrapolated to around 0.998 when λ^{+o} = 0, representing no drag reduction on a

smooth surface. Regarding the uncertainties of data, the horizontal error bars (standard deviations) were from the measurement uncertainties of boat speed, wetting length, and shear stress, and the vertical error bars were from the measurement uncertainties of the shear comparator, which is ±5% based on Figure 4-5(a).

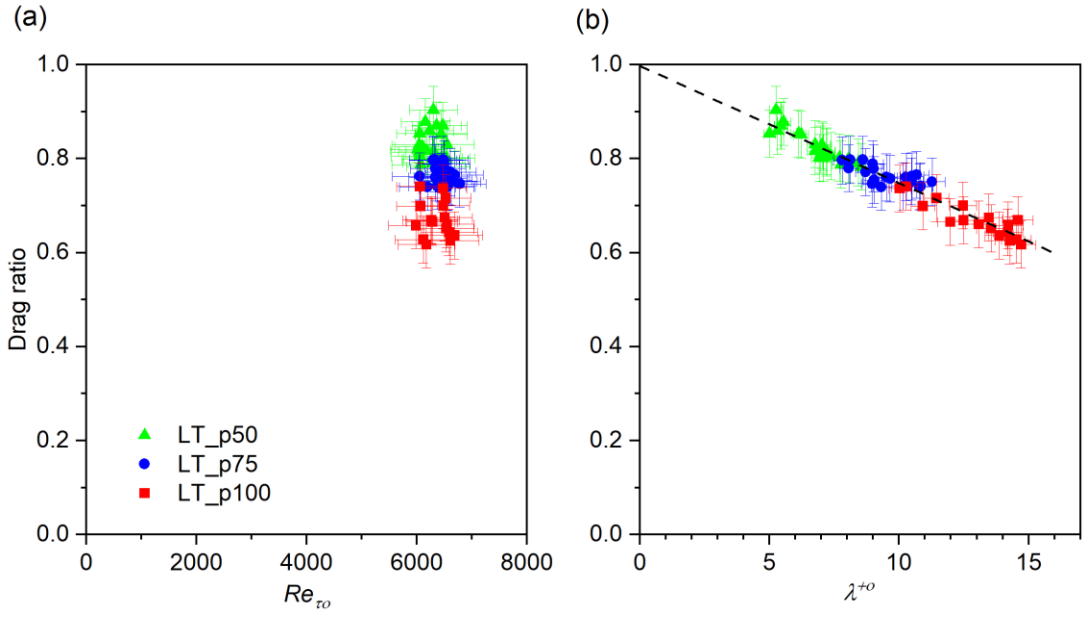

Figure 4-13. Drag ratio results on longitudinal trench surfaces. (a) Drag ratio versus friction Reynolds number. For the symbols, red squares, blue circles, and green triangles are from the trench widths of 100, 75, and 50 μm, respectively. (b) Drag ratio versus normalized slip length. The black dashed line is the linear regression of all the data points.

For comparison, we have plotted the drag ratio result of this study with all the LT data in the literature in Figure 4-14, including the numerical simulations [17, 18, 28, 32, 47, 48] and the previous experimental reports [12, 20, 23, 24], following the review by [8]. Although the normalized slip is usually presented in a log scale for the numerical studies to cover a wide range of values, we use a linear scale here because there is little possibility of encountering very large

values (e.g., $\lambda^{+o} > 25$) in reality. Since three numerical studies [18, 32, 47] reported the slip length normalized to the wall unit of SHPo surface, their data have been modified to represent the slip length normalized to the wall unit of smooth surface. Compared with the previous result from the similar boat setup (marked "Xu *et al.* (2020a), EXP, Boat"), which could not measure the wetting length accurately and lacked the current plastron observation technique to confirm full plastron, the current work showed a clear trend, where the drag ratio reduces with normalized slip length. The drag ratios obtained in this boat experiment are understandably larger than those by the Taylor-Couette flow experiment, which can provide infinitely long plastrons with no deterioration, and those by numerical studies, which assume flat interfaces as well as infinitely long trenches, but also larger than those by towing tank experiment (marked "Xu *et al.* (2021), EXP, TowT"). Although future studies will be needed to find the reasons for the difference, at this point, logical speculations include: (i) reduced slip length by a slightly depinned interface, which is likely less stable on the sample used for Xu [23], (ii) the shorter trenches (the current 1 and 2 cm vs. the previous 3.5 and 7 cm) combined with the surfactant effect resulting in more than proportional decrease in drag reduction, and (iii) the potential transverse flow caused by the V-shape of the hull hindering the drag reduction ability.

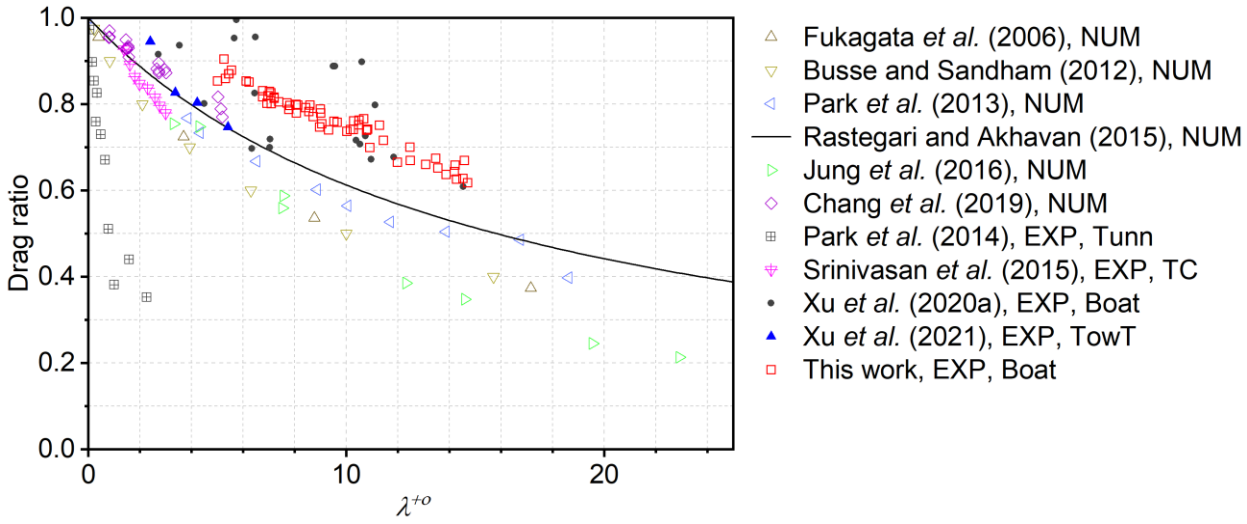

Figure 4-14. Comparison with literature. Drag ratio result of longitudinal trench SHPo surfaces (LT) as a function of dimensionless slip length from the current study (empty red circles) and other studies in the literature.Parts of the literature results were adapted from a recent review paper [8], while the data of Xu [12] and Xu [23] came from the original experimental records available to the authors. NUM means the numerical work. EXP means the experimental work. TC means the Taylor-Couette apparatus. Tunn means water tunnel. TowT means towing tank. Boat means motorboat.

4.4.4 Drag Reduction of Transverse Trenches (TT) and Aligned Posts (AP)

The drag reduction results of TT_p100 and AP_p47 surfaces are presented in Figure 4-15, along with those of the LT_p50 sample. While all the three samples were designed to have the same slip length in flow direction based on Equations (4-1), (4-2), and (4-3), their slip lengths in the transverse direction are different, as listed in Table 4-1. Compared with their longitudinal slip length, the transverse slip length is one-half for LT, twice for TT, and the same for AP. Unlike in laminar flows, where the transverse slip does not affect the longitudinal drag, in turbulent flows, the transverse slip is expected to increase the longitudinal drag [16, 28]. Accordingly, we expect

the drag ratio of AP to be larger than that of LP and the drag ratio of TT to be larger than that of AP. It should be noted that, in Figure 4-15, the slip lengths of LT and TT surfaces were calculated from Equations (4-4) to (4-7), which account for air viscosity, while the slip length of AP surface was calculated from Equation (4-3), which ignores the air viscosity. We expect the slip length of the AP surface would decrease only 5-10% when the air viscosity is accounted for, following the differences available for LT and TT surfaces. In Figure 4-15, the AP surface has a drag ratio slightly larger than that of LT, supporting the expectation that the spanwise slip on AP, which is twice that on LT, would increase the streamwise drag more than the spanwise slip on LT does. The TT surface has the largest drag ratio of the three, staying at 0.97–1.04 regardless of the dimensionless slip length, supporting the expectation that spanwise slip on TT, which is twice that on AP (and four times that on LT), would increase the streamwise drag more than the spanwise slip on AP does. Moreover, for the very small interfacial length in the flow direction on TT_p100 (i.e., 90 μm), there is a good chance that the surfactant in the water has eliminated any slip effect in the streamwise direction [49, 50].

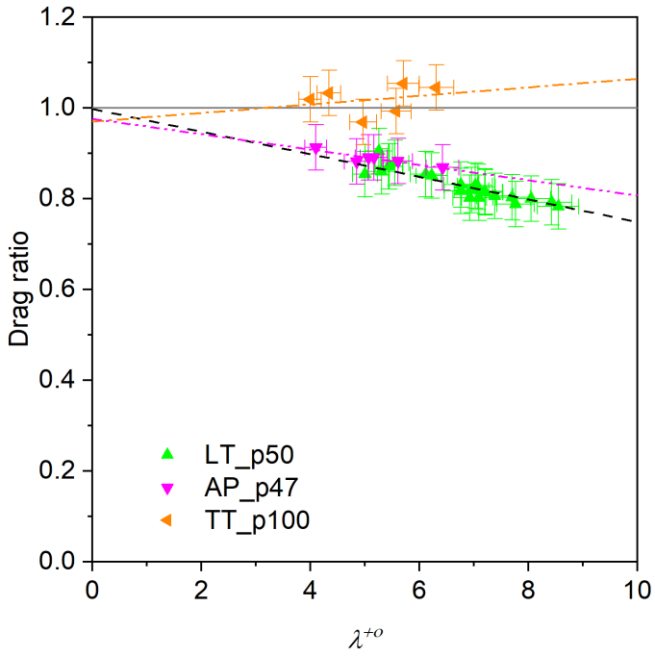

Figure 4-15. Drag ratio results on transverse trench and aligned post surfaces. The longitudinal trench surface with pitch of 50 μm is plotted for comparison. The three samples have identical longitudinal slip lengths but different transverse slip lengths. Green triangles, inverted magenta triangles, and rotated orange triangles are for LT, AP, and TT, respectively. The black dashed line is the linear fitting of the LT samples from Figure 4-13(b). The orange dash-dotted line is the linear fitting of the TT sample. The magenta dash-dot-dotted line is the linear fitting of the AP sample.

4.5 Conclusions

Using the unified theory that can predict the state of plastron on longitudinal trench SHPo surfaces in high-speed flows underwater, we have designed and fabricated high-performance SHPo surfaces that can maintain full plastron under the high shear rate of the current study (up to ~ 69000 s^{-1}). The motorboat used for Xu [12] has been revamped to expand the speed range and improve the boat balance. A recently developed observation system consisting of two underwater cameras was implemented to ensure the measured drag reduction data is not compromised by deteriorated

plastron. We have tested longitudinal trench SHPo surfaces with three different trench pitches and found the drag reduction is well described with the slip length nondimensionalized to the turbulent wall unit. By testing the SHPo surfaces with transverse trenches and aligned posts in comparison to the longitudinal trenches, the experimental results have confirmed that the spanwise slip deteriorates the drag reduction. In addition to expanding the speed range (from 10 knots to 14 knots) where a large drag reduction can be obtained with longitudinal trench SHPo surfaces in field conditions, this study has confirmed that the amount of drag reduction in turbulent flows can be predicted from the dimensionless slip length, shedding light to the design of drag-reducing SHPo surfaces in the future.

References

1. F. Brocher, "Reserches sur la respiration des insects aquatiques adultes–les haemonia.", *Ann Biol Lac*, 5, 5-26, 1912.

2. J.-L. Barrat and L. Bocquet, "Large slip effect at a nonwetting fluid-solid interface", *Physical review letters*, 82, 4671, 1999.

3. K. Watanabe, Y. Udagawa, and H. Udagawa, "Drag reduction of Newtonian fluid in a circular pipe with a highly water-repellent wall", *Journal of Fluid Mechanics*, 381, 225-238, 1999.

4. C.-H. Choi, K.J.A. Westin, and K.S. Breuer, "Apparent slip flows in hydrophilic and hydrophobic microchannels", *Physics of fluids*, 15, 2897-2902, 2003.

5. J. Ou, B. Perot, and J.P. Rothstein, "Laminar drag reduction in microchannels using ultrahydrophobic surfaces", *Physics of Fluids*, 16, 4635-4643, 2004.

6. C.-H. Choi, U. Ulmanella, J. Kim, C.-M. Ho, and C.-J. Kim, "Effective slip and friction reduction in nanograted superhydrophobic microchannels", *Physics of fluids*, 18, 087105, 2006.

7. C. Lee, C.-H. Choi, and C.-J. Kim, "Superhydrophobic drag reduction in laminar flows: a critical review", *Experiments in Fluids*, 57, 1-20, 2016.

8. H. Park, C.-H. Choi, and C.-J. Kim, "Superhydrophobic drag reduction in turbulent flows: a critical review", *Experiments in Fluids*, 62, 1-29, 2021.

9. M. Cheng, M. Song, H. Dong, and F. Shi, "Surface adhesive forces: a metric describing the drag‐reducing effects of superhydrophobic coatings", *Small*, 11, 1665-1671, 2015.

10. S. Zhang, X. Ouyang, J. Li, S. Gao, S. Han, L. Liu, and H. Wei, "Underwater drag-reducing effect of superhydrophobic submarine model", *Langmuir*, 31, 587-593, 2015.

11. H. Dong, M. Cheng, Y. Zhang, H. Wei, and F. Shi, "Extraordinary drag-reducing effect of a superhydrophobic coating on a macroscopic model ship at high speed", *Journal of Materials Chemistry A*, 1, 5886-5891, 2013.

12. M. Xu, A. Grabowski, N. Yu, G. Kerezyte, J.-W. Lee, B.R. Pfeifer, and C.-J. Kim, "Superhydrophobic drag reduction for turbulent flows in open water", *Physical Review Applied*, 13, 034056, 2020.

13. E. Lauga and H.A. Stone, "Effective slip in pressure-driven Stokes flow", *Journal of Fluid Mechanics*, 489, 55-77, 2003.

14. C. Ybert, C. Barentin, C. Cottin-Bizonne, P. Joseph, and L. Bocquet, "Achieving large slip with superhydrophobic surfaces: Scaling laws for generic geometries", *Physics of Fluids*, 19, 123601, 2007.

15. C. Lee and C.-H. Choi, "Structured surfaces for a giant liquid slip", *Physical Review Letters*, 101, 064501, 2008.

16. T. Min and J. Kim, "Effects of hydrophobic surface on skin-friction drag", *Physics of Fluids*, 16, L55-L58, 2004.

17. K. Fukagata, N. Kasagi, and P. Koumoutsakos, "A theoretical prediction of friction drag reduction in turbulent flow by superhydrophobic surfaces", *Physics of Fluids*, 18, 051703, 2006.

18. H. Park, H. Park, and J. Kim, "A numerical study of the effects of superhydrophobic surface on skin-friction drag in turbulent channel flow", *Physics of Fluids*, 25, 110815, 2013.

19. A. Rastegari and R. Akhavan, "The common mechanism of turbulent skin-friction drag reduction with superhydrophobic longitudinal microgrooves and riblets", *Journal of Fluid Mechanics*, 838, 68-104, 2018.

20. H. Park, G. Sun, and C.-J. Kim, "Superhydrophobic turbulent drag reduction as a function of surface grating parameters", *Journal of Fluid Mechanics*, 747, 722-734, 2014.

21. H. Li, S. Ji, X. Tan, Z. Li, Y. Xiang, P. Lv, and H. Duan, "Effect of Reynolds number on drag reduction in turbulent boundary layer flow over liquid–gas interface", *Physics of Fluids*, 32, 122111, 2020.

22. W. Abu Rowin and S. Ghaemi, "Effect of Reynolds number on turbulent channel flow over a superhydrophobic surface", *Physics of Fluids*, 32, 075105, 2020.

23. M. Xu, N. Yu, J. Kim, and C.-J. Kim, "Superhydrophobic drag reduction in high-speed towing tank", *Journal of Fluid Mechanics*, 908, A6, 2021.

24. S. Srinivasan, J.A. Kleingartner, J.B. Gilbert, R.E. Cohen, A.J. Milne, and G.H. McKinley, "Sustainable drag reduction in turbulent Taylor-Couette flows by depositing sprayable superhydrophobic surfaces", *Physical Review Letters*, 114, 014501, 2015.

25. E. Aljallis, M.A. Sarshar, R. Datla, V. Sikka, A. Jones, and C.-H. Choi, "Experimental study of skin friction drag reduction on superhydrophobic flat plates in high Reynolds number boundary layer flow", *Physics of Fluids*, 25, 025103, 2013.

26. J.W. Gose, K. Golovin, M. Boban, B. Tobelmann, E. Callison, J. Barros, M.P. Schultz, A. Tuteja, M. Perlin, and S.L. Ceccio, "Turbulent skin friction reduction through the application of superhydrophobic coatings to a towed submerged SUBOFF body", *Journal of Ship Research*, 65, 266-274, 2021.

27. Y. Liu, J.S. Wexler, C. Schönecker, and H.A. Stone, "Effect of viscosity ratio on the shear-driven failure of liquid-infused surfaces", *Physical Review Fluids*, 1, 074003, 2016.

28. A. Busse and N. Sandham, "Influence of an anisotropic slip-length boundary condition on turbulent channel flow", *Physics of Fluids*, 24, 055111, 2012.

29. J.R. Philip, "Flows satisfying mixed no-slip and no-shear conditions", *Zeitschrift für angewandte Mathematik und Physik ZAMP*, 23, 353-372, 1972.

30. A.M. Davis and E. Lauga, "Hydrodynamic friction of fakir-like superhydrophobic surfaces", *Journal of Fluid Mechanics*, 661, 402-411, 2010.

31. A.V. Belyaev and O.I. Vinogradova, "Effective slip in pressure-driven flow past super-hydrophobic stripes", *Journal of Fluid Mechanics*, 652, 489-499, 2010.

32. J. Chang, T. Jung, H. Choi, and J. Kim, "Predictions of the effective slip length and drag reduction with a lubricated micro-groove surface in a turbulent channel flow", *Journal of Fluid Mechanics*, 874, 797-820, 2019.

33. D. Crowdy, "Slip length for longitudinal shear flow over a dilute periodic mattress of protruding bubbles", *Physics of Fluids*, 22, 121703, 2010.

34. C.-O. Ng and C. Wang, "Effective slip for Stokes flow over a surface patterned with two- or three-dimensional protrusions", *Fluid Dynamics Research*, 43, 065504, 2011.

35. D.G. Crowdy, "Analytical formulae for longitudinal slip lengths over unidirectional superhydrophobic surfaces with curved menisci", *Journal of Fluid Mechanics*, 791, 2016.

36. C.-O. Ng and C. Wang, "Stokes shear flow over a grating: implications for superhydrophobic slip", *Physics of Fluids*, 21, 087105, 2009.

37. D.G. Crowdy, "Slip length formulas for longitudinal shear flow over a superhydrophobic grating with partially filled cavities", *Journal of Fluid Mechanics*, 925, 2021.

38. M. Xu, B. Arihara, H. Tong, N. Yu, Y. Ujiie, and C.-J. Kim, "A low-profile wall shear comparator to mount and test surface samples", *Experiments in Fluids*, 61, 1-13, 2020.

39. N. Yu, S. Kiani, M. Xu, and C.-J. Kim, "Brightness of Microtrench Superhydrophobic Surfaces and Visual Detection of Intermediate Wetting States", *Langmuir*, 37, 1206-1214, 2021.

40. W. Alert *Santa Monica Bay*. Available: https://windalert.com/spot/84161.

41. N. Yu, Z. Li, A.M. McClelland, F.J. del Campo Melchor, S.Y. Lee, J.H. Lee, and C.-J. Kim, *The state of plastron on micro-trench superhydrophobic surfaces in high-speed flows of open water* Mechanical and Aerospace Engineering, University of California, Los Angeles. 2022.

42. K.G. Nayar, D. Panchanathan, G. McKinley, and J. Lienhard, "Surface tension of seawater", *Journal of Physical and Chemical Reference Data*, 43, 043103, 2014.

43. A.J. Prosser and E.I. Franses, "Adsorption and surface tension of ionic surfactants at the air–water interface: review and evaluation of equilibrium models", *Colloids and Surfaces A: Physicochemical and Engineering Aspects*, 178, 1-40, 2001.

44. M.G. Morabito, "Empirical equations for planing hull bottom pressures", *Journal of Ship research*, 58, 185-200, 2014.

45. H. Schlichting and K. Gersten, *Boundary-layer theory*. 2003: Springer Science & Business Media.

46. R.A. Bidkar, L. Leblanc, A.J. Kulkarni, V. Bahadur, S.L. Ceccio, and M. Perlin, "Skin-friction drag reduction in the turbulent regime using random-textured hydrophobic surfaces", *Physics of Fluids*, 26, 085108, 2014.

47. A. Rastegari and R. Akhavan, "On the mechanism of turbulent drag reduction with super-hydrophobic surfaces", *Journal of Fluid Mechanics*, 773, 2015.

48. T. Jung, H. Choi, and J. Kim, "Effects of the air layer of an idealized superhydrophobic surface on the slip length and skin-friction drag", *Journal of Fluid Mechanics*, 790, 2016.

49. J.R. Landel, F.J. Peaudecerf, F. Temprano-Coleto, F. Gibou, R.E. Goldstein, and P. Luzzatto-Fegiz, "A theory for the slip and drag of superhydrophobic surfaces with surfactant", *Journal of Fluid Mechanics*, 883, 2020.

50. F. Temprano-Coleto, S.M. Smith, F.J. Peaudecerf, J.R. Landel, F. Gibou, and P. Luzzatto-Fegiz, "Slip on three-dimensional surfactant-contaminated superhydrophobic gratings", *arXiv preprint arXiv:2103.16945*, 2021.

Chapter 5 Summary and Outlook

5.1 Summary

In this dissertation, we focused on monitoring and achieving the pinned plastron state on the SHPo surface in the turbulent open water flow and tested the drag reduction of the SHPo surface with a full plastron.

First, due to the lack of a monitoring method, we studied the brightness of the intermediate wetting states on the micro-trench SHPo surface and developed a convenient method to detect the depinning, which accounts for most of the failures in previous drag reduction studies of SHPo surface in the turbulent flows in open water. A theory for anticipating the brightness of various wetting states based on the total internal reflection areas on the meniscus was developed and confirmed by the experiments with a customized observation stage equipped with underwater cameras and a confocal microscope. Various wetting states on the micro-trench SHPo surface were carefully generated, and the meniscus shape and position inside micro-trenches were precisely measured by the confocal microscope. Meanwhile, the images of SHPo surfaces were taken by the underwater cameras in a broad range of observing directions. A map of intrusion ratio was developed for designing the observation systems to detect the corresponding intermediate wetting state. For drag reduction experiments, the observing direction with small elevation and azimuth angles was confirmed that would allow for detection of even a slightly depinned state.

After we developed the observation method that allows confirmation of full plastron in field conditions, we further studied the key factors that cause the depinning on the SHPo surface. We summarized the major effects of hydrostatic pressure, air diffusion, and shear stress into a unified

theory for anticipating the length of pinned plastron on SHPo micro-trenches and analyzed the secondary effects from the water dynamic pressure and surfactant. For the experiments, we developed the SHPo surfaces with re-entrant edge and nano-grass to increase the plastron stability and promote the pinned state. We confirmed the theory utilizing the revamped motorboat and tested multiple SHPo surfaces in high-speed flows of open water. The length of pinned plastron was measured using the images from the underwater camera and found to fit the theoretical range reasonably well. The model provided us with the guidance to design geometrical parameters of the SHPo surface and allowed us to achieve a full plastron, i.e., pinned meniscus on the entire surface area, up to the maximum boat speeds.

Finally, with the full plastron on the SHPo surface in hands for the boat experiments, we quantified the drag reduction of the SHPo surface in the turbulent boundary layer flows under the boat, which had great discrepancies among the previous studies in the literature. The clear trend for the data from different SHPo samples helped us understand the effect of slip length on the drag reduction of the SHPo surface in the turbulent flows. Moreover, the reduced drag reduction on the transverse trenches and aligned posts compared to the longitudinal trenches verified the deterioration of the drag reduction due to the transverse slip. All in all, with the full plastron confirmed on the SHPo surface under the high-speed open water flow, we expect this study will open the door for the design of the SHPo surface for realistic drag reduction in the future.

5.2 Outlook

While the rear wetting on the SHPo micro-trench was regarded as a secondary effect causing the depinning of the plastron in our experiments, it could be problematic if the SHPo surface is applied in a surfactant-rich environment where the stagnant-cap effect of the surfactant becomes even more severe. The future study of the mechanism and properties of the stagnant cap on the water-air interface on the SHPo micro-trenches and its effects on the drag reduction ability is valuable for the future application of the SHPo surface.

While most of the numerical and experimental studies focused on the reduced skin friction on SHPo surface in laboratory flow facilities (e.g., water tunnel, towing tank), our experiments on boat studied the drag reduction of SHPo in a complex flow condition where the viscous friction can be affected by multiple elements, such as the non-zero pressure gradient caused by trim angle of the planing boat. Moreover, when planing, the hydrodynamic pressure of water under the boat varies substantially, challenging the maintenance of the full plastron on the SHPo surface. Therefore, the future application of SHPo surfaces under a real marine vessel would benefit from the study of the SHPo drag reduction at different positions of the vessel hull.

Lastly, while the size of SHPo surfaces in our experiments is limited to the 4 cm × 7 cm by the fabrication methods, it is time to investigate the fabrication of large-scale SHPo surfaces and test its feasibility for the drag reduction on a marine vessel.